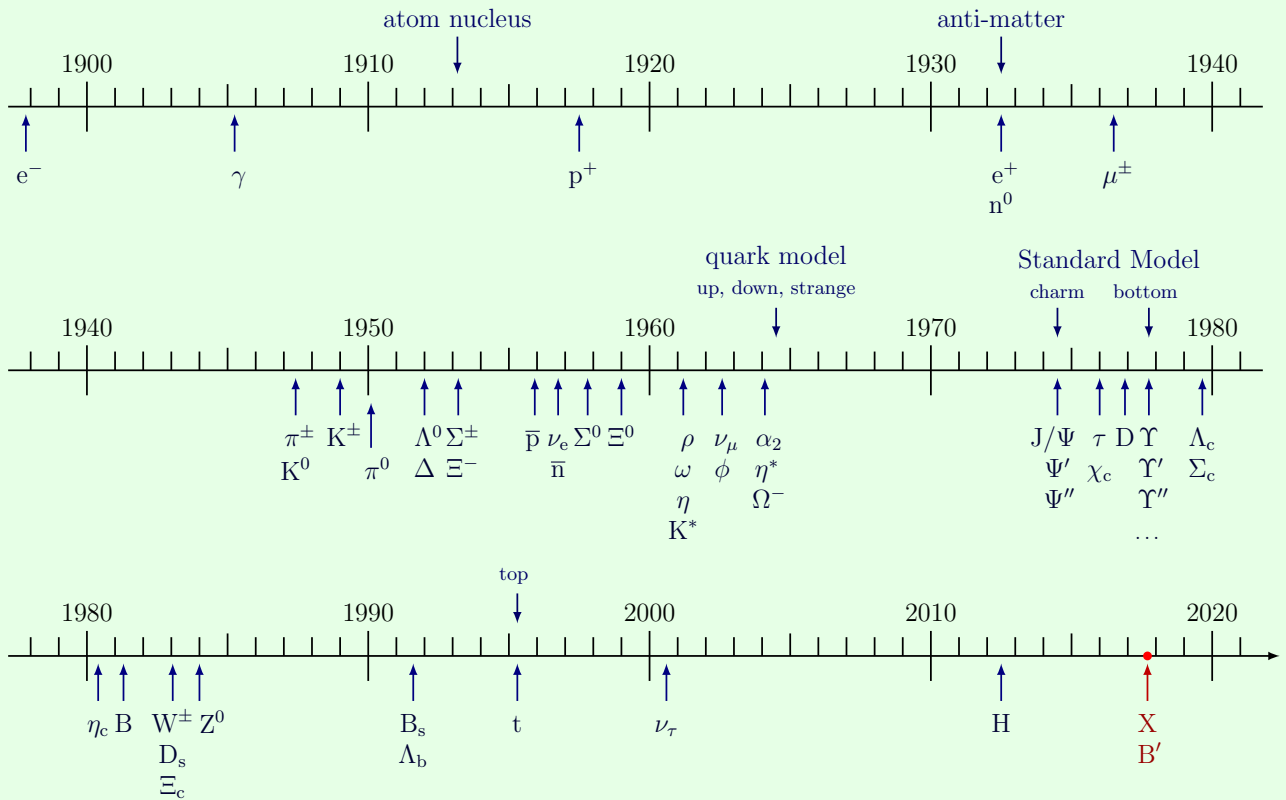

LECTURE NOTES OF SUBNUCLEAR PHYSICS

COLLECTION OF THE LECTURES NOTES OF PROFESSOR DONATELLA LUCCHESI.

EDITED BY

ARDINO ROCCO

ACADEMIC YEAR 2019-2020



Abstract

In this document I have tried to reorder the notes of the Subnuclear Physics course held by Professor Donatella Lucchesi at the Department of Physics of the University of Padua during the second semester of the 2019-20 academic year of the master's degree in Physics of Fundamental Interactions.

The notes are fully integrated with the material provided by the professor in the Moodle platform. In addition, I will integrate them, as best as possible, with the books recommended by the professor.

There may be formatting errors, wrong marks, missing exponents and even missing parts, since I'm still working on them. If you find errors or if you have any suggestions, let me know (you can send an e-mail at rocco.ardino@studenti.unipd.it, labeled with **SP::TYPO/SUGGESTION**) and I will correct/integrate them, so that this document can be a good study support. However, these notes are not to be intended as a substitute of the lectures held by the professor or of lecture notes made by other people.

Padova, Wednesday 10th June, 2020
Rocco Ardino

Contents

1	Introduction and Recap	3
1.1	Basic knowledge	3
1.2	Hydrogen atom and Positronium	5
1.3	Static Quark Model	9
1.3.1	Light quarks: charm and beauty	9
1.3.2	Light mesons	9
1.4	Leptons	11
2	Tools for calculations	13
2.1	Observables in experimental particle physics	13
2.2	Partial Width and Cross Section calculation	14
2.3	Phase Space integral calculation	15
3	Detectors for Particle Physics	19
3.1	Recap: interaction of particles with matter	19
3.1.1	Interactions involving the electrons and heavier particles	19
3.1.2	Interaction of photon with the matter	20
3.2	Gaseous, scintillator and solid state detectors	22
3.2.1	Gas detectors	22
3.2.2	Multiwire proportional chambers	24
3.2.3	Drift chambers	25
3.2.4	Semiconductor detectors	25
3.3	Track reconstruction	26
3.4	Calorimetry	27
3.4.1	Electromagnetic shower development	28
3.4.2	Hadronic shower development	28
3.4.3	Classification and response of calorimeters	30
3.4.4	Particle identification	32
4	Cross section of $e^+e^- \rightarrow \mu^+\mu^-$ and $e^+e^- \rightarrow hh$	33
4.1	Muon-Antimuon pair production: $e^+e^- \rightarrow \mu^+\mu^-$	33
4.1.1	Properties of massless spin- $\frac{1}{2}$ fermions	34
4.1.2	Matrix element and cross section evaluation	35
4.2	Hadron production: $e^+e^- \rightarrow$ hadrons	36
5	Deep Inelastic Electron Scattering	39
5.1	The SLAC-MIT experiment	39
5.2	The parton model	40
5.3	Crossing symmetry	41
5.4	Cross section for electron-quark scattering	43
5.5	Bjorken scaling	45
6	Strong interactions	49

6.1	The gluon	49
6.1.1	Measurement of parton distribution functions	49
6.1.2	Photon emission in $e^+e^- \rightarrow q\bar{q}$	51
6.1.3	Gluon effects on PDFs	52
6.2	QCD	52
6.2.1	Lagrangian dynamics and gauge invariance	52
6.2.2	Vacuum polarization	53
6.2.3	Running Coupling strong Constant	55
6.2.4	Structure of hadrons	57
6.2.5	Structure of jets	57
6.2.6	Production of top quark	57
7	Weak interactions	59
7.1	V-A Weak Theory	59
7.1.1	Experimental tests: muon decay	60
7.1.2	Experimental tests: pion decay	62
7.1.3	Experimental tests: neutrino scattering	63
7.2	Electroweak interaction	64
7.3	Experimental tests of electroweak interaction	67
7.3.1	Discovery of the neutral current	67
7.3.2	Discovery of W^\pm and Z^0 bosons	68
7.3.3	Measurements of W^\pm mass	72
7.3.4	Measurements of Z^0 mass	73
7.3.5	Measurement of A_{BF}	76
7.3.6	Determination of the Weinberg angle	76
7.3.7	Global fit of SM measurements	78
7.4	Cabibbo Theory and CKM matrix	79
7.4.1	The Cabibbo mixing angle	80
7.4.2	Quark and lepton mass terms in the Standard Model	81
7.4.3	Discrete space-time symmetries and the Standard Model	81
7.4.4	Experimental determination of V_{ud} , V_{cs} , V_{us} and V_{cd}	85
7.4.5	Experimental determination of V_{ub} , V_{cb} and V_{tb}	86
7.4.6	Experimental determination of V_{td} and V_{ts}	88
7.5	CP violation	89
7.5.1	CP violation in the K^0 - \bar{K}^0 system	89
7.5.2	CP violation in B -meson system	93
8	New Physics	99
8.1	Neutrino and Standard Model	99
8.1.1	Neutrino mass and β decay	99
8.1.2	Adding neutrino mass to the Standard Model	101
8.1.3	The V_{PNMS} effect	103
8.1.4	Neutrino mixing evidence	104
8.1.5	Summary of experimental results	108
8.2	Higgs boson and properties	108
8.2.1	Expected properties of the Higgs boson	108
8.2.2	Measurements of Higgs boson properties at the LHC	111
9	Exercises	117
	Bibliography	119

Course structure and program

Informations

Suggested books:

- *Concepts of Elementary Particle Physics*, Michael E. Peskin.
It has a very good experimental approach, with theoretical concepts explained as well.
- Any other book where the same topics are presented is fine. For example, the book of Alessandro Bettini.

Exam modalities: the exam is splitted into three parts. These are:

- **Written exercises.**

Given on moodle before the exam. We have to solve some of them and present the solutions at the exam.

- **Paper presentation.**

We have to choose a paper on a measurement or a discovery linked to the contents of the course. Then, we have to prepare a presentation of about 15 minutes (with slides).

- **Oral discussion.**

After the previous parts, some questions on the course topics can be asked.

The final evaluation will be a weighted mean of the three parts.

Remeber to subscribe to the Facebook group *Subnuclear Physics at DFA* for further informations and for infos on seminars of particle physics.

Course Program

- **Introduction and recap**

- **Tools for calculation.**

In order to understand all the following topics, we need some mathematical tools (that we already have but the way we are going to use them is different from the use we did in theoretical physics course). They are needed to evaluate the physical phenomena we are going to discuss.

- **Detectors for particle physics experiments.**

They are needed to perform measurements, so it is important to acquire a certain knowledge on them. For example, in order to choose why a detector is better than another one for a certain task and to set up a particle physics experiment. This part is not well described in the reference book, so we will use other books for this purpose.

Lecture 1.
Tuesday 10th
March, 2020.
Compiled:
Wednesday 10th
June, 2020.
Prof. Lucchesi

- **Cross section of $e^+e^- \rightarrow \mu^+\mu^-$ and $e^+e^- \rightarrow hh$.**

The former is a very simple process and it is important for the study of many other processes. The ladder will be important to understand the basis of QCD.

- **Strong interactions:**

- ▷ **Deep inelastic scattering**
- ▷ **Gluon**
- ▷ **QCD**
- ▷ **Partons and jets**

- **Electroweak interactions** (This part and the part on strong interactions sum up into the discussion on Standard Model):

- ▷ **V-A Weak theory.**

It is the theory at the base of electroweak interaction, which we will build up.

- ▷ **Gauge theory and symmetry breaking.**

This part will be discussed not so deeply since it was treated during the course of *Theoretical Physics of Fundamental Interactions*.

- ▷ **W and Z^0 bosons.**

The most important items and measurements will be presented.

- ▷ **Cabibbo theory and CKM.**

This part is needed in order to put the hadrons, in particular the quarks, into the electroweak theory. However, it will not be discussed deeply since it was presented during the bachelor course *Introduction to Nuclear and Subnuclear Physics*.

- ▷ **CP violation, the B meson system.**

It will be a more experimental discussion.

- **New Physics** (we will try to give an answer to how we can go beyond the description given by Standard Model, in fact there are phenomena that are still not explained by this theory):

- ▷ **Neutrino and Standard Model**

- ▷ **Higgs properties**

Chapter 1

Introduction and Recap

1.1 Basic knowledge

Relativistic wave equations

Relativistic quantum field theory is necessary to describe quantitatively elementary particle interactions. Its description is not part of this course, so we will use it in simple cases and only when necessary.

It is assumed the following knowledge:

- Klein-Gordon equation (for boson fields):

$$\left(\frac{\partial^2}{\partial t^2} - \nabla^2 + m^2 \right) \psi(t, \vec{x}) = 0 \quad (1.1)$$

- Dirac equation (Klein-Gordon can't give a description for fermion fields):

$$\left(i\gamma_\mu \frac{\partial}{\partial x_\mu} - m \right) \psi(t, \vec{x}) = 0 \quad (1.2)$$

with $\psi = (\psi_1, \psi_2, \psi_3, \psi_4)$

- Basic concepts of fields and particles
- Basic concepts of Feynman diagrams

Natural Units

During the course we will use the natural units, therefore:

$$\hbar = c = 1 \quad (1.3)$$

Considering that:

$$1 \text{ eV} = 1.6 \cdot 10^{-19} \text{ J}$$

$$c = 3 \cdot 10^8 \text{ m/s}$$

we have:

$$1 \frac{\text{eV}}{c^2} = 1.78 \cdot 10^{-36} \text{ Kg}$$

Since $E^2 = p^2c^2 + m^2c^4$, it is convenient to measure p in GeV/c and m in GeV/c^2 . For example the electron mass $m_e = 0.91 \cdot 10^{-27} \text{ g}$ corresponds to $m_e = 0.51 \text{ MeV}/c^2$. It is also useful to remember that $\hbar c = 197 \text{ MeVfm}$.

An interesting quantity to consider in natural units is the strength of the electric charge of the electron or proton. By taking into account the potential $V(r) = \frac{e^2}{4\pi\epsilon_0 r}$, the radius r in natural units has a dimension of Energy $^{-1}$. By this way it forces the following relation:

$$\alpha \equiv \frac{e^2}{4\pi\epsilon_0\hbar c} = \frac{1}{137.036} \quad (1.4)$$

namely, the **fine structure constant**.

Symmetries

They are the corner stones of particle physics. The most important ones for our studies are the **space-time symmetries**, which can be classified into:

- Continuous symmetries:

- ▷ Translation in time. The generator of the group of time translations is the operator H , namely the Hamiltonian, which is linked to the energy quantity.
- ▷ Translation in space. The generator of the group of space translations is the operator \vec{p} , namely the momentum.
- ▷ Rotations. In this case, the generator of the group of this kind of transformations is the angular momentum \vec{L} .

If a system is invariant under one of these transformations, the corresponding generator, so H , \vec{p} or \vec{L} , is conserved.

- Discrete symmetries:

- ▷ Parity P :

$$x^\mu = (x^0, \vec{x}) \xrightarrow{P} (x^0, -\vec{x}) \quad (1.5)$$

Fermions have half-integer spin and angular momentum conservation requires their production in pairs. We can define therefore just relative parity. By convention, the proton p has parity equal to +1. The parity of the other fermions is given in relation to the parity of the proton.

Parity of bosons can be defined without ambiguity since they are not necessarily produced in pairs.

Parity of a fermion and its antiparticle (i.e. an antifermion) are opposite, while parity of a boson and its anti-boson are equal.

Moreover, the parity of the positron is equal to -1 . Quarks have parity equal to +1, leptons have parity equal to +1. Their antiparticles have parity equal to -1 .

Lastly, parity of a photon is equal to -1 .

- ▷ Time Reversal T :

$$x^\mu = (x^0, \vec{x}) \xrightarrow{T} (-x^0, \vec{x}) \quad (1.6)$$

- ▷ Charge Conjugation C :

$$\text{Particle} \xleftrightarrow{C} \text{Antiparticle} \quad (1.7)$$

It is needed in order to restore a complete symmetry under the exchange of a particle with its antiparticle. A photon has -1 eigenvalue under C , which means: $C|\gamma\rangle = -|\gamma\rangle$.

Fermion-antifermion have opposite intrinsic parity and for non elementary particles the total angular momentum has to be considered, in fact the C parity goes like $(-1)^\ell$ or $(-1)^{\ell+1}$ (depending on the intrinsic parity).

Fundamental constituents of the matter

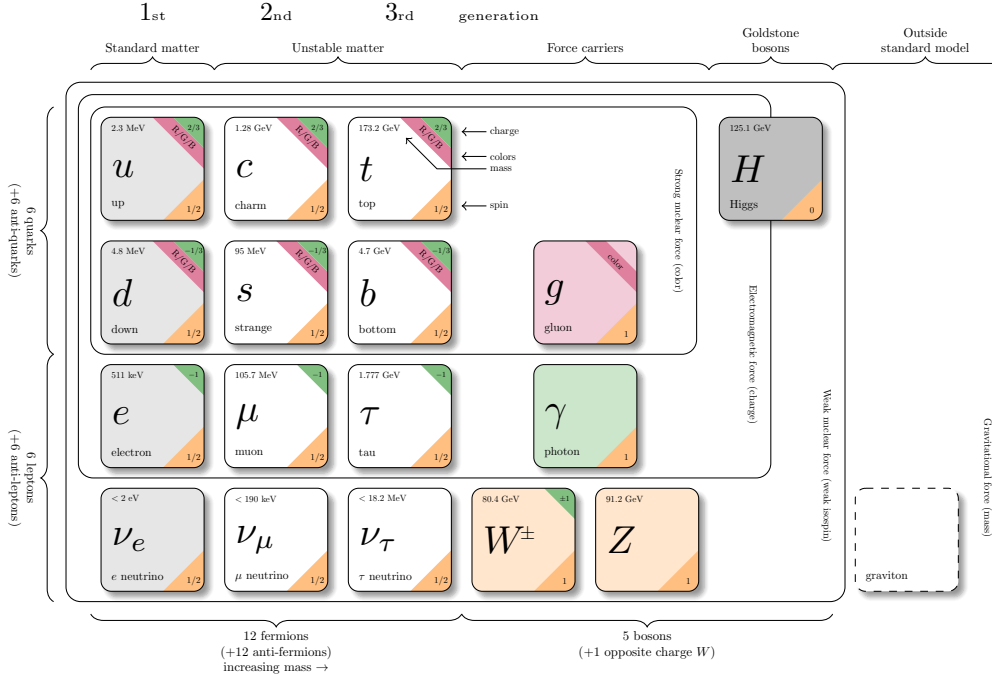


Figure 1.1: Standard Model particles.

1.2 Hydrogen atom and Positronium

We are going to study the already known system of the hydrogen atom, and compare it to the system of positronium. More in detail, our goal is to understand the e^+e^- bound state and the possible application of this model to the description of other systems. Therefore, we start from the hydrogen atom since it has some characteristics in common with the positronium.

In QM Physics, this bound state is really similar to the hydrogen atom. The assumptions for this one in the non relativistic limit are that the mass of the proton is much bigger than the mass of the electron ($m_p \gg m_e$) and the potential is given by:

$$V(r) = -\frac{e^2}{4\pi r} = -\frac{\alpha}{r} \quad (1.8)$$

From this potential, by solving the Schrödinger equation, we get the bound state energies:

$$E = -\frac{R_y}{n^2} \quad (1.9)$$

Lecture 2.
*Wednesday 11th
March, 2020.
Compiled:
Wednesday 10th
June, 2020.
Prof. Lucchesi*

R_y is known as **Rydberg energy**, whose expression reads:

$$R_y = \frac{1}{2} \frac{me^4}{(4\pi)^2} = 12.6 \text{ eV} \quad (1.10)$$

$$R_y = \frac{1}{2} \alpha^2 m_p \quad \text{In natural units} \quad (1.11)$$

The bound states of hydrogen are arranged in levels associated with integers $n = 1, 2, 3, \dots$. Each level contains the orbital angular momentum states:

$$\begin{aligned} \ell &= 0, 1, \dots, n-1 \\ m &= -\ell, \dots, \ell \end{aligned} \quad (1.12)$$

The orbital wavefunctions are the spherical harmonics $Y_{\ell m}(\theta, \varphi)$, which are even under spatial reflection for even ℓ and odd for odd ℓ . Then, under P , these states transform as:

$$P |n\ell m\rangle = (-1)^\ell |n\ell m\rangle \quad (1.13)$$

However, with these assumptions, we are not considering that the real hydrogen atom has more structure. In fact, we are neglecting that the electron is a particle with intrinsic spin and we have to take into account also this quantity. In a more technical way, we have to add the contribution of the spin-orbit interaction (fine splitting), which is proportional to the scalar product $\vec{\mathbf{L}} \cdot \vec{\mathbf{S}}$. Concerning the Hamiltonian of this contribution, it is given by:

$$\Delta H = \frac{g-1}{2} \frac{\alpha}{m^2 r^3} \vec{\mathbf{L}} \cdot \vec{\mathbf{S}} \quad (1.14)$$

The sign is such that the state with $\vec{\mathbf{L}}$ and $\vec{\mathbf{S}}$ opposite in sign has lower energy. Moreover, it may be useful to express the operator $\vec{\mathbf{L}} \cdot \vec{\mathbf{S}}$ in terms of J^2, L^2, S^2 :

$$\vec{\mathbf{J}} = \vec{\mathbf{L}} + \vec{\mathbf{S}} \implies \vec{\mathbf{L}} \cdot \vec{\mathbf{S}} = \frac{1}{2} \left((\vec{\mathbf{L}} + \vec{\mathbf{S}})^2 - L^2 - S^2 \right) = \frac{1}{2} (J^2 - L^2 - S^2) \quad (1.15)$$

By this way it is straightforward to diagonalize the operator $\vec{\mathbf{L}} \cdot \vec{\mathbf{S}}$. At the end we get the order of magnitude of the spin-orbit interaction:

$$\left\langle \frac{\alpha}{m^2 r^3} \right\rangle \sim \frac{\alpha}{m^2 a_0^3} \sim \alpha^4 m \sim \alpha^2 R_y \quad (1.16)$$

Thus, this effect is a factor of 10^{-4} smaller than the splitting of the principal levels of hydrogen.

Another contribution that we have to add is the spin-spin interaction (hyperfine splitting) between electron and proton, which leads to the addition of another term into the total Hamiltonian. The magnetic moments of the proton and the electron interact, with the ground state favoring the configuration in which the two spins are opposite. Therefore:

$$\Delta H = C \vec{\mathbf{S}}_p \cdot \vec{\mathbf{S}}_e \quad (1.17)$$

where the C constant depends on the electron wavefunction.

Hence, we have several levels for the spin states. For example, the 1S state of hydrogen is split into two levels, corresponding to the total spin:

$$\vec{\mathbf{J}} = \vec{\mathbf{S}}_p + \vec{\mathbf{S}}_e \quad (1.18)$$

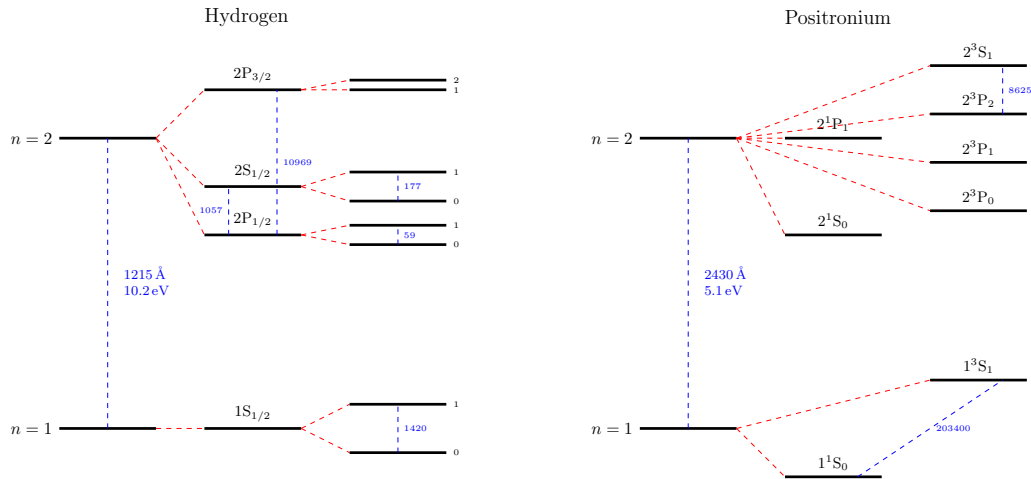


Figure 1.2: Comparison of the 1S, 2S, and 2P energy levels of hydrogen atom and positronium.

The possibilities we have are 2: $J = 0$ and $J = 1$, depending on how the two spin states of proton and electron combine. The projection on the z -axis gives 3 possibilities: $J_z = 1, 0, -1$ (corresponding to $|\uparrow\uparrow\rangle$, $\frac{1}{\sqrt{2}}(|\downarrow\uparrow\rangle + |\uparrow\downarrow\rangle)$, $|\downarrow\downarrow\rangle$).

Now the possibility that we have to evaluate is that e^+e^- forms bounded states. In fact, the same ideas can be applied to a particle-antiparticle system and the simplest case is the positronium.

It is relatively easy to make positronium. In colliders, when working with a beam of positrons which enter in the matter, they can pick up an electron and form a bounded state of positronium, so this is the starting point of the idea. All the considerations applied to the case of hydrogen atom can be applied to the positronium case as well. All the calculations are omitted. The first consideration is that here we can't apply the approximation $m_p \gg m_e$, in fact the two particles here have the same mass. The solution for this two-body problem is to use the reduced mass μ , namely:

$$\mu = \frac{m_1 m_2}{m_1 + m_2} = \frac{m_e}{2} \quad (1.19)$$

At the end of all the calculations we won't do, we get that the hyperfine splitting contribution is approximately of the same order of magnitude of the fine splitting and both are of the order $\alpha^4 m_e$.

Now we have to classify the eigenstates under parity and charge conjugation of the positronium. Let's consider first P . The intrinsic parity of the electron is $P_{e^-} = +1$, of the positron $P_{e^+} = -1$. So the parity of a single particle goes like $P = (-1)^\ell$ and the overall parity goes like $P = (-1)^{\ell+1}$.

For C , we must account three effects:

- C converts the electron to the positron and the positron to the electron. The electron and positron are fermions, and so, when we put the electron and positron back into their original order in the wavefunction, we get a factor -1 .
- Reversal of the coordinate in the orbital wavefunction gives a factor $(-1)^\ell$.
- Finally, the electron and positron spins are interchanged. The $S = 1$ state is

symmetric in spin, but the $S = 0$ state is antisymmetric.

$$S = 0 \longrightarrow \frac{1}{2}(|\uparrow\downarrow\rangle - |\downarrow\uparrow\rangle)$$

$$S = 1 \longrightarrow |\uparrow\uparrow\rangle \quad \frac{1}{2}(|\uparrow\downarrow\rangle + |\downarrow\uparrow\rangle) \quad |\downarrow\uparrow\rangle$$

and so gives another factor (-1) .

In all, the positronium states have C :

$$C = (-1)^{\ell+1} \cdot \begin{cases} 1 & S = 1 \\ -1 & S = 0 \end{cases} \quad (1.20)$$

and what we get is the J^{PC} scheme. The low-lying states of the positronium spectrum then have the J^{PC} values as in Figure 1.3.

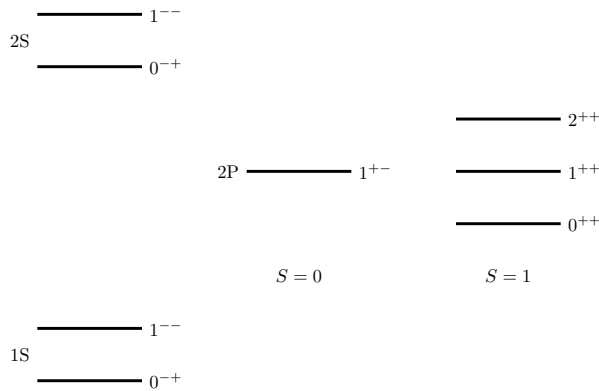


Figure 1.3: J^{PC} scheme. The 2P states 0^{++} , 1^{++} and 2^{++} arise from coupling the $L = 1$ orbital angular momentum to the $S = 1$ total spin angular momentum.

We know that electron and positron annihilate each other, so this state decays into something. The rules are E and \vec{P} conservation. It can't decay into a single photon since the momentum is not conserved. Recall that:

$$C|\gamma\rangle = -1 \implies C|n\gamma\rangle = (-1)^n \quad (1.21)$$

If we are looking for the two photon decay (so positive conjugation) of the positronium, the only possible state is the one with $S = 0$. If we are looking for a three photon decay (so negative conjugation), the only possible state is the one with $S = 1$. This kind of decay has been verified experimentally.

Positronium with state $S = 0$ is also known as **para-positronium**. If the state is $S = 1$, it is also known as **ortho-positronium**. Their medium lifes are:

$$\frac{1}{\tau_p} = \frac{1}{2}\alpha^5 m \quad \tau_p = 1.2 \cdot 10^{-10} \text{ s} \quad (1.22)$$

$$\frac{1}{\tau_o} = \frac{2}{9\pi}(\pi^2 - 9)\alpha^6 m \quad \tau_o = 1.4 \cdot 10^{-7} \text{ s} \quad (1.23)$$

So, when we emit positrons into a gas, $\frac{1}{4}$ of the states decays quickly in τ_p , while $\frac{3}{4}$ of the states decays slower in τ_o . It is a strange result, but experiment verifies it (Berko and Pendleton, 1980).

1.3 Static Quark Model

A beautifully simple way to create any particle, together with its antiparticle, is to annihilate electrons and positrons at high energy. The annihilation results in a short-lived excited state of electromagnetic fields. This state can then re-materialize into any particle-antiparticle pair that couples to electromagnetism and has a total mass less than the total energy of the annihilating e^+e^- system.

1.3.1 Light quarks: charm and beauty

By this way, the importance of the positronium state is clear. Moreover, it is linked to the discovery of quark charm and beauty.

Their discovery takes place in 1974 at SPEAR experiment, where by studying the process $e^+e^- \rightarrow hh, \mu^+\mu^-, e^+e^-$, an enormous, very narrow, resonance at about 3.1 GeV was discovered. This resonance would correspond to a new strongly interacting particle.

When they announced this discovery, they learned that the group of Samuel Ting, working at Brookhaven National Laboratory in Upton, New York, had also observed this new particle. Ting's group had studied the reaction $pp \rightarrow e^+e^- + X$, where the particles X are not observed.

This never observed particle is now called the J/ψ . A few weeks later, the SPEAR group discovered a second narrow resonance at 3686 MeV, the ψ' .

Another group of narrow resonances is found in e^+e^- annihilation at higher energy. The lightest state of this family, called Υ , has a mass of 9600 MeV. It was discovered by the group of Leon Lederman in the reaction $pp \rightarrow \mu^+\mu^- + X$ at the Fermilab proton accelerator.

Concerning the J/ψ , this particle is given by a quark doublet $c\bar{c}$ called **charmonium**. If this state exists, we will see phenomena like the ones observed with positronium. In the process $e^+e^- \rightarrow hh$, the highest rate reactions are those in which e^+e^- pair is annihilated by the electromagnetic current $\vec{j} = \bar{\psi}\gamma\psi$ through the matrix element:

$$\langle 0 | \vec{j}(x) | e^+e^- \rangle \quad (1.24)$$

The current has spin 1, $P = -1$, and $C = -1$. These must also be properties of the annihilating e^+e^- state, and of the new state that is produced. So, all of the ψ and Υ states must have $J^{PC} = 1^{--}$.

The current creates or annihilates a particle and antiparticle at a point in space. So, if these particles are particle-antiparticle bound states, the wavefunctions in these bound states must be nonzero at the origin. Most probably, they would be the 1S, 2S, etc. bound states of a potential problem. If this guess is correct, the states with higher L must also exist. They might be produced in radiative decays of the ψ and Υ states. Indeed, there is an experimental evidence, with a pattern of states as in Figure 1.4.

Remarkably, this reproduces exactly the pattern of the lowest-energy states of positronium and makes even more clear that the analogy to positronium is precise. In the case of the ψ family, the fermion is called the charm quark (c); this quark has a mass of about 1.8 GeV. In the case of the Υ family, the fermion is called the bottom quark (b); this quark has a mass of about 5 GeV.

1.3.2 Light mesons

Now we can go back to the π mesons and other relatively light hadrons. π s are the strongly interacting particles and there are three π mesons: π^0, π^+ and π^- .

Lecture 3.
 Tuesday 17th
 March, 2020.
 Compiled:
 Wednesday 10th
 June, 2020.
 Prof. Lucchesi

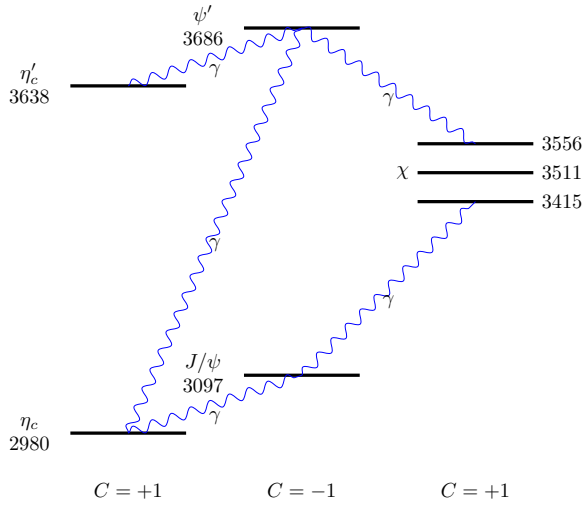


Figure 1.4: Pattern of states for the charmonium.

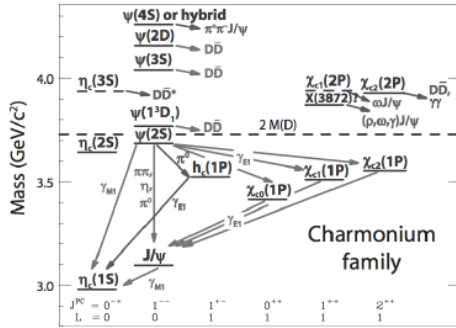


Figure 1.5: Observed states and transitions of the J/ψ system.

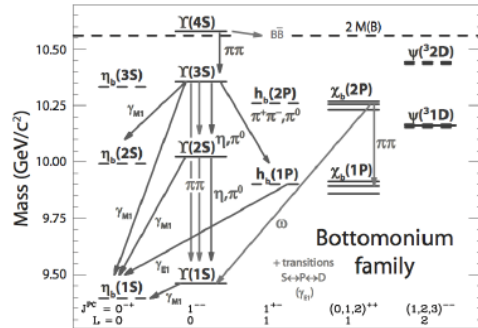


Figure 1.6: Observed states and transitions of the Υ system.

Their history is the beginning of modern particle physics and they were discovered in 1947, when Lattes, Occhialini and Powell demonstrated the existence of π^\pm through $\pi^\pm \rightarrow \mu^\pm + \nu$.

By detailed study of their interactions, it was determined that the π mesons also had $J^P = 0^-$. The π^0 decays to 2 photons, so it is $C = +1$. All of this is consistent with the interpretation of the pions as spin- $\frac{1}{2}$ fermion-antifermion bound states.

There are 9 relatively light 0^- hadrons, also known as **pseudoscalar mesons**, and 9 somewhat heavier 1^- hadrons, called the **vector mesons**, presented in Figure 1.7. The K and K^* states are not produced singly in strong interactions. They are only produced together with one another, or with special excited states of the proton. For example, we see the reactions:

$$\begin{aligned}\pi^- p &\rightarrow n K^+ K^- \\ \pi^- p &\rightarrow \Lambda^0 K^0\end{aligned}$$

where Λ^0 is a heavy excited state of the proton, but we don't see the reaction:

$$\pi^- p \rightarrow n K^0$$

For this reason, the K mesons and the Λ^0 baryon became known as the strange particles.

As a consequence of this discovery, a new quantum number, the **strangeness**, was introduced to describe the production and decay processes. It was found that the

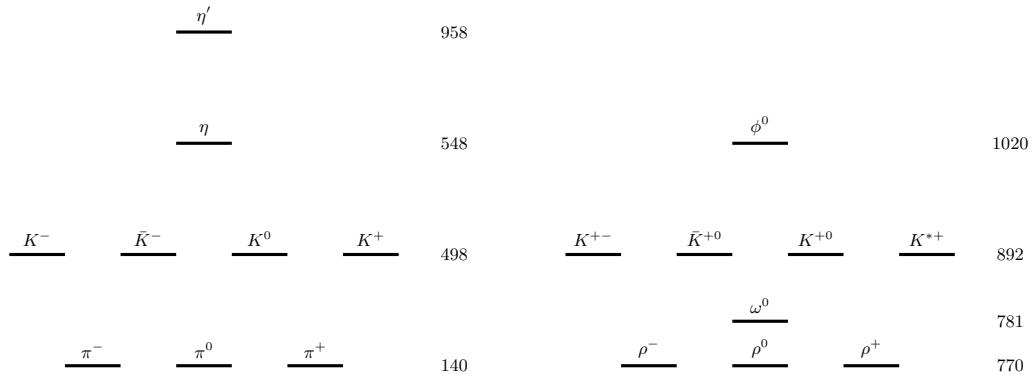


Figure 1.7: Light mesons summary. On the left there are the pseudoscalar mesons, on the right the vector mesons. The numbers given are the masses of the particles in MeV.

rules for K and K^* production can be expressed simply by saying that the strong interaction preserves the strangeness, with K^0 , K^+ , K^{*0} and K^{*+} having strangeness $S = -1$, their antiparticles having $S = +1$, and the Λ^0 having $S = +1$. Moreover, with the introduction of strangeness, a new kind of quark was introduced in the theories, namely the strange quark s . States with strangeness $+1$ will be assigned one s quark, and states with strangeness -1 will have one \bar{s} antiquark.

1.4 Leptons

The leptons are fundamental particles, divided in several classes. We have:

- **Electron e .**

It was discovered by J.J. Thomson in 1897 while studying the properties of cathode rays.

- **Muon μ .**

It was discovered by Carl D. Anderson and Seth Neddermeyer in 1936 as component of the cosmic rays. At the beginning it was thought to be the Yukawa particle, the mediator of the strong force. Then Conversi, Pancini and Piccioni gave a proof that it does not interact strongly.

- **Tauon τ .**

It was discovered by a group led by Martin Perl at Stanford Linear Accelerator Center. They used e^+e^- collisions with final states events $e\mu$.

- **Neutrino ν .**

Neutrino hypothesis was formulated by Pauli to explain the β -decay. It was discovered by Clyde Cowan and Fred Reines in the 1953. We don't know if mass is given to neutrinos through the same mechanism (Higgs mechanism) for the other particles or if there is something that does it that we still don't know.

Chapter 2

Tools for calculations

To compare the results of elementary particle experiments to proposed theories of the fundamental forces, we must think carefully about what quantities we can compute and measure. We cannot directly measure the force that one elementary particle exerts on another. Most of our information about the subnuclear forces is obtained from scattering experiments or from observations of particle decay.

In scattering experiments, the basic measureable quantity is called the **differential cross section**. In particle decay, the basic measureable quantity is called the **partial width**.

2.1 Observables in experimental particle physics

The basic observable quantity associated with a decaying particle is the **rate of decay**. In quantum mechanics, an unstable particle A decays with the same probability in each unit of time. The probability of survival to time t then obeys the differential equation:

$$\frac{dP(t)}{dt} = -\frac{P}{\tau_A} \xrightarrow{\text{solution}} P(t) = P_0 e^{-\frac{t}{\tau_A}} \quad (2.1)$$

The decay rate τ_A^{-1} is also called the **total width** Γ_A of the state A . Its dimension is 1/sec, equivalent to GeV up to factors of \hbar and c .

$$\tau_A = \frac{1}{\Gamma_A} \quad \Gamma_A = \text{Total width of the state } A \quad (2.2)$$

If there are multiple decay processes like $A \rightarrow f$, each process has a rate $\Gamma(A \rightarrow f)$, namely the **partial width**. Thus, the total decay rate is given by:

$$\Gamma_A = \sum_f \Gamma(A \rightarrow f) \quad (2.3)$$

Another quantity called **branching ratio** can be defined by the definition of the previous ones:

$$\frac{\Gamma(A \rightarrow f)}{\Gamma_A} = \text{Branching ratio} \quad (2.4)$$

We can now introduce the **cross section**. Let's imagine a fixed target experiment, where a beam of A particles of density n_A and velocity v_A , are shot at the fixed center B . What we can measure includes the rate R at which we see scatterings from the beam:

$$R = \frac{\text{Number of events}}{\text{Time}} = n_A v_A \sigma_i \quad (2.5)$$

with σ_i the cross section of the process, which has the dimension of an area and it is measured in barn (10^{-28} m^2). It is the effective area that the target B presents to the beam. Another important quantity is the **luminosity**, i.e.:

$$\mathcal{L} = \frac{R}{\sigma_i} \quad (2.6)$$

Returning to the cross section, an alternative definition can be given. Imagine two bunches of particles A and B aimed at one another, namely a collision between two beams. The key idea is that the second beam is the target, so we consider $N_B = n_B l_B A_B$ in order to calculate the rate:

$$R = n_A n_B l_B A_B |v_A - v_B| \sigma_i \quad (2.7)$$

As pointed before, every beam is composed of bunches with the following gaussian distribution:

$$\frac{dN}{ds} = \frac{N}{2\pi\sigma_x\sigma_y} e^{-\left(\frac{x^2}{2\sigma_x^2} + \frac{y^2}{2\sigma_y^2}\right)} \quad (2.8)$$

The number of interactions per bunch is $N_{\text{int}} = \sigma_{\text{int}} \frac{N_1 N_2}{4\pi\sigma_x\sigma_y}$ and the bunch frequency is f . Therefore, we can calculate the rate:

$$R_i = N_{\text{int}} f = \sigma_{\text{int}} \frac{N_1 N_2}{4\pi\sigma_x\sigma_y} \quad (2.9)$$

2.2 Partial Width and Cross Section calculation

The partial width and the cross section for a certain process can be calculated through **Fermi's Golden Rule** in a very practical way. By using the time evolution operator T , we can write:

$$\langle 1, 2, \dots, n | T | A(p_A) \rangle = \underbrace{\mathcal{M}(A \rightarrow 1, 2, \dots, n)}_{\text{Invariant matrix element}} (2\pi)^4 \delta^{(4)} \left(p_A - \sum_{i=1}^n p_i \right) \underbrace{\qquad}_{E, \vec{p} \text{ conservation}} \quad (2.10)$$

It is useful to work out the dimension of \mathcal{M} . The operator T is dimensionless, and the states have total dimension $\text{GeV}^{-(n+1)}$. The delta function has units GeV^{-4} . Then the invariant matrix element has the units:

$$\mathcal{M} \sim \text{GeV}^{3-n} \quad (2.11)$$

Now, to find the total rate, we must integrate over all possible values of the final momenta. This integral is called **phase space** and for n final particles, the expression for the phase space integral is:

$$\int d\Pi_n = \int \frac{d^3 p_1}{(2\pi)^3 2E_1} \cdots \frac{d^3 p_n}{(2\pi)^3 2E_n} (2\pi)^4 \delta^{(4)} \left(p_A - \sum_{i=1}^n p_i \right) \quad (2.12)$$

However, we also need to normalize. So the initial state $|A\rangle$ will yield:

$$|A\rangle \rightarrow \frac{1}{2E_A} \quad \text{Initial state} \quad (2.13)$$

Finally, the Fermi Golden Rule formula for a partial width to an n -particle final state f is:

$$\Gamma(A \rightarrow f) = \frac{1}{2M_A} \int d\Pi_n |\mathcal{M}(A \rightarrow f)|^2 \quad (2.14)$$

If the final state particles have spin, we need to sum over final spin states. The initial state A is in some state of definite spin. If we have not defined the spin of A carefully, an alternative is to average over all possible spin states of A . By rotational invariance, the decay rate of A can't depend on its spin orientation.

Concerning the cross section, a formula for this quantity is constructed in a similar way. We need the matrix element for a transition from the two initial particles A and B to the final particles through the interaction. So, it reads:

$$\sigma(A + B \rightarrow f) = \frac{1}{2E_A E_B |v_A - v_B|} \int d\Pi_n |\mathcal{M}(A + B \rightarrow f)|^2 \quad (2.15)$$

2.3 Phase Space integral calculation

Phase space plays a very important role in particle physics. The default assumption is that final state particles are distributed according to phase space. This assumption is correct unless the transition matrix element has nontrivial structure. We will proceed with a couple of examples/exercises in order to understand the way of working with this kind of computations.

Example 1: Phase space of 2 particles

Most of the reactions we will discuss will have two particles in the final state. So it's better to start with this example. We have to compute:

$$\int d\Pi_2 = \int \frac{d^3 p_1}{(2\pi)^3 2E_1} \frac{d^3 p_2}{(2\pi)^3 2E_2} (2\pi)^4 \delta^{(4)}(p - p_1 - p_2) \quad (2.16)$$

Let's work in the CM system, where $\vec{p}_1 + \vec{p}_2 = 0$ and so $\vec{p}_1 = -\vec{p}_2$. Hence:

$$P = (E_{CM}, \vec{0}) \quad (2.17a)$$

$$p_1 = (E_1, \vec{p}) \quad (2.17b)$$

$$p_2 = (E_2, -\vec{p}) \quad (2.17c)$$

We have to integrate over \vec{p}_2 and exploit the properties of δ function:

$$\begin{aligned} \int d\Pi_2 &= \int \frac{d^3 p}{(2\pi)^3} \frac{1}{2E_1 2E_2} (2\pi) \delta(E_{CM} - E_1 - E_2) \\ &= \int \frac{p^2 d\Omega}{16\pi^2 E_1 E_2} \frac{E_1 E_2}{p E_{CM}} \\ &= \frac{1}{8\pi} \left(\frac{2p}{E_{CM}} \right) \int \frac{d\Omega}{4\pi} \end{aligned} \quad (2.18)$$

Example 2: Phase space of 3 particles

It is also possible to reduce the expression for three-body space to a relatively simple formula. Let's work again in the center of mass frame where $\vec{p}_1 + \vec{p}_2 + \vec{p}_3 = 0$ and let the total energy-momentum in this frame be $Q^0 = E_{CM}$. The three momentum vectors lie in the same plane, called **event plane**. Then the phase space integral can be written as an integral over the orientation of this plane and over the variables:

$$x_1 = \frac{2E_1}{E_{CM}} \quad x_2 = \frac{2E_2}{E_{CM}} \quad x_3 = \frac{2E_3}{E_{CM}}$$

which obey the constraint:

$$x_1 + x_2 + x_3 = 2$$

It can be shown that, after integrating over the orientation of the event plane, the integral over three-body phase space can be written as:

$$\int d\Pi_3 = \frac{E_{\text{CM}}^2}{128\pi^3} \int dx_1 dx_2 \quad (2.19)$$

It can be shown, further, that this integral can alternatively be written in terms of the invariant masses of pairs of the three vectors ($m_{12}^2 = (p_1 + p_2)^2$ and $m_{23}^2 = (p_2 + p_3)^2$):

$$\int d\Pi_3 = \frac{1}{128\pi^3 E_{\text{CM}}^2} \int dm_{12}^2 dm_{23}^2 \quad (2.20)$$

This formula leads to an important construction in hadron physics called the **Dalitz plot**.

Example 3: $\pi^+ \pi^- \rightarrow \rho^0 \rightarrow \pi^+ \pi^-$

One important type of structure that one finds in scattering amplitudes is a **resonance**. In ordinary quantum mechanics, a resonance is described by the **Breit-Wigner formula**:

$$\mathcal{M} \sim \frac{1}{E - E_R + \frac{i}{2}\Gamma} \quad (2.21)$$

where E_R is the energy of the resonant state and Γ is its decay rate. The Fourier transform of Eq. 2.21 is:

$$\psi(t) = ie^{-iE_R t} e^{-\Gamma \frac{t}{2}} \quad (2.22)$$

Then the probability of maintaining the resonance decays exponentially

$$|\psi(t)|^2 = e^{-\Gamma t} \quad (2.23)$$

corresponding to the lifetime:

$$\tau_R = \frac{1}{\Gamma} \quad (2.24)$$

It is useful to consider a specific example of a resonance in an elementary particle reaction, so we will consider $\pi^+ \pi^- \rightarrow \rho^0 \rightarrow \pi^+ \pi^-$, where the meson ρ^0 is found as a resonance at the ρ^0 mass of 770 MeV. We can represent this process by a diagram of evolution in space-time, as in Figure 2.1.

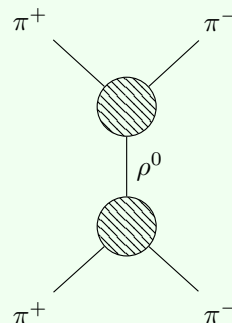


Figure 2.1: Diagram of $\pi^+\pi^- \rightarrow \rho^0 \rightarrow \pi^+\pi^-$.

Briefly, what we find is that the final distributions of the invariant masses are not in agreement with what we expect from the phase space distributions for two particles. In this case we can do the calculation in an easy way by studying:

1. $\pi^+\pi^- \rightarrow \rho^0$ and treat it as a stable particle
2. Using Feynman diagrams.

So, if we consider the cross section of $\pi^+\pi^- \rightarrow \rho^0$, we get:

$$\sigma(\pi^+\pi^- \rightarrow \rho^0) = \frac{1}{4E_A E_B |v_A - v_B|} \int \frac{d^3 p_C}{(2\pi)^3 2E_C} |\mathcal{M}|^2 (2\pi)^4 \delta^4(p_C - p_A - p_B) \quad (2.25)$$

where $A = \pi^+$, $B = \pi^-$ and $C = \rho^0$. The partial width reads:

$$\Gamma_\rho = \frac{1}{2m_\rho} \int d\Pi_2 |\mathcal{M}|^2 = \frac{g_\rho^2}{6\pi} \frac{p^3}{m_\rho^2} \quad (2.26)$$

By studying the cross section of the whole process $\pi^+\pi^- \rightarrow \rho^0 \rightarrow \pi^+\pi^-$, we get:

$$\sigma(\pi^+\pi^- \rightarrow \rho^0 \rightarrow \pi^+\pi^-) = \frac{1}{2m_\rho} \frac{1}{8\pi} \frac{2p}{m_\rho} \int \frac{d\Omega}{4\pi} \frac{1}{(E_{CM}^2 - m_p^2)^2 - m_p^2 \Gamma_\rho^2} |k|^2 \quad (2.27)$$

where k is a part related to the spin of ρ^0 .

We see a resonance and we are able to fit the data, so we can get the quantities we want to know as the parameters of the best fit.

Chapter 3

Detectors for Particle Physics

3.1 Recap: interaction of particles with matter

The way we identify particles is through their interaction with matter. So, we can detect:

- Charged particles based on ionization, breamsstrahlung, Cherenkov effect.
- γ -rays based on photoelectric/Compton effect and pair production.
- Neutrons based on strong interaction.
- Neutrinos based on weak interaction.

We will give only a phenomenological treatment since the goal is to be able to understand the implications for detector design.

3.1.1 Interactions involving the electrons and heavier particles

A relativistic charged particle with a mass much greater than the mass of the electron, when passing through the matter, is subject to a loss of energy due to the interaction with atomic electrons. These ones can be subtracted from the atom and then can be detected. From the total charge collected by the electrodes of a detector, it is possible to know the original interacting particle. The equation that describes this interaction and the loss of energy is the **Bethe-Bloch Equation** (in natural units):

$$-\left\langle \frac{dE}{dx} \right\rangle = K \rho \frac{Z}{A} \frac{z^2}{\beta^2} \left[\frac{1}{2} \log \frac{2m_e c^2 \beta^2 \gamma^2 T_{\max}}{I^2} - \beta^2 - \frac{\delta(\beta\gamma)}{2} - \frac{C}{z} \right] \quad (3.1)$$

where the meaning of the various symbols is given in Table 3.1. A plot showing the stopping power in function of the factor $\beta\gamma$ is given in Figure 3.1. In particular, from this plot we can see some interesting characteristics of the energy loss process. In the first part, the particle loses more energy when its velocity is slower, so the trend is $\sim \frac{1}{\beta^2}$. When the energy increases, a minimum is met, whose x -axis value is approximately the same for every material. The right part of the plot with respect to this minimum shows a gain in the energy loss which is due to relativistic effects.

The Bethe-Bloch formula is valid for particles much heavier than the electron. For this kind of particles, we have that relativistic effects even at low energies, since its mass is lower in comparison with the other particles. So, the electron loses energy through ionization (at lower energies) and **breamsstrahlung**, namely *braking radiation*, when deflected by another charged particle (at higher energies). The different materials that the electron can pass through, are characterized by their **radiation length** X_0 ,

Lecture 4.
Wednesday 18th
March, 2020.
Compiled:
Wednesday 10th
June, 2020.

*Interaction
through ionization*

*Breamsstrahlung
energy loss*

Symbol	Physical meaning
K	Constant [0.307075 MeVg ⁻¹ cm ²]
ρ	Density of the absorber
Z	Atomic number of absorber
A	Atomic mass of absorber
z	Atomic number of incident particle
β	Particle velocity in units of c
γ	Relativistic factor derived from β
T_{\max}	Maximum energy transfer in a single collision
I	Ionization potential of the absorber

Table 3.1: Bethe-Bloch formula: meaning of all the symbols figuring in its expression.

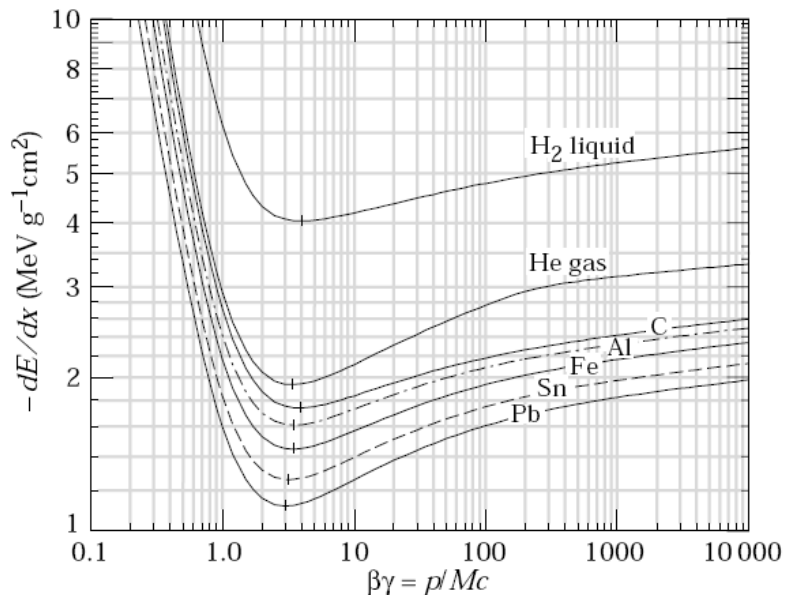


Figure 3.1: Few examples for different materials of Bethe-Bloch formula.

which is a quantity empirically defined as the distance covered by an electron beam before its energy decreases by a factor $\frac{1}{e}$ (63%). It is measured in g/cm² and an approximation of its expression is:

$$X_0 = \frac{A}{4\alpha N_A Z^2 r_e^2 \log \frac{183}{Z^{\frac{1}{3}}}} \quad (3.2)$$

Moreover, there exists a point in which the loss of energy due to ionization and the loss of energy due to bremsstrahlung are equal. This point is called **critical energy** E_c and a relatively good approximation of its value is:

$$E_c \approx \frac{600 \text{ MeV}}{Z} \quad (3.3)$$

Energy loss as a function of other parameters

Concerning the trend of these losses, we find that the ionization loss decreases logarithmically with E and increases linearly with Z , while bremsstrahlung loss increases approximately linearly with E and it is the dominant process at high energies. This is evident in the plots in Figures 3.2 and 3.3.

3.1.2 Interaction of photon with the matter

Photons can lose energy in several ways. The possibilities are:

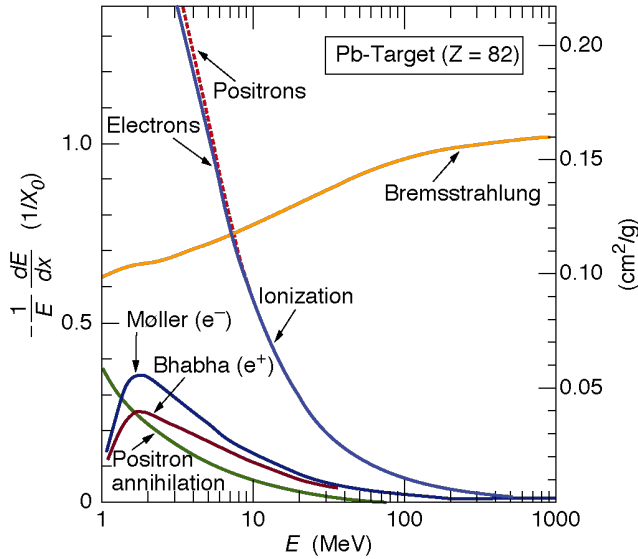


Figure 3.2: Total energy loss for electrons.

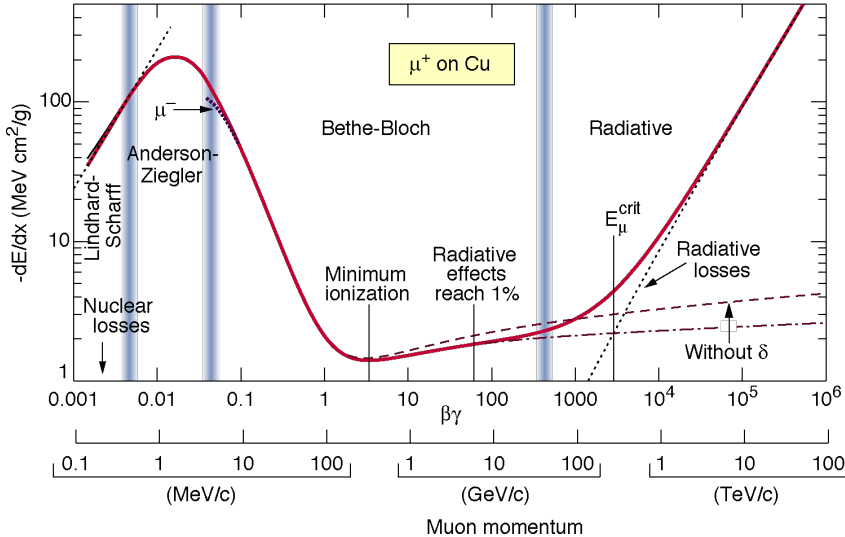


Figure 3.3: Energy loss summary.

- Photoelectric effect on atoms at low energy.
- Compton effect, which is important at medium range energies.
- Pair production, which is the dominant process at higher energies.

It goes without saying that we will focus on pair production, since we are discussing topics whose energies are relatively high. Concerning the cross section of this process, it is approximated by:

$$\sigma_{\text{pair}} = \frac{7}{9} \frac{N_A}{A} \frac{1}{X_0} \quad (3.4)$$

We can characterize a certain material by defining the **attenuation length** λ , namely the length for which the beam of photons inside the material is attenuated by a factor $\frac{1}{e}$, and it is linked to the radiation length by $\lambda = \frac{9}{7} X_0$.

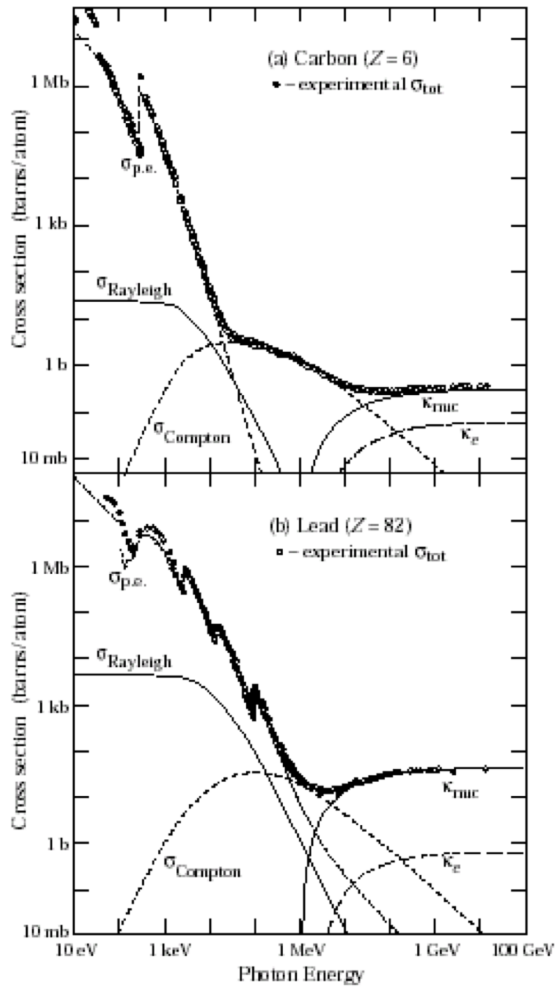


Figure 3.4: Interaction of photons with matter.

3.2 Gaseous, scintillator and solid state detectors

Particles can be identified as point-like objects with a certain mass and some other properties that characterize them. The only way to detect them is to make them interact inside a medium. With this technique we can measure their charge, medium lifetime, velocity, momentum and energy and from these we can retrieve their mass and a lot of other interesting properties. So, let's start a discussion on the many types of detectors that can be employed for a particle experiment.

3.2.1 Gas detectors

These detectors are based on the interaction of the particles with a gaseous medium. The interaction causes the ionization of the atoms in the medium, the charge is collected and from its total amount we can reconstruct the properties of the interacting particles.

In particular, we focus now on the ionization process. When the particle enters in the medium, a first ionization takes place and it is called **primary ionization**. For example, it can be schematized as follows:



The charges produced in the primary ionization interact as well with the medium

and they create a **secondary ionization**, as follows:



Experimentally speaking, it is important to evaluate the number of particles produced in the interaction and the relevant parameters to estimate this quantity are the ionization energy E_i , the average energy/ion pair W_i and the average number of ion pairs (per cm) n_T . By putting all together, we get:

$$\langle n_T \rangle = \frac{L \langle \frac{dE}{dx} \rangle}{W_i} \quad (3.7)$$

with L the thickness of the material. Typical values for E_i and n_T are:

$$E_i \sim 30 \text{ eV}$$

$$n_T \sim 100 \frac{\text{pairs}}{3 \text{ KeV}}$$

Another important effect to discuss in gas detectors is the **diffusion** in presence of electric and/or magnetic fields. These fields affect the trajectory of the particles transversally and longitudinally. In particular, by measuring the bending of the particle in presence of a magnetic field with a component orthogonal to the velocity vector, we are able to infer the momentum of the particle itself. The electric field influences only the longitudinal diffusion and not the transverse diffusion.

Lastly, another phenomenon that can happen in gas detectors is the **multiplication**. The electrons can undergo to a multiplication process called **Townsend avalanche**. Given the number of electrons at the position x , $n(x) = n_0 e^{\alpha x}$, we have the gain:

$$G = \frac{n(x)}{n_0} = e^{\alpha x} \quad (3.8)$$

where the parameter α can depend on x .

Depending on the gain factor G of the multiplication, four regions of work of the detector can be exploited:

- **Ionization mode**

The intensity of the electrical field E is low and the electric current at the electrodes of the detector is proportional to the charge produced in primary ionization.

- **Proportional mode**

It's the region of use for most of detectors and in this case E is sufficiently intense to generate a secondary ionization, so that the initial charge can be multiplied by a certain factor. It's also possible to measure the loss of energy of the original particle, proportional to the collected charge.

- **Limited proportional mode**

The amplification of ionization charge is now a process that can't be controlled since the electric field is too strong.

- **Geiger mode**

The electric field is so intense to generate an avalanche of electrons without control, that reaches the electrodes. It is not possible to measure the energy loss in this case, but we can only detect a logic signal that tells us if a particle has crossed the detector or not.

- Ionization mode:**
full charge collection
no multiplication; gain ≈ 1
- Proportional mode:**
multiplication of ionization
signal proportional to ionization
measurement of dE/dx
secondary avalanches need quenching;
gain $\approx 10^4 - 10^5$
- Limited proportional mode:**
[saturated, streamer]
strong photoemission
requires strong quenchers or pulsed HV;
gain $\approx 10^{10}$
- Geiger mode:**
massive photoemission;
full length of the anode wire affected;
discharge stopped by HV cut

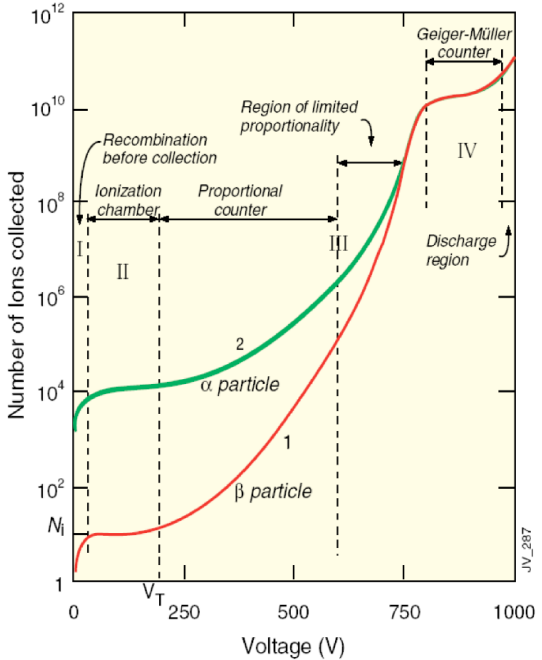


Figure 3.5: Regions of work of ionization detector with a plot giving numeric and practical examples.

3.2.2 Multiwire proportional chambers

They are proportional chambers with multiple wires added to reconstruct the trajectory of the particle. The cathode is the external shell, while the anodes are the internal wires, which generate an electrical field in first order approximation inversely proportional to the distance from the wire.

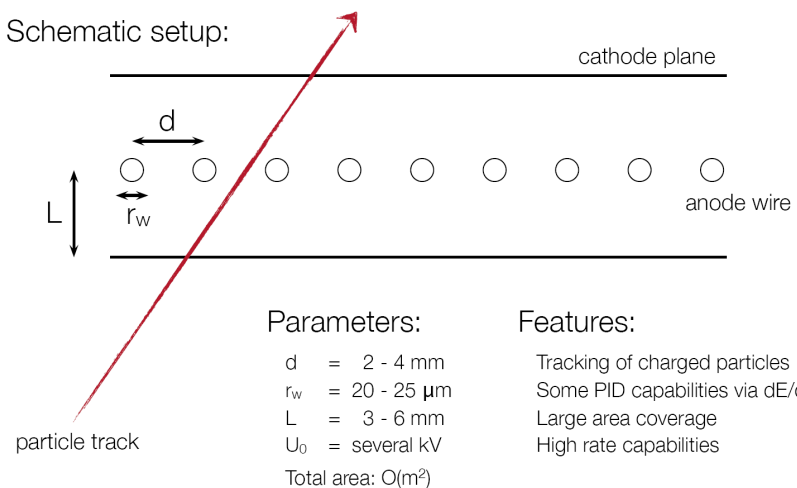


Figure 3.6: Description of multiwire proportional chamber structure and principle of work.

The principle of work is quite simple. The passage of a certain particle produces ionization charges, in particular electrons, which are collected by the nearest wire. Knowing which are all the anodes that collected ionization charge, we can understand the path followed by the crossing particle.

3.2.3 Drift chambers

Drift chambers are very similar to multiwire proportional chambers, however in this case we can have two dimensional informations through time measurements, namely **drift time** measurements.

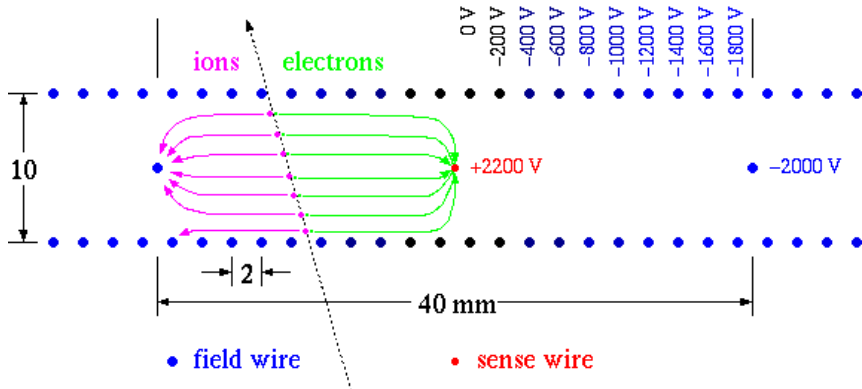


Figure 3.7: Scheme of a drift chamber.

They exploit an external detector such as a scintillator counter, near the chamber, to determine the time t_0 in which the particle arrives. The scintillator detects it and sends a signal to start a sort of chronometer. Then the particle cross the chamber and the electrons from the ionization drift to the nearest anode, captured by the electrical field. At the arrival of the electrons at the anode, a singals is sent to stop the time measurement. Now we have all the informations to extrapolate the drift time t_D , from which we can compute the spatial informations:

$$x = \int_0^{t_D} v_D dt \quad (3.9)$$

What is important to remember is that the detector is built with a studied geometry in order to get a known drift velocity.

3.2.4 Semiconductor detectors

Semiconductor detectors have the following characteristics:

- High density (respect to gas detectors), so large energy loss in a shorter distance.
- A small diffusion effect, so their position resolution can be less than $10 \mu\text{m}$.
- Low ionization energy, so it is easier to produce charged particles when they are crossed.

The materials employed for their construction can vary depending on the purpose of the detector itself. The possibilities are:

- Germanium, which needs to be operated at a very low temperature (77 K) due to small band gap in its microscopic structure.
- Silicon, which can operate at room temperature.
- Diamond, resistent to very hard radiations, with low noise signal. Its employment is still limited by a high cost of natural diamonds, however there exist some techniques through which the artificial production of diamond is a reality. So, diamond detectors are in development up to now.

Silicon detectors are the most common and they are based on a p-n junction with reverse bias applied to enlarge the depletion region. The potential barrier becomes higher so that the diffusion current across the junction is suppressed and the current across the junction is very small (“leakage current”).

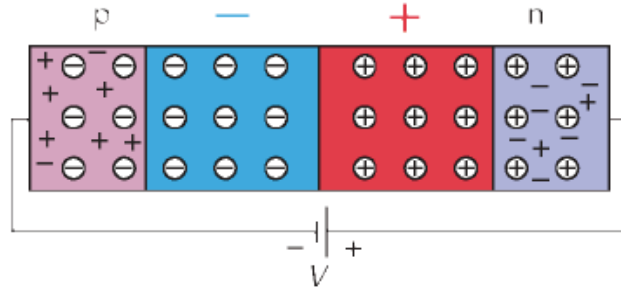


Figure 3.8: A p-n junction with reverse bias applied.

Such a detector can be built in strips. By segmenting the implant we can reconstruct the position of the traversing particle in one dimension. We have a higher field close to the collecting electrodes where most of the signal is induced. Strips can be read with dedicated electronics to minimize the noise.

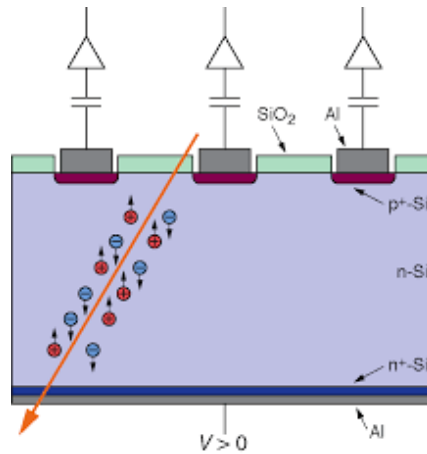


Figure 3.9: Silicon microstrip detector section with representation of ionization charges, generated by a traversing particle.

To have 2-dimensional measurements, double sided silicon detector are used. Moreover, a type of silicon detector still in development is the pixel detector (for 3-dimensional measurements).

Noise contributions can be leakage current and electronics readout. Instead, position resolution is the spread of the reconstructed position minus the true position. For example:

$$\sigma = \frac{\text{pitch length}}{\sqrt{12}} \quad \text{One strip cluster} \quad (3.10)$$

$$\sigma = \frac{\text{pitch length}}{1.5 \frac{S}{N}} \quad \text{Two strip cluster} \quad (3.11)$$

3.3 Track reconstruction

Track reconstruction is used to determine momentum of charged particles by measuring the bending of a particle trajectory in a magnetic field. The starting point is the

expression of the Lorentz force to which a particle is subjected when moving inside a magnetic field:

$$\vec{F} = q\vec{v} \times \vec{B} \quad (3.12)$$

from which we get:

$$m \frac{v^2}{r} = qvB \implies p = rqB \quad (3.13)$$

In fixed target experiments, Eq. 3.13 can be rewritten to:

$$p = qB \frac{L}{\theta} \quad (3.14)$$

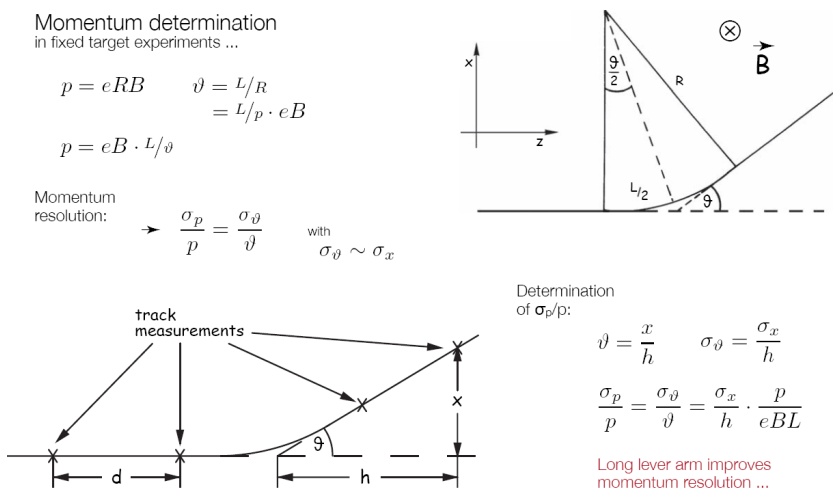


Figure 3.10: Tracking reconstruction example.

3.4 Calorimetry

Conceptually, a calorimeter is a block of matter, which intercepts the primary particle and is of sufficient thickness to cause it to interact and deposit all its energy inside the detector volume in a subsequent cascade or "shower" of increasingly lower-energy particles. Eventually most of the incident energy is dissipated and appears in the form of heat. Some (usually a very small) fraction of the deposited energy goes into the production of a more practical signal (e.g. scintillation light, Cerenkov light, or ionization charge), which is proportional to the initial energy.

In principle, the uncertainty in the energy measurement is governed by statistical fluctuations in the shower development, and the fractional resolution $\frac{\sigma}{E}$ improves with increasing energy E as $E^{-\frac{1}{2}}$.

At the outset it was noted that calorimetric detectors offer many other attractive capabilities, aside from the energy response, all of which have since been exploited in varying degrees:

- They are sensitive to charged and neutral particles
- The size of the detector scales logarithmically with the particle energy E , whereas for magnetic spectrometers the size scale with momentum p as $p^{\frac{1}{2}}$, for a given relative momentum resolution $\frac{\Delta p}{p}$.

Lecture 5.
Tuesday 24th
March, 2020.
Compiled:
Wednesday 10th
June, 2020.

Main features of calorimeters

- Through the use of segmented detectors the information of the shower development allows precise measurements of the position and angle of the incident particle.
- The shower development is a statistical process and the number of secondary particles $\langle N \rangle$ is proportional to the energy E of the incident particle.
- The different response of the materials to electrons, muons and hadrons can be exploited for particle identification.
- Their fast time response allows operation at high particle rates, and the patterns of energy deposition can be used for real-time event selection.

3.4.1 Electromagnetic shower development

The theory of electromagnetic shower development is relatively simple. Electrons and positrons lose energy by ionization and by radiation. The first process dominates at low energy, the second one at high energy. Photons interact either through the photoelectric effect, Compton scattering or pair production. The photoelectric effect dominates at low energies, pair production at high energies. So in our case, for electrons the loss of energy is dominated by bremsstrahlung, for photons by pair production.

E.M. shower model

A simplified electromagnetic shower model in a homogeneous detector has the following assumptions: we assume a material with radiation length of X_0 and we suppose that we have 2^t particles after $t \cdot X_0$ radiation lengths, each with energy $\frac{E}{2^t}$. So the shower stops when $E < E_C$ and the number of particles generated along the path is:

$$N_{\max} = 2^{t_{\max}} = \frac{E_0}{E_C} \quad (3.15)$$

The maximum expansion of the shower is obtained at:

$$t_{\max} \propto \log \left(\frac{E_0}{E_C} \right) \quad (3.16)$$

Molière radius

The lateral development of the shower is described by the **Molière Radius** ρ_M :

$$R_M \approx (21 \text{ MeV}) \frac{X_0}{E_C} \quad (3.17)$$

It is important to note that both X_0 and ρ_M are defined for the asymptotic energy regime ($> 1 \text{ GeV}$).

Transversally, the 95% of the energy of shower is contained in a cone of radius $R \sim 2\rho_M$. For lateral shower containment, material differences are much smaller than longitudinally. In addition, there is no energy dependence. A given (sufficiently long) cylinder will thus contain the same fraction of the energy from 1 GeV electromagnetic showers as from 1 TeV ones. Some examples are showed in Figures 3.11 and 3.12.

3.4.2 Hadronic shower development

Nuclear interaction length

Showers generated and developed by hadrons are affected by strong interactions, characterized by the **nuclear interaction length** λ_{int} , namely the average distance hadrons travel before inducing a nuclear interaction. It is expressed in g/cm^2 and for energies up to 100 GeV it scales as:

$$\lambda_{\text{int}} \sim A^{\frac{1}{3}} \quad (3.18)$$

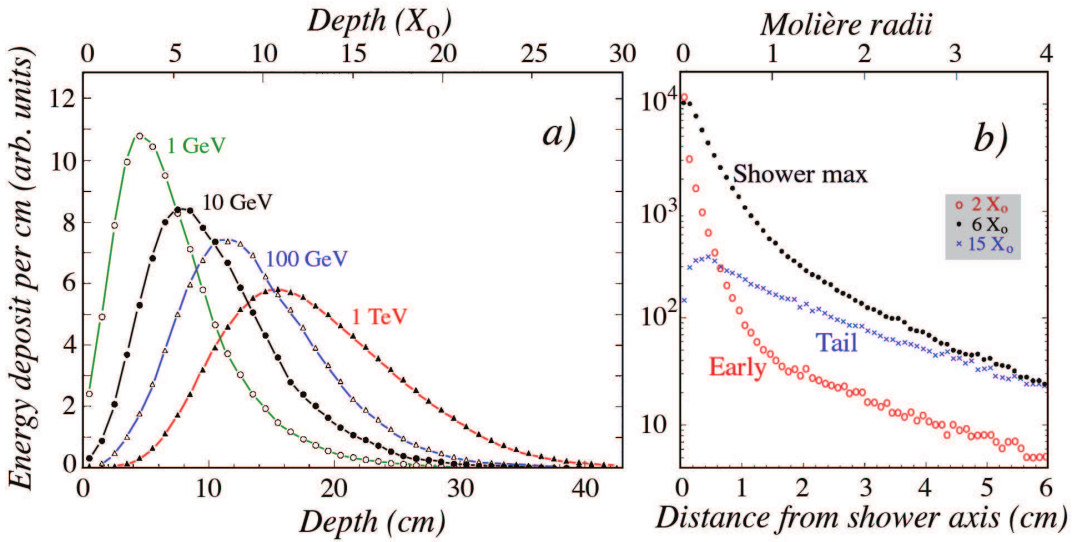


Figure 3.11: Left: the energy deposited as a function of depth for 1, 10, 100 and 1000 GeV electron showers developing in a block of copper; the integral of these curves have been normalized to the same value in order to compare the shower profiles. Right: radial distributions of the energy deposited by 10 GeV electron shower in copper at various depths.

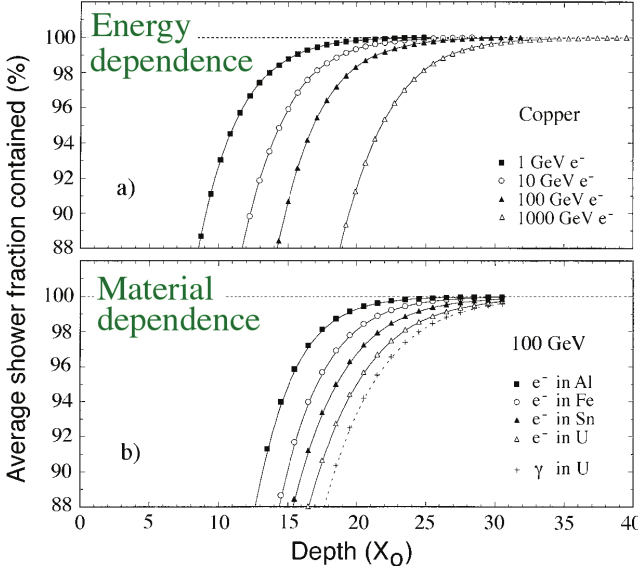


Figure 3.12: Average energy fraction contained in a block of matter with infinite transverse dimensions, as a function of the thickness of the absorber. Up: results for showers induced by electrons of various energies in a copper absorber. Down: results for 100 GeV electron showers in different absorber materials.

On average, hadronic shower profiles look very similar to the electromagnetic ones, except that the scale factor is usually much larger for the hadronic showers. For example, for copper X_0 amounts to 1.4 cm, while $\lambda_{\text{int}} = 15$ cm.

Strong interaction is responsible for:

- The production of hadronic shower particles, of which $\sim 90\%$ are pions. The neutral pions decay in 2 γ s, which develop an electromagnetic component in the shower. The fraction of this component depends on the energy of the initial particle.
- The occurrence of nuclear reactions. In these processes, neutrons and protons are released from atomic nuclei, however the nuclear binding energy of these

Effects of strong interactions

nucleons has to be provided. Therefore, the fraction of the shower energy needed for this purpose does not contribute to the calorimeter signals. This is the so called **invisible energy** phenomenon.

So we get in function of the distance travelled inside the calorimeter:

$$N(x) = N_0 e^{-\frac{x}{\lambda_{\text{int}}}} \quad (3.19)$$

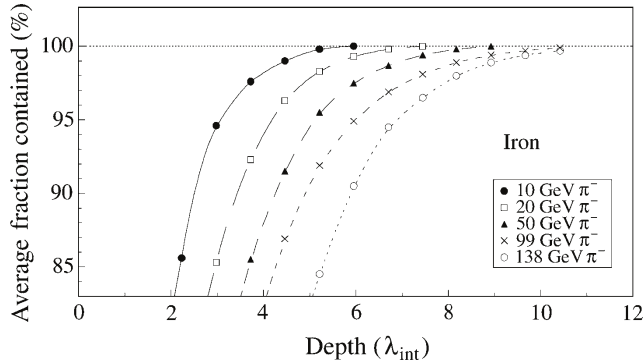


Figure 3.13: Average energy fraction contained in a block of matter with infinite transverse dimensions, as a function of the thickness of the absorber.

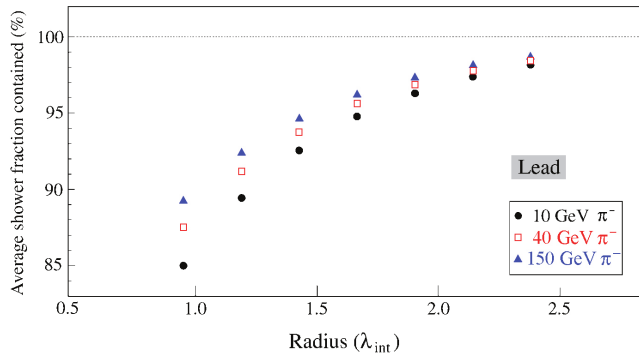


Figure 3.14: Average energy fraction contained in an infinitely long cylinder of absorber material, as a function of the radius of this cylinder, for pions of different energies showering in a lead-based calorimeter.

Consequences of nuclear interaction properties

The large majority of the non-em energy is deposited through nucleons and not through relativistic particles such as pions. These nuclear interaction properties have important consequences for calorimetetry:

- As a result of the invisible energy phenomenon, the calorimeter signals for hadrons are in general smaller than for electrons of the same energy.
- Since the electromagnetic energy fraction is energy dependent, the calorimeter is non-linear for hadron detection.

3.4.3 Classification and response of calorimeters

Calorimeters classification

Calorimeters are distinguished according to their composition into two classes:

- **Homogeneous calorimeters**, in which the absorber and the active (signal producing) medium are one and the same. They are used to get high precision results.

- **Sampling calorimeters**, in which these two roles are played by different media. These are layers of active material and high density absorber. This type of calorimeter is more common.

The calorimeter response is defined as the average calorimeter signal per unit of deposited energy. The response is thus expressed in terms of photoelectrons per GeV, pico-coulombs per MeV or something similar. Electromagnetic calorimeters are in general linear, since all the energy carried by the incoming particle is deposited through processes that may generate signals (excitation /ionization of the absorbing medium). Non-linearity is usually an indication of instrumental problems, such as signal saturation or shower leakage. An example of non-linear calorimeter data is given in Figure 3.15.

Calorimeters response

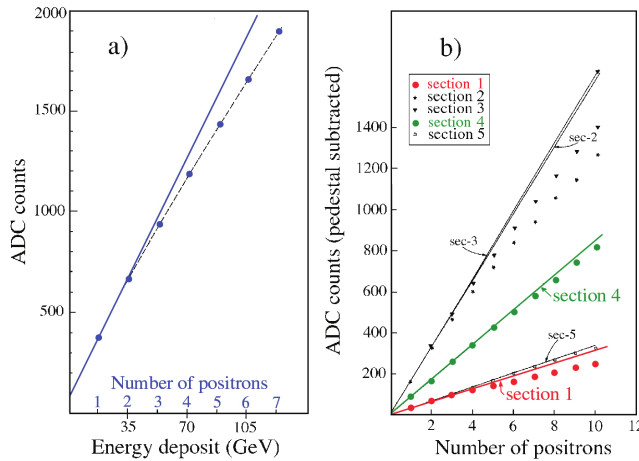


Figure 3.15: Average electromagnetic shower signal from a calorimeter read out with wire chambers operating in the “saturated avalanche” mode, as a function of energy. The calorimeter was longitudinally subdivided.

Calorimeters are based on physical processes that are inherently statistical in nature, so the precision of calorimetric measurements is determined and limited by fluctuations. We examine here the fluctuations that may affect the energy resolution. Many of them will affect electromagnetic and hadronic calorimeters, but the last one has additional term of uncertainty to be discussed later. Fluctuations and contributions to the energy resolution are:

Fluctuations

- Signal quantum fluctuations, such as photoelectron statistics:

$$\frac{\sigma_E}{E} \sim \frac{1}{\sqrt{E}} \quad (3.20)$$

- Shower leakage fluctuations:

$$\frac{\sigma_E}{E} \sim \frac{1}{\sqrt[4]{E}} \quad (3.21)$$

- Fluctuations resulting from instrumental effects, such as electronic noise, light attenuation, structural non-uniformities.

$$\frac{\sigma_E}{E} \sim \frac{1}{E} \quad (3.22)$$

- Sampling fluctuations:

$$\frac{\sigma_E}{E} \sim \text{const} \quad (3.23)$$

So, the calorimeter energy resolution has different contribution from several fluctuation processes, which add in quadrature:

$$\sigma_T^2 = \sigma_1^2 + \sigma_2^2 + \cdots + \sigma_n^2 = \sigma_1 \oplus \sigma_2 \oplus \cdots \oplus \sigma_n \quad (3.24)$$

For electromagnetic showers, the relevant contributions to the energy resolution can be summarized as:

$$\frac{\sigma}{E} = \frac{a}{\sqrt{E}} \oplus b \oplus \frac{c}{E} \quad (3.25)$$

with a the stochastic term (due to intrinsic shower fluctuations, ...), b the constant term, c the noise term.

For hadronic showers, we have some types of fluctuations as in electromagnetic showers, however, there are some additional effects that tend to dominate the performance of hadron calorimeters.

- Fluctuations in visible energy play a role in all hadron calorimeters and form the ultimate limit to the achievable hadronic energy resolution. So this is an irreducible contribution.
- Fluctuations in the electromagnetic shower fraction causes differences between p and π induced showers since in p showers there are no π^0 .

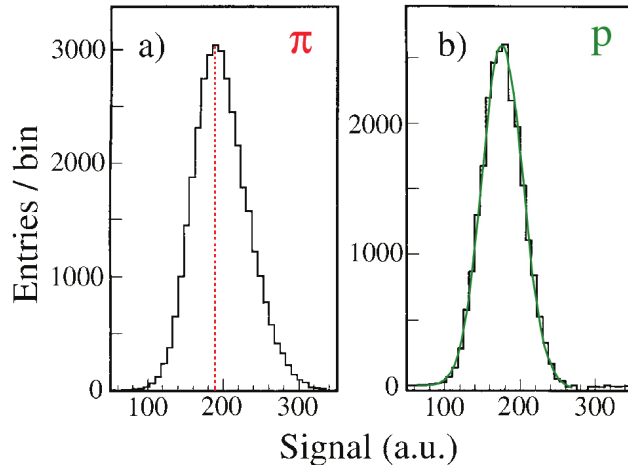


Figure 3.16: Signal distributions for 300 GeV pions and protons detected with a quartz-fiber calorimeter. The curve on the right represents the result of a gaussian fit to the proton distribution.

In the case of hadron calorimeter, the relation used before does not describe the energy resolution due to the two additional effects. For the majority of calorimeters the energy resolution can be approximated by:

$$\frac{\sigma}{E} = \frac{a}{\sqrt{E}} + b \quad (3.26)$$

where a can reach values of 90% and b can be around few %. Therefore, why do we build hadronic calorimeters? In HEP experiments we do not measure single hadrons, we do not reconstruct p , π , etc. We reconstruct jets! Jet reconstruction is complex and

TODO

3.4.4 Particle identification

TODO

Short lived particles are identified through the resonance. Stable or long lived particles are identified exploiting time of flight, Cerenkov, energy loss, combination of tracking and calorimeter.

Chapter 4

Cross section of $e^+e^- \rightarrow \mu^+\mu^-$ and $e^+e^- \rightarrow hh$

The first is a quantum electromagnetic process and it is relatively simple to compute its cross section at first order. It is also our benchmark when we start to study the second process.

Lecture 6.
 Wednesday 25th
 March, 2020.
Compiled:
 Wednesday 10th
 June, 2020.

4.1 Muon-Antimuon pair production: $e^+e^- \rightarrow \mu^+\mu^-$

The idea is now to study the cross section of the first process $e^+e^- \rightarrow \mu^+\mu^-$. The matrix elements for this process can be constructed by breaking the process down into components. First, the e^+e^- state is annihilated by an electromagnetic current. This current couples to a quantum state of electromagnetic excitation. Finally, this state couples to another current matrix element describing the creation of the muon pair. These passages can be drawn in a Feynman diagram in a very simple way, as in Figure 4.1.

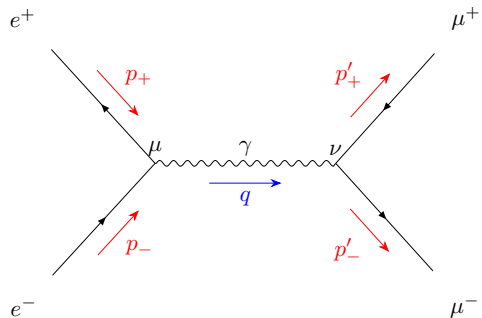


Figure 4.1: Feynmann diagram of $e^+e^- \rightarrow \mu^+\mu^-$.

The intermediate photon state can be described as a Breit-Wigner resonance at zero mass. Taking the limit of zero resonance mass in the Breit-Wigner formula, it would then contribute to the scattering amplitude by a factor:

$$\frac{1}{q^2 - m_R^2 + \frac{i}{2}m_R\Gamma_R} \sim \frac{1}{q^2} \quad (4.1)$$

where q is the momentum carried by the photon from the initial to the final state. Moreover, we consider the reaction at energies large compared to the muon mass and, certainly, very far from the mass shell condition $q^2 = 0$ for a photon, therefore we approximate: $m_e = m_\mu = 0$. A resonance contributing to an elementary particle

Description as a
 Breit-Wigner
 resonance

Virtual particle definition and matrix element

reaction very far from its mass shell is called a **virtual particle**. In this case, we say that the reaction is mediated by a **virtual photon**.

So, the matrix element reads:

$$\mathcal{M}(e^+e^- \rightarrow \mu^+\mu^-) = (-e) \langle \mu^+\mu^- | j^\mu | 0 \rangle \frac{1}{q^2} (-e) \langle 0 | j_\mu | e^+e^- \rangle \quad (4.2)$$

The operator structure $j^\mu j_\mu$ that appears in Eq. 4.2 is called **current-current interaction**.

4.1.1 Properties of massless spin- $\frac{1}{2}$ fermions

We will focus now on the properties of the massless spin- $\frac{1}{2}$ fermions in order to evaluate Eq. 4.2.

The dynamics of fermions and the calculation of matrix elements is quite simplified in the ultrarelativistic limit, which is our case since we are considering energies so large that both the electrons and muons are moving relativistically and their masses can be neglected. In this approximation, the Dirac equation takes the form:

$$i\gamma^\mu \partial_\mu \psi = 0 \quad (4.3)$$

where:

$$\gamma^0 = \begin{pmatrix} 0 & 1 \\ 1 & 0 \end{pmatrix} \quad \gamma^i = \begin{pmatrix} 0 & \sigma_i \\ -\sigma_i & 0 \end{pmatrix} \quad (4.4)$$

It is convenient to write this representation by defining $\sigma^\mu = (1, \vec{\sigma})^\mu$ and $\bar{\sigma}^\mu = (1, -\vec{\sigma})^\mu$, so:

$$\gamma^\mu = \begin{pmatrix} 0 & \sigma^\mu \\ \bar{\sigma}^\mu & 0 \end{pmatrix} \quad (4.5)$$

Moreover, we will write $\Psi = (\psi_L, \psi_R)$, so the Dirac equation splits into 2-component equations:

$$i\bar{\sigma} \cdot \partial \psi_L = 0 \quad (4.6a)$$

$$i\sigma \cdot \partial \psi_R = 0 \quad (4.6b)$$

The fields ψ_L and ψ_R annihilate different electron states and create different positron states. These states are not connected by the Dirac equation in this massless limit. When we couple the Dirac equation to electromagnetism, we modify the derivative to include the A_μ field:

$$\partial_\mu \rightarrow D_\mu = (\partial_\mu - ieA_\mu) \quad (4.7)$$

This preserves the separation of the fields ψ_L and ψ_R and of the associated electrons and positrons. The two pieces of the Dirac field communicate only through the mass term. Thus, for zero electron mass or for very high energy where the mass can be neglected, there are essentially two different species of electrons, namely e_L^- and e_R^- . Electromagnetic interactions cannot turn electrons of one kind into the other.

Now, let's take the equation for ψ_R and let's try to find the plane wave solutions:

$$(i\partial_t + i\vec{\sigma} \cdot \nabla) \psi_R = 0 \implies \psi_R(x) = u_R(p) e^{-iEt + i\vec{p} \cdot \vec{x}} \quad (4.8)$$

where $u_R(p)$ is the 2-component spinor. For simplicity, look for a plane wave moving in the $\hat{z} =: \hat{3}$ direction: $\vec{p} = p\hat{3}$. Then:

$$(E - p\sigma^3) u_R = \begin{pmatrix} E - p & 0 \\ 0 & E + p \end{pmatrix} u_R = 0 \quad (4.9)$$

So, we get two solutions, with the following characteristics:

Gauge covariant derivative

Plane wave solutions

- $E = p > 0, S_3 = \frac{1}{2}$

So the corresponding electron moves at the speed of light and spins in the right-handed sense. The field operator $\psi_R(x)$ destroys an electron in this state.

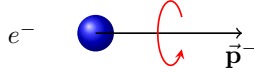


Figure 4.2: Spin up electron.

- $E = -p < 0, S_3 = \frac{1}{2}$.

This solution corresponds to the creation of a positron by the Dirac field. The positron has spin down with respect to the direction of motion.

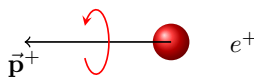


Figure 4.3: Spin down positron.

So we find an electron which is left-handed and a positron which is right-handed¹, and viceversa for the other two solutions of the ψ_L equation, a couple of right-handed electron and left-handed positron.

4.1.2 Matrix element and cross section evaluation

The first step is to evaluate the matrix element for $e_R^- e_L^+$ and $e_L^- e_R^+$ annihilations. In all, the process $e^-e^+ \rightarrow \mu^-\mu^+$ has four amplitudes for the various spin states that are permitted by helicity conservation. All of the differential cross sections have the same structure. So, by considering that:

$$|\mathcal{M}(e_R^- e_L^+ \rightarrow \mu_R^- \mu_L^+)|^2 = |\mathcal{M}(e_L^- e_R^+ \rightarrow \mu_L^- \mu_R^+)|^2 = e^4(1 + \cos \theta)^2 \quad (4.10a)$$

$$|\mathcal{M}(e_R^- e_L^+ \rightarrow \mu_L^- \mu_R^+)|^2 = |\mathcal{M}(e_L^- e_R^+ \rightarrow \mu_R^- \mu_L^+)|^2 = e^4(1 - \cos \theta)^2 \quad (4.10b)$$

we have for example, for $e_R^- e_L^+ \rightarrow \mu_R^- \mu_L^+$:

$$\begin{aligned} \sigma &= \frac{1}{2E \cdot 2E \cdot E} \int d\Pi_2 |\mathcal{M}|^2 \\ &= \frac{1}{2E_{CM}^2} \frac{1}{8\pi} \int \frac{d\cos \theta}{2} e^4(1 + \cos \theta)^2 \end{aligned} \quad (4.11)$$

and for $e_R^- e_L^+ \rightarrow \mu_L^- \mu_R^+$:

$$\begin{aligned} \sigma &= \frac{1}{2E \cdot 2E \cdot E} \int d\Pi_2 |\mathcal{M}|^2 \\ &= \frac{1}{2E_{CM}^2} \frac{1}{8\pi} \int \frac{d\cos \theta}{2} e^4(1 - \cos \theta)^2 \end{aligned} \quad (4.12)$$

With some algebra, we get the differential cross sections:

Matrix element evaluation for the all possible annihilations

¹We can consider the helicity $h = \hat{p} \cdot \vec{S}$ to describe the solutions. So we get $h = +\frac{1}{2}$ for the left-handed electron and $h = -\frac{1}{2}$ for the right-handed positron.

Differential cross section

$$\frac{d\sigma}{d\cos\theta} = \frac{\pi\alpha^2}{2E_{CM}^2}(1 + \cos\theta)^2 \quad \text{for } e_R^-e_L^+ \rightarrow \mu_R^-\mu_L^+ \text{ and } e_L^-e_R^+ \rightarrow \mu_L^-\mu_R^+ \quad (4.13a)$$

$$\frac{d\sigma}{d\cos\theta} = \frac{\pi\alpha^2}{2E_{CM}^2}(1 - \cos\theta)^2 \quad \text{for } e_R^-e_L^+ \rightarrow \mu_L^-\mu_R^+ \text{ and } e_L^-e_R^+ \rightarrow \mu_R^-\mu_L^+ \quad (4.13b)$$

Cross section result At the end, we get the final result:

$$\sigma = \frac{4\pi\alpha^2}{3E_{CM}^2} \quad (4.14)$$

What is important to remember is that the cross section goes as the inverse squared of the energy in the center of mass. This is a common behaviour for electromagnetic interactions. However, at very high energies this behaviour is broken and there are corrections to consider.

How can we measure muons in a given polarization state? Actually, this is very difficult and it is not possible with the odiern technology, so we can measure only in average.

Lecture 7.

Tuesday 31st

March, 2020.

Compiled:

Wednesday 10th

June, 2020.

4.2 Hadron production: $e^+e^- \rightarrow \text{hadrons}$

With the QED process $e^+e^- \rightarrow \mu^+\mu^-$ as a reference point, we can now discuss the process of e^+e^- annihilation to hadrons. The main products of this reaction are observed to be π and K mesons. We will consider the ultrarelativistic regime, so we will consider this process at multi-GeV center of mass energies.

Before beginning with the discussion, we have to remember that hadrons are formed by quarks. Imagine that we are at center of mass energies at which we can ignore the quark masses. Then, since quarks are spin- $\frac{1}{2}$ particles, the structure of the QED cross section for quark pair production is exactly the same as that in the process of muon pair production that we have just analyzed. By stopping here, we are ignoring the effects of the strong interaction, which play an essential role in forming the mesons that appear in the final state. However, this model can be useful as an estimate of the order of magnitude of the cross section or as a reference value.

The changes in the calculations are the following three corrections:

- First, σ depends on E_{CM} , so we must sum over the relevant quark species produced at the given energy. Remember that we can ignore the masses, at the energy we consider, with a good approximation.
- Second, we need to change the value of the electric charge of the produced particles, from -1 for the muon to $Q_f = +\frac{2}{3}$ for u, c , and $Q_f = -\frac{1}{3}$ for d, s, b . The matrix element \mathcal{M} contains one power of the final electric charge, so the cross section is proportional to Q_f^2 .
- Finally, quarks carry a hidden quantum number called color, which can take three values. We need to sum over the final color states in computing the total cross section.

Differential cross section

Thus, these corrections lead to the same angular distribution as before for the muon pair production:

$$\frac{d\sigma}{d\cos\theta} \sim (1 + \cos^2\theta) \quad (4.15)$$

Cross section

while the total cross section is modified to:

$$\sigma(e^+e^- \rightarrow \text{hadrons}) = \sum_f 3Q_f^2 \frac{4\pi}{3} \frac{\alpha^2}{E_{\text{CM}}^2} \quad \text{with } f = u, d, s, c, b \quad (4.16)$$

Note that the quark top t is not included in the sum since its mass is very large and the approximation made before doesn't hold if we include it.

Another quantity that we can analyze is the ratio:

$$R = \frac{\sigma(e^+e^- \rightarrow \text{hadrons})}{\sigma(e^+e^- \rightarrow \mu^+\mu^-)} = \sum_f 3Q_f^2 = \begin{cases} 2 & \text{for } u, d, s \\ 3 \cdot \frac{1}{3} & \text{for } u, d, s, c \\ 3 \cdot \frac{2}{3} & \text{for } u, d, s, c, b \end{cases} \quad (4.17)$$

Branching Ratio

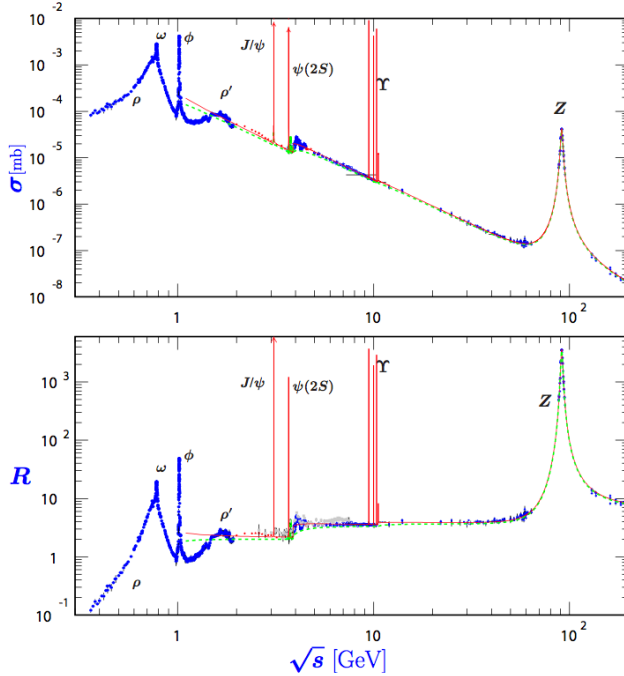


Figure 4.4: Measurements of the total cross section for e^+e^- annihilation to hadrons as a function of energy. The lower figure shows the ratio R . The green dotted curve is the prediction we have found in Eq. 4.17. The vertical lines are the μ resonances, which are very narrow compared to the hadronic ones.

The prediction for the angular distributions can also be tested experimentally. Before considering any method of detailed comparison, we need to ask what $e^+e^- \rightarrow$ hadrons events actually look like at high energies. Figure 4.5 shows a typical event at $E_{\text{CM}} = 91$ GeV. The tracks are mostly charged pions and kaons. The tracks clearly form two bundles, with π and K mesons moving in opposite directions. We call such a bundle of hadronic tracks a **jet**. The final states of e^+e^- annihilation to hadrons at high energy typically consist of two back-to-back jets.

Note that quarks are not observed in isolation, but only as constituents of hadrons. However, it is not hard to imagine that a high-energy quark might induce the creation of more quark-antiquark pairs and that all of these might reform into pions and other hadrons. In this understanding, the central axes of the jets would be proxies for the original directions of the quarks. To add some experiment data concerning jet axes, Figure 4.6 shows the orientation of jet axes in e^+e^- annihilation to hadrons at $E_{\text{CM}} = 91$ GeV as a function of $|\cos \theta|$ (and not just $\cos \theta$ since it is difficult to distinguish quark jets from antiquark jets). The functional form is very close to $(1 + \cos^2 \theta)$. The question we'll try to answer is: how is it possible that the strong interactions can be strong and yet these predictions for hadronic processes can be so accurate by neglecting them?

Definition of jets

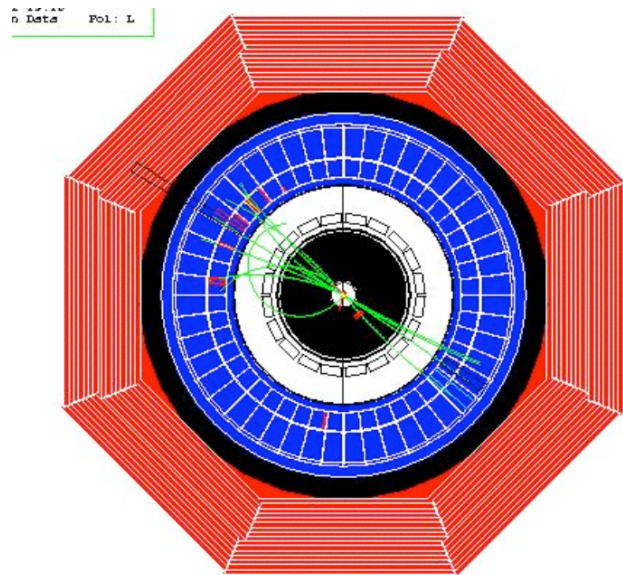


Figure 4.5: Event display from the SLD experiment showing a typical e^+e^- annihilation to hadrons event at a center of mass energy of 91 GeV.

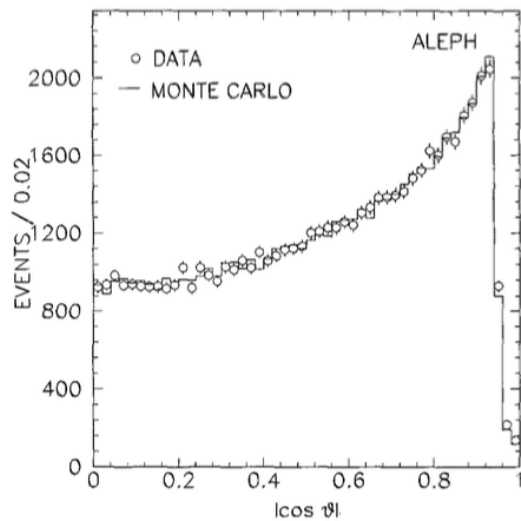


Figure 4.6: Distribution of the orientations of jet axes in e^+e^- annihilation to hadrons as a function of $|\cos \theta|$.

Chapter 5

Deep Inelastic Electron Scattering

The discovery that quarks can be described by spin- $\frac{1}{2}$ particles with simple electromagnetic interactions was actually made, not with this process, but in an earlier experiment studying a reaction in which this conclusion was even more surprising. It is the scattering $e^- p \rightarrow e^- p$.

What we observe in this process is that as the transferred momentum of electron to proton increases, elastic collisions become infrequent. Most scattering events break the proton open and produce a large number of hadrons. When the total mass of the hadrons is much larger than the original proton mass, the reaction is referred to as **deep inelastic electron-proton scattering**. Now we will see that this regime is well described using a picture in which electrons scatter from free quarks inside the proton. What is surprising is that we can ignore the strong interaction to a first approximation in the scattering of the electrons from quarks inside protons.

5.1 The SLAC-MIT experiment

Deep inelastic scattering was first studied in the 1960's at the SLAC linear electron accelerator. The purpose of the experiment was to study the structure of the proton through elastic scattering at high energies. The process can be schematized as follows:

$$e^- p \rightarrow e^- X \quad (5.1)$$

where X can be anything. The electron in the final state goes through a spectrometer in order to reconstruct its 4-momentum. The hadronic final state was ignored.

A Feynman diagram of this process is given in Figure 5.1:

Feynman diagram
of the process

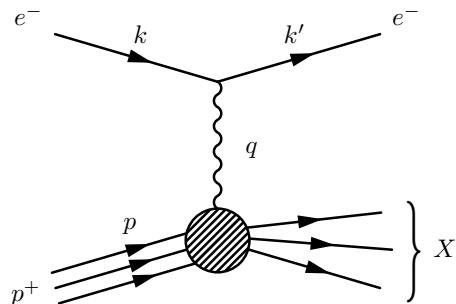


Figure 5.1: Feynman diagram of electron-proton deep inelastic scattering. Source code taken from [6].

The electron interacts with a current matrix element:

$$\langle e^-(k') | j^\mu | e^-(k) \rangle \quad (5.2)$$

Mass of the final hadronic system

The current couples to a virtual photon, which then couples to another current acting on the proton. However, the current matrix element between the proton and the particular hadronic states is not sufficiently simple to exploit for our calculations. Let's consider k the initial electron momentum and k' the final electron momentum. In the experiment, we prepare k and measure k' , so the momentum of the virtual photon in $q = (k - k')$. Then, the mass W of the final hadronic system is given by:

$$W^2 = (P + q)^2 = m_p^2 + 2P \cdot q + q^2 \quad (5.3)$$

Cross section as a function of W

Remember that the energy transfer is much larger than the mass of the proton, so we can ignore both the electron and proton mass. Moreover, q is spacelike, so there exists a frame where the energy transfer is zero and only momentum is transferred. So it is convenient to write $q^2 = -Q^2$.

The cross sections as a function of W for increasing values of $Q^2 = -q^2$ are showed in Figure 5.2. As W increases from left to right in each plot, we see the Δ , N^* , etc., baryon resonances. However, at large Q^2 , the resonances become less visible over a smooth continuum rising with W . This fact shows how complex the data collected were and the challenge of their interpretation.

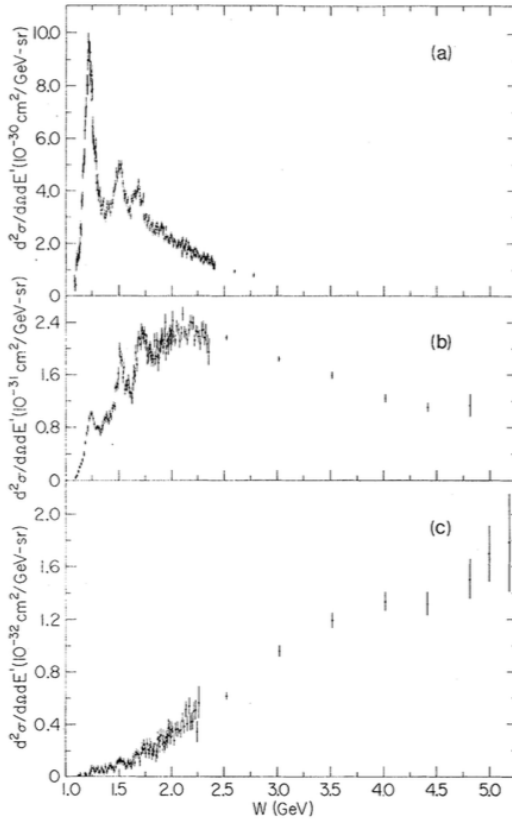


Figure 5.2: Cross section for deep inelastic ep scattering as a function of the final hadronic mass W , measured by the SLAC-MIT experiment, at low, medium, and high values of Q^2 .

5.2 The parton model

To understand the meaning of deep inelastic scattering observed data, Feynmann proposed a simple picture based on free quarks and antiquarks that he called **parton**

model. Feynman modeled the proton as a collection of constituents called **partons**. Some of these might be quarks, which we already expect as constituents of the proton. At very high energy, all partons are moving approximately in the direction of the proton, so all partons have a large component of momentum along the direction of the proton, while their transverse momenta remain of the order of the momenta within the proton bound state. So the momentum vector of a parton can be written as:

$$p^\mu = \xi P^\mu \quad (5.4)$$

where P is the total energy momentum of the proton and ξ is the fraction of this energy-momentum carried by that parton. ξ runs over the values 0 and 1.

Let $f_i(\xi)d\xi$ be the probability of finding a parton of type i carrying the momentum fraction ξ . The whole set of partons carry the total energy-momentum of the proton. This implies the sum rule:

$$\int_0^1 d\xi \sum_i f_i(\xi) \cdot \xi = 1 \quad (5.5)$$

In the parton model, deep inelastic scattering is described by the Feynman diagram in Figure 5.3.

Definition of partons

Portrait of deep inelastic scattering with a parton

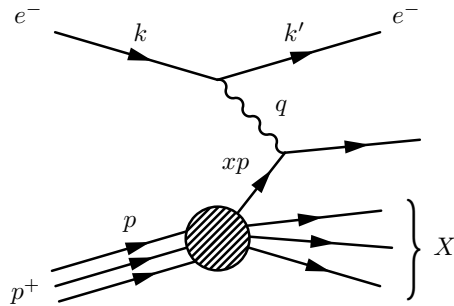


Figure 5.3: Feynman diagram of deep inelastic scattering with a parton.

We take each quark or antiquark in the proton and consider it to scatter from the electron as a pointlike spin- $\frac{1}{2}$ particle. The outgoing quark cannot be seen in isolation since it's not possible to have a quark singlet. Rather, it must turn into a jet of hadrons through processes that involve the strong interactions in a non-trivial way. Here again, the effects of the strong interactions are ignored when computing the cross section, which will be interpreted as the sum of the cross sections for all possible hadronic final states. So, the parton model cross section reads:

$$\sigma(e^- p \rightarrow e^- X) = \int d\xi \sum_f [f_f(\xi) + f_{\bar{f}}(\xi)] \sigma(e^- q(\xi p) \rightarrow e^- q) \quad (5.6)$$

5.3 Crossing symmetry

To compute the cross section, we need to evaluate the matrix elements for electron-quark scattering, which can be described by the Feynman diagram in Figure 5.4. This diagram is similar to the one for $e^- e^+ \rightarrow \mu^- \mu^+$, so the matrix element will have the same structure:

$$\mathcal{M}(e^- q_f \rightarrow e^- q_f) = (-e) \langle e^- | j^\mu | e^- \rangle \frac{1}{q^2} (Q_f e) \langle q_f | j_\mu | q_f \rangle \quad (5.7)$$

Cross section for deep inelastic scattering according to parton model

Lecture 8.
Wednesday 1st
April, 2020.
Compiled:
Wednesday 10th
June, 2020.

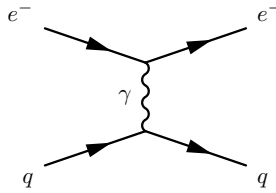


Figure 5.4: Electron-quark scattering Feynman diagram.

To evaluate this matrix element, we need the concept of **crossing symmetry**, applied in a phenomenological way. To begin, we compare the diagram in Figure 5.4 with the following one for $e^+e^- \rightarrow q\bar{q}$ in Figure 5.5.

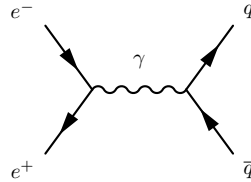


Figure 5.5: Feynman diagram representing quark pair production via electron-positron annihilation.

The two Feynmann diagrams actually show the same process, laid out in different ways in space-time. The situations with a final quark and an initial antiquark are strongly related, because the same quantum field that creates the electron destroys the positron, and similarly for a quark and antiquark. So, the matrix elements have the same functional form with appropriate identification of the external momenta.

$$\sum_{\text{spin}} |\mathcal{M}_{\text{scat}}|^2 \longrightarrow \sum_{\text{spin}} |\mathcal{M}_{\text{pair}}|^2 \quad (5.8)$$

Moreover, a theorem from QFT states that processes related by this kind of symmetry are described by the same function of external momenta. It is useful to introduce a rigorous and standard notation for the kinematic invariants of 2-body scattering process. So, we want to study:

$$1(p_1) + 2(p_2) \longrightarrow 3(p_3) + 4(p_4) \quad (5.9)$$

The Mandelstam invariants read (with $p_1^0, p_2^0 < 0$ and $p_3^0, p_4^0 > 0$):

$$s = (p_1 + p_2)^2 = (p_3 + p_4)^2 \quad (5.10a)$$

$$t = (p_1 + p_3)^2 = (p_2 + p_4)^2 \quad (5.10b)$$

$$u = (p_1 + p_4)^2 = (p_2 + p_3)^2 \quad (5.10c)$$

where:

$$s + t + u = m_1^2 + m_2^2 + m_3^2 + m_4^2 \quad (5.11)$$

We write down now the kinematics of the process in the center of mass frame and with the assumption of massless particles, in order to understand better the meaning of s, t, u . The 4-momenta are:

$$p_1 = (-E, 0, 0, -E) \quad (5.12a)$$

$$p_2 = (-E, 0, 0, E) \quad (5.12b)$$

$$p_3 = (E, E \sin \theta, 0, E \cos \theta) \quad (5.12c)$$

$$p_4 = (E, -E \sin \theta, 0, -E \cos \theta) \quad (5.12d)$$

and:

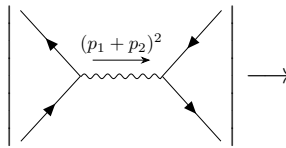
$$s = (2E)^2 = E_{\text{CM}}^2 \quad (5.13)$$

$$t = -2E^2(1 - \cos \theta) \quad (5.14)$$

$$u = -2E^2(1 + \cos \theta) \quad (5.15)$$

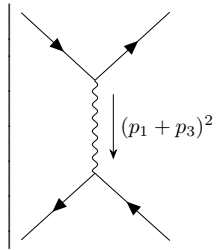
Eqs. 5.13, 5.14, 5.15 are true even for general masses. The two independent variables represented by s, t, u correspond to the CM energy and the CM scattering angle. So s, u, t provide a Lorentz-invariant way to parametrize the two key variables of a scattering process. Concerning the crossing symmetry, an easy way to implement it is to permute the three invariants as the legs of the diagram are switched between the initial and the final state.

In the last chapter, we stated that we could represent an intermediate state in a Feynman diagram with a Breit-Wigner denominator. When the intermediate state separates the initial and the final state, the denominator depends on $(p_1 + p_2)^2 = s$:

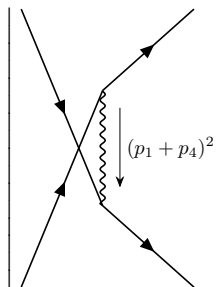


$$\rightarrow \frac{1}{(p_1 + p_2)^2 - m_R^2 + im_R\Gamma_R} = \frac{1}{s - m_R^2 + im_R\Gamma_R} \quad (5.16)$$

This type of reaction is called an ***s*-channel process**. If the amplitude depends on t , we have a ***t*-channel process**, if it depends on u , we have an ***u*-channel process**:



$$\rightarrow \frac{1}{(p_1 + p_3)^2 - m_R^2 + im_R\Gamma_R} = \frac{1}{t - m_R^2 + im_R\Gamma_R} \quad (5.17)$$



$$\rightarrow \frac{1}{(p_1 + p_4)^2 - m_R^2 + im_R\Gamma_R} = \frac{1}{u - m_R^2 + im_R\Gamma_R} \quad (5.18)$$

5.4 Cross section for electron-quark scattering

Crossing symmetry allows us to convert the calculations we did in the previous chapter for e^+e^- annihilation into calculations of the invariant amplitudes for electron-quark scattering. So, by denoting with Q_f the electric charge of the quark in question, we get the following results:

$$|\mathcal{M}(e_R^- e_L^+ \rightarrow q_R \bar{q}_L)|^2 = |\mathcal{M}(e_L^- e_R^+ \rightarrow q_L \bar{q}_R)|^2 = Q_f^2 e^4 (1 + \cos \theta)^2 = 4Q_f^2 e^4 \frac{u^2}{s^2} \quad (5.19)$$

$$|\mathcal{M}(e_R^- e_L^+ \rightarrow q_L \bar{q}_R)|^2 = |\mathcal{M}(e_L^- e_R^+ \rightarrow q_R \bar{q}_L)|^2 = Q_f^2 e^4 (1 - \cos \theta)^2 = 4Q_f^2 e^4 \frac{t^2}{s^2} \quad (5.20)$$

These expressions are correct in any frame and they yield the expressions for the crossed amplitudes after an appropriate permutation of variables. For example, consider the crossing symmetry;

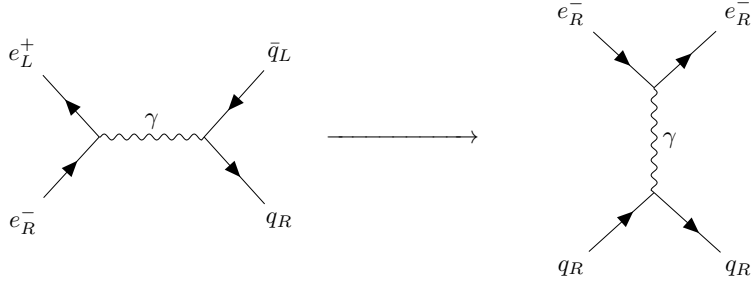


Figure 5.6: Feynman diagram representing the action of crossing symmetry.

The eq scattering diagram on the right of Figure 5.6 is obtained by moving the final antiquark \bar{q}_L to the initial state, where it becomes the quark q_R , and moving the initial positron e_L^+ to the final state, where it becomes the electron e_R^- . Note that helicity is conserved. The interchange of momenta is:

$$\left. \begin{array}{l} p_1 \rightarrow p_1 \\ p_2 \rightarrow p_3 \\ p_3 \rightarrow p_4 \\ p_4 \rightarrow p_2 \end{array} \right\} \Rightarrow \left\{ \begin{array}{l} s \rightarrow t \\ t \rightarrow u \\ u \rightarrow s \end{array} \right. \quad (5.21)$$

If we do this exchange, the matrix element for $e_R^- q_R \rightarrow e_R^- q_R$ is given by:

$$|\mathcal{M}(e_R^- q_R \rightarrow e_R^- q_R)|^2 = 4Q_f^2 e^4 \frac{s^2}{t^2} \quad (5.22)$$

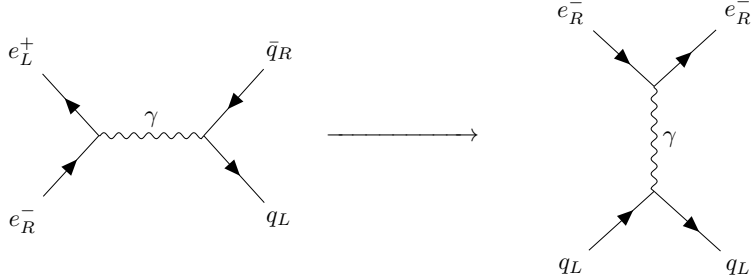


Figure 5.7: Feynman diagram representing the action of crossing symmetry..

Similarly, the crossing symmetry in Figure 5.7 produces:

$$|\mathcal{M}(e_R^- q_L \rightarrow e_R^- q_L)|^2 = 4Q_f^2 e^4 \frac{u^2}{t^2} \quad (5.23)$$

Notice that this matrix element is proportional to $u^2 \sim (1 + \cos \theta)^2$ and vanishes for backward scattering ($\cos \theta = -1$). If we look at the flow of spin angular momentum, we can see that in this case backward scattering is forbidden by angular momentum conservation. The matrix elements for the other helicity combinations allowed by helicity conservation can be obtained in the same way:

$$|\mathcal{M}(e_L^- q_L \rightarrow e_R^- q_L)|^2 = 4Q_f^2 e^4 \frac{s^2}{t^2} \quad (5.24)$$

$$|\mathcal{M}(e_L^- q_R \rightarrow e_R^- q_R)|^2 = 4Q_f^2 e^4 \frac{u^2}{t^2} \quad (5.25)$$

We can now assemble the cross section for eq scattering. Averaging over the spins in the initial state and summing over the spins in the final state, the cross section is given by:

$$\sigma(eq \rightarrow eq) = \frac{1}{2E} \frac{1}{2E} \frac{1}{8\pi} \int \frac{d\cos\theta}{2} \frac{1}{4} \sum_{\text{spins}} |\mathcal{M}(eq \rightarrow eq)|^2 \quad (5.26)$$

There is no color factor of 3 in this equation. Whatever color the quark has in the initial state, that color is passed to the quark in the final state. Summing over the matrix elements for the allowed processes, we find:

$$\frac{d\sigma}{d\cos\theta} = \frac{1}{2s} \pi \alpha^2 \frac{2}{4} \left(4Q_f^2 \frac{s^2 + u^2}{t^2} \right) = \frac{\pi Q_f^2 \alpha^2}{s} \frac{s^2 + u^2}{t^2} \quad (5.27)$$

By changing variable through $dt = \frac{1}{2}s d\cos\theta$, we can rewrite the result completely invariantly:

$$\frac{d\sigma}{dt} = \frac{2\pi Q_f^2 \alpha^2}{s^2} \frac{s^2 + u^2}{t^2} \quad (5.28)$$

Lastly, by combining Eq. 5.6 with Eq. 5.28, we obtain the parton model prediction for deep inelastic scattering cross section:

$$\sigma(e^- p \rightarrow e^- X) = \int d\xi \int d\hat{t} \sum_f [f_f(\xi) + f_{\bar{f}}(\xi)] \frac{2\pi Q_f^2 \alpha^2}{\hat{s}^2} \frac{\hat{s}^2 + \hat{u}^2}{\hat{t}^2} \quad (5.29)$$

The invariants with the hat symbol are used here for the electron-parton scattering process, reserving the symbols without hats for the full electron-proton scattering reaction.

5.5 Bjorken scaling

Let's go further. First of all, $\hat{t} = q^2 = -Q^2$ and this quantity is directly measured in the deep inelastic scattering experiment. Next, we compare s for the full $e^- p$ reaction with \hat{s} for the parton reaction:

$$s = (k + P)^2 = 2k \cdot P \quad (5.30)$$

$$\hat{s} = (k + p)^2 = 2k \cdot p = 2k \cdot \xi P \quad (5.31)$$

So it's evident that $\hat{s} = \xi s$. It is useful to define the quantity y :

$$y = \frac{2P \cdot q}{2P \cdot k} \xrightarrow{\text{proton rest frame}} \frac{q^0}{k^0} \quad (5.32)$$

The physical meaning of y is the fraction of the initial electron energy that is transferred to the proton, so it is bounded between 0 and 1. What we can do now is to express y in function of the Mandelstam invariants for the parton reaction:

$$y = \frac{2\xi P \cdot q}{2\xi P \cdot k} = \frac{2p \cdot (k - k')}{2p \cdot k} = \frac{\hat{s} + \hat{u}}{\hat{s}} \quad (5.33)$$

By reordering, we get:

$$\Rightarrow \frac{\hat{u}}{\hat{s}} = -(1 - y) \quad \text{or} \quad \hat{s}^2 + \hat{u}^2 = \hat{s}^2 [1 + (1 - y)^2] \quad (5.34)$$

Lecture 9.
Tuesday 7th April, 2020.
Compiled:
Wednesday 10th June, 2020.

All these results should be included in the expression for the cross section $\sigma(e^-p \rightarrow e^-X)$. However, there is one more important kinematic relation to consider. In the parton model, we assumed that the quark is a free point-like Dirac particle and that the electron-quark scattering is elastic. If the final quark is treated as massless particle, then:

$$0 = (p + q)^2 = 2p \cdot q + q^2 = 2\xi P \cdot q - Q^2 \quad (5.35)$$

By reordering Eq. 5.35, we can express the parameter ξ as an observable combination of momenta and we will denote it with x :

$$x = \xi = \frac{Q^2}{2P \cdot q} \quad (5.36)$$

This is a good thing to see since in the parton model a deep inelastic scatter at a fixed value of x is due to an initial parton carrying the fraction x of the initial proton momentum. By measuring x , we can sample the momentum distributions of quarks in the proton wavefunction. By combining the previous results:

$$Q^2 = xys \quad (5.37)$$

and with x fixed:

$$d\hat{t} = dQ^2 = xsdy \quad (5.38)$$

This gives our final formula for the deep inelastic scattering cross section:

$$\frac{d\sigma}{dxdy}(e^-p \rightarrow e^-X) = \sum_f xQ_f^2 [f_f(x)f_{\bar{f}}(x)] \cdot \frac{2\pi\alpha^2 s}{Q^4} [1 + (1 - y)^2] \quad (5.39)$$

with $0 < x, y < 1$.

We can rewrite this result by introducing a **form factor** F_2 , which contains the information about the proton structure and it is unknown:

$$\frac{d\sigma}{dxdy}(e^-p \rightarrow e^-X) = F_2 \cdot \frac{2\pi\alpha^2 s}{Q^4} [1 + (1 - y)^2] \quad (5.40)$$

F_2 could depend on the general kinematics of the problem, so it could be a general function of x and Q^2 :

$$F_2(x) = \sum_f xQ_f^2 [f_f(x)f_{\bar{f}}(x)] \quad (5.41)$$

What is surprising is that the predicted form depends only on x and it is independent of Q^2 . This behaviour is called **Bjorken scaling**, from the name of the physicist who predicted this simple dependence based on more advanced hypotheses about the behaviour of current matrix elements at high energy. An example of the described behaviour is showed in Figure 5.8, where all of the data falls on a single curve as a function of x .

Over the past decades, F_2 has been measured repeatedly at higher energies, using muons and neutrinos produced by proton beams of hundreds of GeV. The full world data set, collected by the Particle Data Group is showed in Figure 5.9.

In conclusion, we saw that e^-p deep inelastic scattering allows us to meaure a quantity $F_2(x)$, interpreted as a sum over parton distributions for quarks and antiquarks in the proton, and where x is the fraction of the momentum of a proton carried by a quark and $f_f(x)$, $f_{\bar{f}}(x)$ are the parton distribution functions. In particular, these ones are the probability distribution of quarks and antiquarks of flavor f in the proton as a function of x .

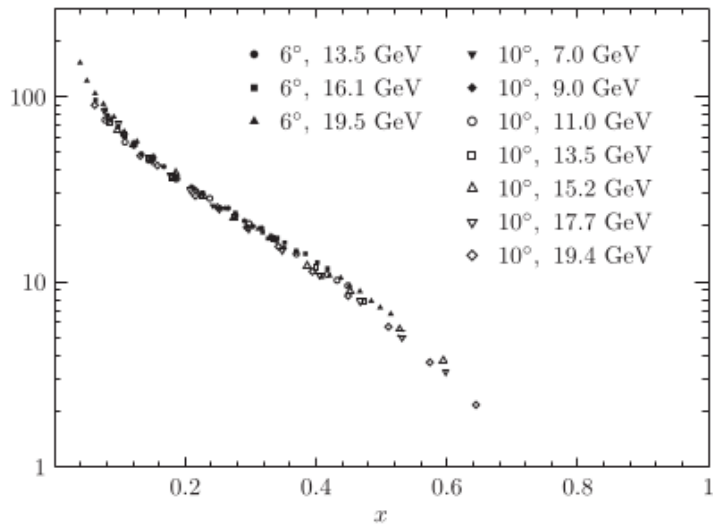


Figure 5.8: Measurements of the quantity F_2 by the SLAC-MIT experiment, at energy and angle settings giving $Q^2 > 1 \text{ GeV}^2$, plotted as a function of x .

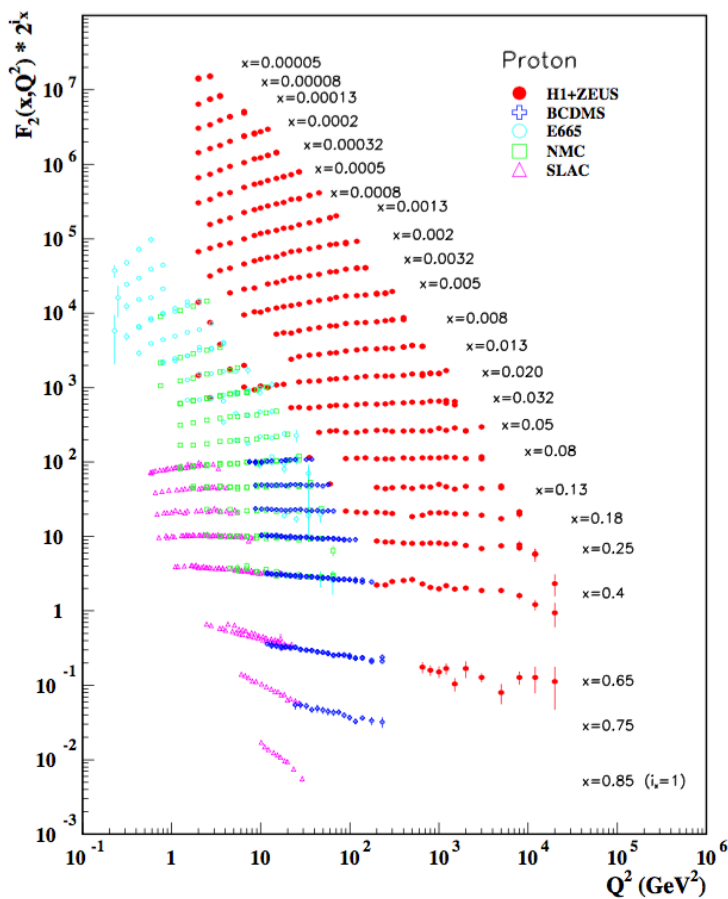


Figure 5.9: Measurements of the quantity F_2 at increasing values of x as a function of Q^2 , compiled by the Particle Data Group.

Chapter 6

Strong interactions

6.1 The gluon

6.1.1 Measurement of parton distribution functions

Let's begin by returning on the final discussion in the previous chapter. We want to know the probability density functions (PDFs) at high energies. In order to understand their utility, we take the example of the proton, composed of three quarks, in particular uud . However in its $F_2^p(x)$ factor we can have contributions from other quarks and not only by u and d . However, there are certain rules that should be satisfied:

$$\int_0^1 dx [f_u(x) - f_{\bar{u}}(x)] = 2 \quad (6.1)$$

$$\int_0^1 dx [f_d(x) - f_{\bar{d}}(x)] = 1 \quad (6.2)$$

$$\int_0^1 dx [f_q(x) - f_{\bar{q}}(x)] = 0 \quad q = s, c, b, t \quad (6.3)$$

These PDFs have to be measured experimentally, in our case the reaction $e^- p \rightarrow e^- X$ gives us one combination of these distributions. But there are other reactions that give us access to other, orthogonal, combinations.

Another important source of information is deep inelastic scattering by neutrinos. Neutrinos interact with protons through the weak interaction, and so we will need to understand the structure of that interaction to interpret this data in detail. We will see later that neutrinos also interact through a form of the current-current interaction, and that, at the level of the parton model, neutrino and antineutrino deep inelastic scattering is also described by a formula similar to the one we found. The four most important parton-level processes are:

$$\nu + d \rightarrow u + \mu^- \quad (6.4)$$

$$\nu + \bar{u} \rightarrow \bar{d} + \mu^- \quad (6.5)$$

$$\bar{\nu} + u \rightarrow d + \mu^+ \quad (6.6)$$

$$\bar{\nu} + \bar{d} \rightarrow \bar{u} + \mu^+ \quad (6.7)$$

To measure the cross section of electron-proton interaction, we can measure something similar with muons. So we are looking to processes with a muon in the final state. By measuring the sign of the final muon each event and the distribution of events in y , we can separately measure u and d quark and antiquark distributions. By looking for strange or charmed particles in the final states of deep inelastic electron and neutrino scattering, we can also estimate the heavy quark distributions. Note that the sum

Lecture 10.
Wednesday 8th
April, 2020.
Compiled:
Wednesday 10th
June, 2020.

Flavor sum rules
for PDFs

rules imply that the total numbers of heavy quarks and antiquarks in the proton are equal, but they do not imply that $f_f(x) = f_{\bar{f}}(x)$. In fact, some processes that add quark-antiquark pairs lead to different distributions.

Using data from all of these reactions, it is possible to assemble a quantitative model of the full set of pdfs. In setting up such a model, we typically divide the u and d pdfs into **valence** and **sea components**. The valence component contains exactly two u quarks and one d quark, at values of x of order 1. These distributions will have the general form in Figure 6.1. These valence quarks are accompanied by a sea of quarks and antiquarks. The sea distributions are largest at much smaller values of x . They are found to be divergent as x approaches to 0, so that the proton contains a very large number of quark-antiquark pairs carrying very small fractions of the total proton momentum. This can be seen in Figure 6.2.

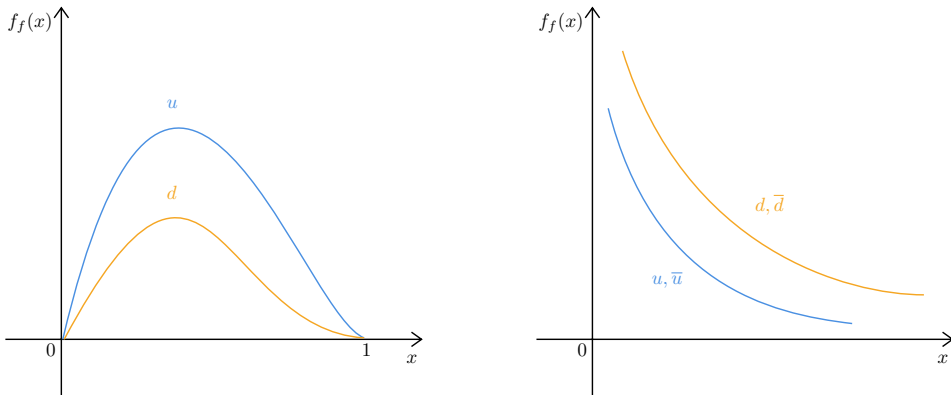


Figure 6.1: The pdfs of the proton: valence components.

Figure 6.2: The pdfs of the proton: sea components.

The divergences of the quark and antiquark pdfs must match so that the integrals in the sum rules can be finite. Feynman called the partons at very small x the **wee partons**.

These ideas can be incorporated in a quantitative model of the pdfs whose parameters are then fit to the relevant data. The fit gives explicit forms for the valence and sea pdf functions. Figure 6.3 shows the functions extracted by the NNPDF collaboration. Now, since each parton carries a fraction x of the proton's energy-momentum:

$$\int dx x \sum_i f_i(x) = 1 \quad (6.8)$$

The fraction of the total energy-momentum of the proton carried by quarks is given by the integral:

$$\frac{P_{q+\bar{q}}}{P} = \int_0^1 dx x \sum_f [f_f(x) + f_{\bar{f}}(x)] \approx 0.5 \quad (6.9)$$

With the extra factor of x , this integral easily converges as x approaches 0. So, something is still missing since we expect $\frac{P_{q+\bar{q}}}{P} \approx 0.5$. We need additional partons of another type and it shouldn't participate in deep inelastic scattering. Presumably, the proton must also contain the particle responsible for the binding of quarks into hadron bound states. This particle is called **gluon**. If gluons lead to the strong interaction, then, also, there should be a field equation for the gluon field, and there should be physical gluon particles. These particles should appear in the proton wavefunction

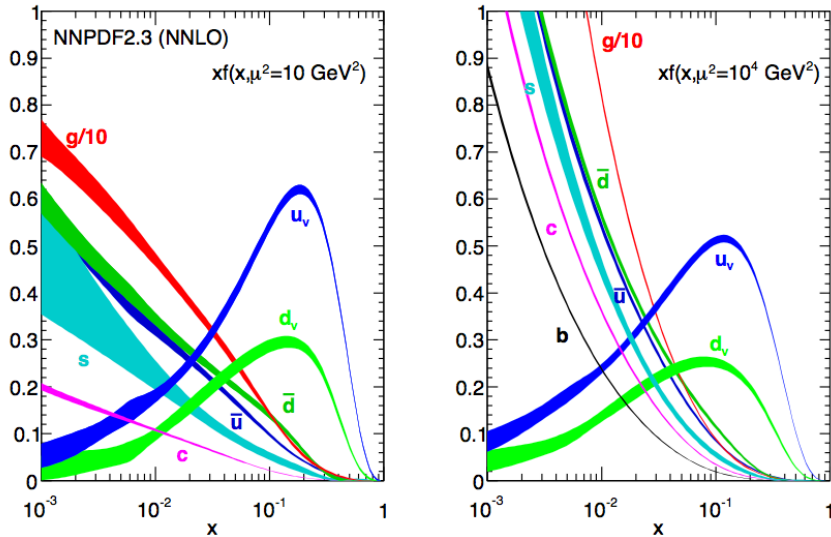


Figure 6.3: Parton distribution functions $xf_i(x)$ at $Q = 3.1 \text{ GeV}$ and at $Q = 100 \text{ GeV}$, according to the fit of the NNPDF collaboration.

and should carry some fraction of its momentum. The gluon should be radiated from the outgoing quarks and antiquarks.

If there is a gluon that interacts with quarks, it should be produced in the reaction $e^+e^- \rightarrow \text{hadrons}$. We have seen that typical events for this process at high energies are 2-jet events, due to quarks and antiquarks. If a gluon also appears as a jet, we should also see 3-jet events, in which one jet is the product of a gluon. And this is what was observed experimentally.

6.1.2 Photon emission in $e^+e^- \rightarrow q\bar{q}$

Let's start by formulating a hypothesis. The simplest one is that gluons are spin 1 particles like photons, and that they couple to the conserved quark current in the same manner as the photon. The theory of photon emission from relativistic charged particles is rather straight-forward.

We focus now on the process of e^+e^- annihilation into hadrons. The final state of two collinear particles has a momentum very close to that of the original particle, so only a small momentum transfer is required. This process is called **collinear splitting**. In particle detectors, splitting is induced by the interaction of the electron or photon with an atomic nucleus. However, when a relativistic particle is produced in a hard-scattering reaction, that reaction can give the small amount of extra momentum needed to allow splitting.

Consider, then, Feynman diagram with $e^+e^- \rightarrow q\bar{q}$ followed by photon:

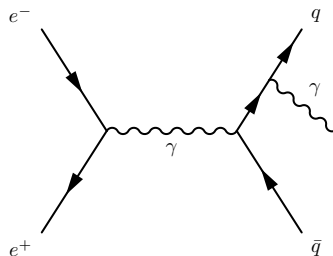


Figure 6.4: Feynman diagram of $e^+e^- \rightarrow q\bar{q} + \gamma$.

In the full process $e^+e^- \rightarrow q\bar{q} + \gamma$, photons can also be emitted from the initial-

state electron and positron, and all of these emissions must be accounted to compare with data. However, it turns out that the dominant contribution to the cross section consists of separate contributions from each of the initial and final legs, so it makes sense to study these separately.

We can study the gluon emission in e^+e^- interaction:

- $e^+e^- \rightarrow q\bar{q}g \rightarrow 3 \text{ jets}$
- $e^+e^- \rightarrow q\bar{q} \rightarrow q\bar{q}g$

6.1.3 Gluon effects on PDFs

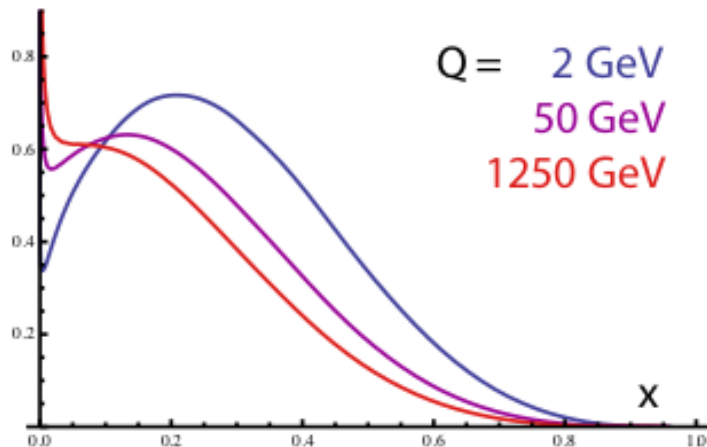


Figure 6.5: Evolution of the u quark pdf $xf_u(x)$ from $Q = 2$ GeV to $Q = 1250$ GeV, showing the flow of valence quark energy-momentum into gluons.

Lecture 11.
Wednesday 15th
April, 2020.
Compiled:
Wednesday 10th
June, 2020.

6.2 QCD

We have now accumulated enough clues to guess at the underlying theory of the strong interaction. This theory should be a theory of massless spin 1 bosons: the gluons. The basic equations of the theory should be some generalization of Maxwell's equations. It would be good if this theory accounted for two of the odd properties of hadrons. First, there is the 3-valued quantum number color, which still needs a physical interpretation. Second, there is a mystery that, although the strong interactions are strong enough to bind quarks permanently into hadrons, we can ignore the strong interactions to first order in analyzing the dynamics of quarks in e^+e^- annihilation and deep inelastic scattering.

It turns out that these clues suggest a unique proposal for the fundamental theory that describes the strong interaction. This theory is called Quantum Chromodynamics (QCD).

6.2.1 Lagrangian dynamics and gauge invariance

Starting from the Lagrangian for QED:

$$\mathcal{L} = -\frac{1}{4}F^{\mu\nu}F_{\mu\nu} + \bar{\Psi}(i\gamma^\mu D_\mu - m)\Psi \quad (6.10)$$

we want to extend this theory to strong interactions. This Lagrange density is manifestly Lorentz invariant. It is also invariant under the symmetries P , C , and T . In

addition to the space-time symmetries the Lagrangian is invariant with respect to a phase rotation of the Dirac field:

$$\Psi(x) \rightarrow e^{i\alpha} \Psi(x) \quad (6.11)$$

$$\bar{\Psi}(x) \rightarrow e^{-i\alpha} \bar{\Psi}(x) \quad (6.12)$$

This symmetry is known as global gauge invariance. In addition, it is possible to show that QED Lagrangian has also local gauge invariance property.

Local gauge invariance is a powerful constraint on the properties of the quantum theory of electromagnetism. Even at the classical level, it requires the field equations to take the form of Maxwell's equations. It is also the principle that allows the 4-vector A_μ to contain only two polarization states.

In searching for a theory of the gluon, a massless spin 1 particle with only the two transverse polarizations, it is natural to build on the idea of local gauge invariance. But, the strong interaction is not simply a slightly modified version of QED. QED, even with a stronger coupling constant, does not have 3-fermion bound states. Also, if the QED coupling were strong enough to bind quarks, it would not be possible to ignore the effects of the QED interactions as we did in our discussions of e^+e^- annihilation and deep inelastic scattering. We need a different generalization that can change these properties.

In QED, the local symmetry is based on the group $U(1)$ of phase rotations. In principle, we can find larger theories that generalize QED by enlarging the local symmetry to a larger Lie group. It turns out that the change from an Abelian to a non-Abelian local symmetry group changes the theory profoundly. It will be interesting, then, to develop the theory of spin 1 particles with non-Abelian local symmetry.

6.2.2 Vacuum polarization

To understand the uniqueness of non-Abelian gauge theories, we first need to discuss a property of the quantum corrections to QED. The leading contribution to electron-electron scattering is associated with the Feynman diagram in Figure 6.6.

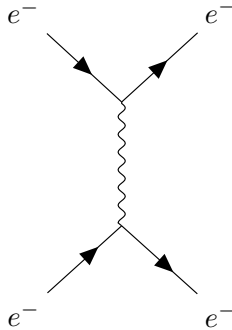


Figure 6.6: Feynman diagram of leading contribution of electron-electron scattering.

Quantum corrections to this process include the diagram in Figure 6.7, in which the virtual photon converts to an electron-positron pair, which then reforms the photon. This effect is called **vacuum polarization**. Any electromagnetic disturbance can create a virtual electron-positron pair, that is, a quantum state with an e^+e^- pair that contributes to the complete wavefunction of the state. This effect causes the vacuum state of QED to become a mixture of quantum states, most of which contain one or more e^+e^- pairs. Through the influence of these states, the vacuum in QED has properties of a dielectric medium. The virtual e^+e^- pairs can screen electric charge,

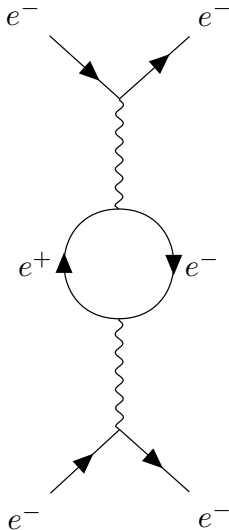


Figure 6.7: Feynman diagram of correction contribution of electron-electron scattering.

so that apparent strength of electric charge is smaller than the original strength of the charge found in the Lagrangian.

The largest separation of a virtual electron-positron pair is the electron Compton wavelength $\frac{\hbar}{m_e c}$. Pairs can be produced at all size scales smaller than this. At distances short compared to $\frac{1}{m_e}$, the screening influence of virtual electron-positron pairs is scale-invariant; charges are screened by the same factor at each length scale. Then, the apparent charge of the electron increases when the electron is probed at shorter distances or scattered with larger momentum transfer. This effect is described by the equation:

$$\frac{d}{d \log Q} e(Q) = \beta(e(Q)) \quad (6.13)$$

where Q is the momentum transfer in the process under study and $\beta(e)$ is a positive function that depends on e but not directly on Q . Assuming $Q \gg m_e$, we find:

$$\beta(e) = +\frac{e^3}{12\pi^2} \quad (6.14)$$

By solving the differential equation, we get these equivalent results:

$$e^2(Q) = \frac{e_0^2}{1 - \frac{e_0^2}{6\pi^2} \log \left(\frac{Q}{Q_0} \right)} \quad (6.15)$$

$$\alpha(Q) = \frac{\alpha_0}{1 - \frac{2\alpha_0}{3\pi} \log \left(\frac{Q}{Q_0} \right)} \quad (6.16)$$

The value of $\alpha(Q)$ changes on a logarithmic scale when $Q > m_e$. At distances larger than $\frac{1}{m_e}$, $\alpha = \frac{1}{137}$, but at shorter distances, $\alpha(Q)$ is stronger.

In Figure 6.8 there is a more detailed look at the evolution of α . We expect according to the previous results that α^{-1} should be a linear function of $\log Q$. However, at m_μ , states with virtual $\mu^+ \mu^-$ pairs also come into play and so the slope of the linear function is doubled. As Q goes above the values of quark masses, the quarks provide additional contributions to vacuum polarization. This effect is observed experimentally.

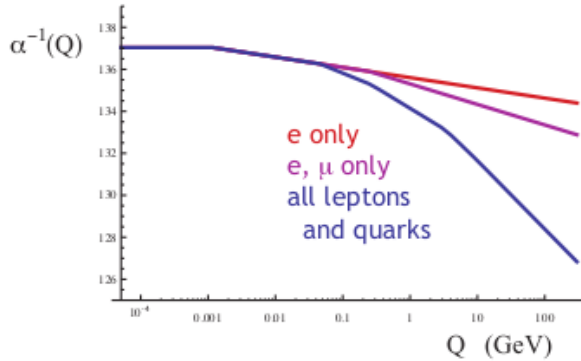


Figure 6.8: Dependence of $\alpha^{-1}(Q)$ on the momentum transfer Q predicted by the vacuum polarization effect. The effect of each particle f turns on for $Q > 2m_f$.

Another example of the effects of vacuum polarization is showed in Figure 6.9, which is the cross section plot for Bhabha scattering $e^+e^- \rightarrow e^+e^-$ at $E_{\text{CM}} = 29$ GeV. The specific effect of vacuum polarization raises the predicted cross section by about 10%, giving good agreement with the data.

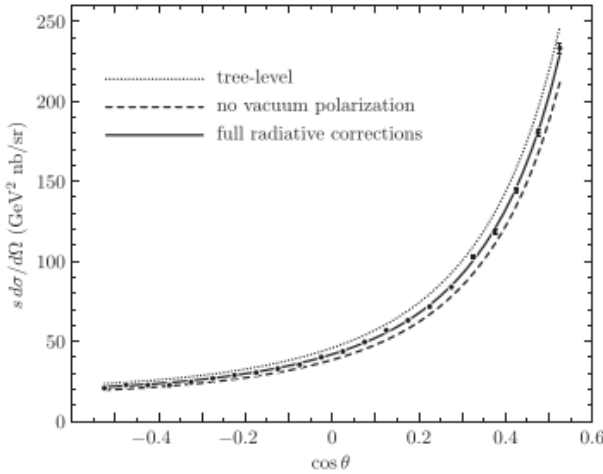


Figure 6.9: Differential cross section for $e^+e^- \rightarrow e^+e^-$ measured by the HRS experiment, showing the effect of vacuum polarization.

6.2.3 Running Coupling strong Constant

We return now to strong interactions. Non-Abelian gauge theories also have a vacuum polarization effect, corresponding to the Feynman diagram in Figure 6.10. The combination of effects is easiest to see if one considers the scattering of heavy particles, for which the exchanged gluon creates a Coulomb potential

However, this diagram actually contains two separable and distinct physical effects:

- The first effect is the first addend in Figure 6.10, where we have the creation of a virtual gluon pair by the Coulomb potential, using the nonlinear interaction of the non-Abelian theory. This effect contributes:

$$\frac{dg_s}{d \log Q} = +\frac{1}{3} \frac{g_s^3}{16\pi^2} C(G) \quad (6.17)$$

- The other contribution is the second addend in Figure 6.10, where the Coulomb potential creates a virtual gluon, which then changes the color transferred by

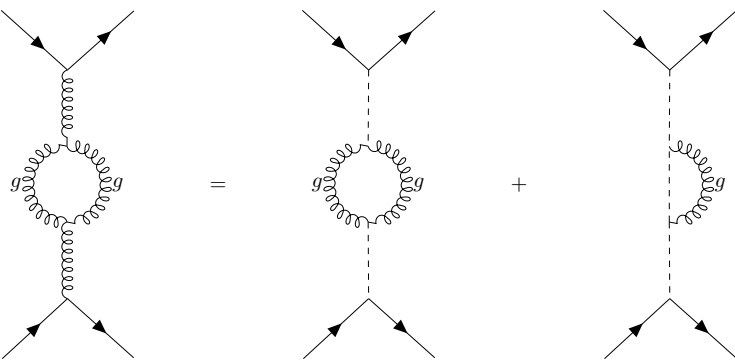


Figure 6.10: Feynman diagram representing vacuum polarization for strong interactions as a sum of two independent contributes.

the Coulomb exchange. By explicit computation, the effect of this diagram is to confuse what colors the potential is carrying. The precise size of the effect is:

$$\frac{dg_s}{d \log Q} = -\frac{12}{3} \frac{g_s^3}{16\pi^2} C(G) \quad (6.18)$$

In the non-Abelian case, this effect completely dominates the effect of vacuum polarization.

The solution for the scale-dependent coupling is:

$$\alpha_s(Q) = \frac{\alpha_s(Q_0)}{1 - \left(\frac{b_0 \alpha_s(Q_0)}{2\pi} \right) \log \left(\frac{Q}{Q_0} \right)} = \frac{\frac{2\pi}{b_0}}{\log \left(\frac{Q}{\Lambda} \right)} \quad (6.19)$$

with:

$$b_0 = 11 - \frac{2}{3} n_f \quad (6.20)$$

The new dynamics of the non-Abelian gauge theory causes $\alpha_s(Q)$ to decrease and actually tend to zero as Q increases. On the other hand, for small Q or large distances, the coupling α_s increases, apparently without bound.

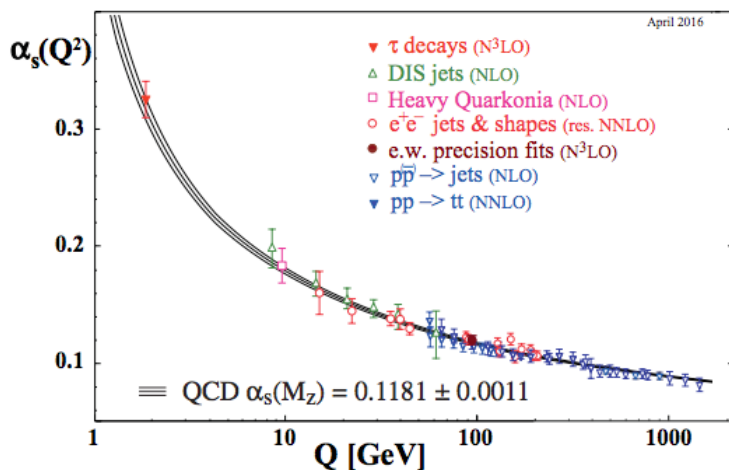


Figure 6.11: Measured values of α_s from a variety of experiments.

6.2.4 Structure of hadrons

It is possible to compute the spectrum of QCD in an expansion for large values of the coupling constant g_s . In this expansion, the gauge fields emerging from each colored particle form a tube of fixed cross section. An isolated particle with color would then carry an infinite flux tube and would have infinite energy. The only finite-energy states are those with zero total color, in other words, states that are singlets of color $SU(3)$.

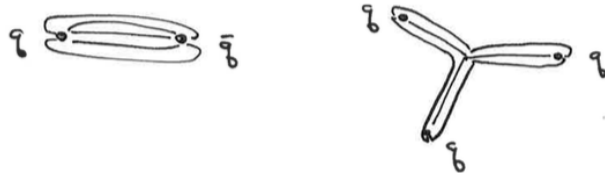


Figure 6.12: Singlets of color $SU(3)$.

This principle gives the mesons and baryons as the bound states of quarks and anti-quarks.

6.2.5 Structure of jets

The physics of quark and gluon splitting gives us a picture of the evolution from quarks and antiquarks produced as primary particles in $e^+e^- \rightarrow$ hadrons to the pions, kaons, etc. that form the hadronic final states. Begin from the initial $q\bar{q}$ pair. The quark will radiate a gluon, with the highest probability of radiation in the collinear region, $q_{1\perp} \ll \sqrt{s}$. This gluon, and also the recoiling quark, emits additional gluons, with $q_{2\perp} \ll q_{1\perp}$. Occasionally, a gluon splits to a quark-antiquark pair. So, we obtain a shower of gluons, quarks, and antiquarks. At each stage, the momentum transfer decreases. So, the quarks and gluons in the shower are all roughly collinear. Eventually, the q_\perp in the splittings falls below 1 GeV, the value of $\alpha_s(q_\perp)$ becomes large, and the strong interaction effects of QCD take over, combining quarks and antiquarks into mesons and baryons. This gives a jet of hadrons, similar to those we have seen in e^+e^- event displays.

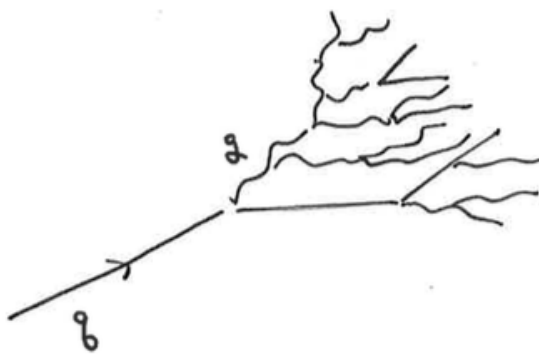


Figure 6.13: Jet of hadrons.

6.2.6 Production of top quark

Let's consider an example. A top quark pair can be produced from quark antiquark annihilation or from gluon-gluon annihilation. The possibilities are represented in Figure 6.14.

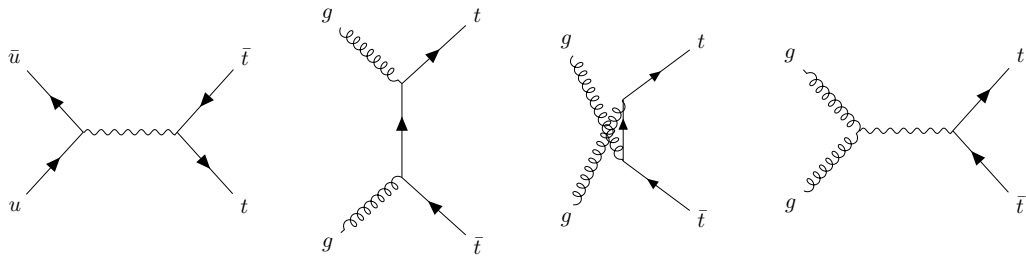


Figure 6.14: Possibilities of top quark-antiquark pair production.

Figure 6.15 shows measurements of the top quark pair production cross section at the LHC at 7, 8 and 13 TeV and the average of measurements at the Tevatron at 1.96 TeV. The blue and green curves are the QCD theory predictions for $p\bar{p}$ and pp collisions as a function of energy.

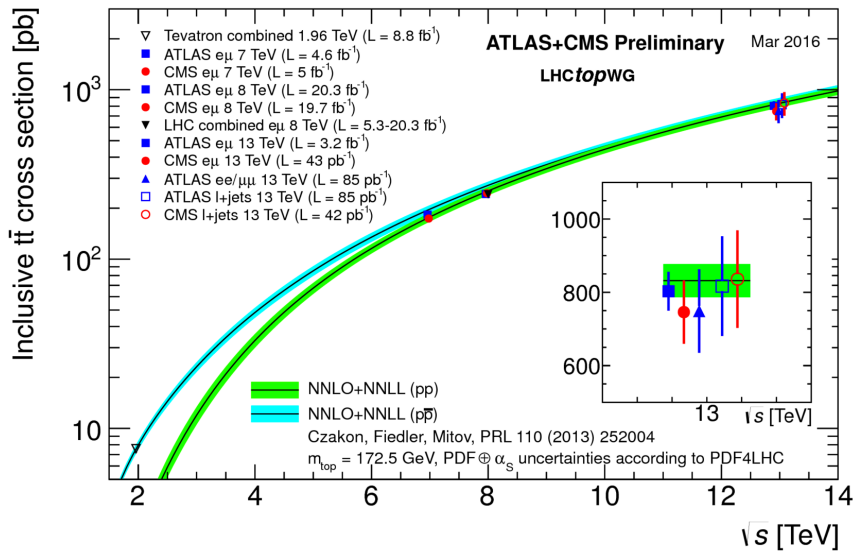


Figure 6.15: Measurements of the cross section for production of a pair of top quarks in $p\bar{p}$ and pp collisions at the Tevatron collider and the LHC, as a function of energy, compared to predictions from QCD, from the LHC Top Quark Working Group.

Chapter 7

Weak interactions

Now we turn to the other subnuclear interaction, the weak interaction. The discussion of this topic starts from the observation of the medium lifetime of some unstable particles. QCD leads to a large spectrum of mesons and baryons, most of which are unstable with decay rates of the order of 100 MeV, corresponding to lifetime of the order of 10^{-23} s. However, the lightest particles of each type are more stable. Most familiarly, the neutron is unstable by β decay:

$$n \longrightarrow pe^- \bar{\nu}_e \quad (7.1)$$

though it is very long-lived:

$$\tau(n) = 880 \text{ s} \quad (7.2)$$

The great difference with the typical hadronic lifetimes suggest that those particles, like neutron, decays are due to another subnuclear interaction, different from the strong one.

7.1 V-A Weak Theory

Historically, it all started with the study of β decay in 7.1. Before the discovery of neutrinos, it was observed that the spectrum of e^- was continuous, but this was not possible for a two-particle product decay, i.e. $n \longrightarrow pe^-$. Therefore, Pauli postulated the existence of a another invisible particle that enters in the products of β decay. Fermi called this particle **neutrino** and gave a unified description of the β decays of nuclei using a general 4-fermion interaction, like in Figure 7.1.

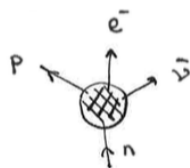


Figure 7.1: Fermi description of beta decay.

Strange particles added other elements to the discussion on weak interaction. In fact, S (strangeness) is conserved in strong production of strange particles, but S must be violated in their decay. It was found:

$$K^0 \xrightarrow{P=+1} \pi^+ \pi^- \quad (7.3)$$

$$K^0 \xrightarrow{P=-1} \pi^+ \pi^- \pi^0 \quad (7.4)$$

Lecture 12.
*Tuesday 21st April,
2020.*
Compiled:
*Wednesday 10th
June, 2020.*

It seemed impossible that these decays with final state $P = +1$ and $P = -1$ could belong to the same particle, since parity was known to be an almost perfect symmetry of atomic physics and nuclear physics. In 1956, parity violation was confirmed by the experiment of Madame Wu with the study of the decay of polarized Co^{60} nuclei.

In 1958, it was proposed a model of the weak interaction based on the idea that parity is maximally violated by this type of interaction and this model was called **V-A theory**. Moreover, the V-A theory proposed that all weak interaction matrix elements could be derived from a current-current interaction of the form:

$$\mathcal{M} = \left\langle \frac{4G_F}{\sqrt{2}} j_L^{\mu+} j_{\mu L}^- \right\rangle \quad (7.5)$$

where:

$$j_L^{\mu+} = \mu_L^\dagger \bar{\sigma}^\mu e_L + u_L^\dagger \bar{\sigma}^\mu d_L + \dots \quad (7.6)$$

$$j_L^{\mu-} = e_L^\dagger \bar{\sigma}^\mu \nu_L + d_L^\dagger \bar{\sigma}^\mu u_L + \dots \quad (7.7)$$

with e, μ, u, d representing the lepton and quark fields. What is important to observe is that only the left-handed components of the Dirac field appear in Eqs. 7.6 and 7.7. The name “V minus A” of the theory comes from rewriting:

$$u_L^\dagger \bar{\sigma}^\mu D_L = \bar{u} \gamma^\mu \left(\frac{1 - \gamma^5}{2} \right) d = \frac{1}{2} [\bar{u} \gamma^\mu d - \bar{u} \gamma^\mu \gamma^5 d] \quad (7.8)$$

which is a difference of the **Vector** and the **Axial** vector currents. Concerning the parameter G_F , it is called **Fermi constant** and it has the dimensions of GeV^{-2} :

$$G_F = 1.166 \cdot 10^{-5} \text{ GeV}^{-2} \quad (7.9)$$

7.1.1 Experimental tests: muon decay

Although V-A theory is quite simple, it makes a number of detailed and rather unexpected predictions for weak interaction processes that are confirmed by experiment. Let's start with the muon decay. The process under study is the following:

$$\mu^- \longrightarrow e^- + \bar{\nu}_e + \nu_\mu \quad (7.10)$$

The Feynman diagram of the process is in Figure 7.2.

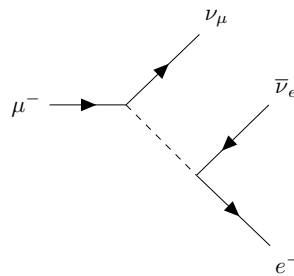


Figure 7.2: Feynman diagram of muon decay process.

Using the various fermion fields to destroy and create initial and final particles, the matrix element is:

$$\mathcal{M} \frac{4G_F}{\sqrt{2}} u_L^\dagger(p_\nu) \bar{\sigma}^\mu u_L(p_\mu) u_L^\dagger(p_e) \bar{\sigma}_\mu v_L(p_{bar\nu}) \quad (7.11)$$

From this result we can calculate the energy spectrum:

$$\frac{d\Gamma}{dE'} = \frac{G_F^2}{12\pi^3} m_\mu^2 E'^2 \left(8 - \frac{4E'}{m_\mu} \right) \quad (7.12)$$

$$\Gamma = \frac{1}{\tau} = \int d\Gamma = \int dE \frac{d\Gamma}{dE} = \frac{G_F^2 m_\mu^5}{192\pi^3} \quad (7.13)$$

where E' is the energy of e^- . A plot of the results is in Figure 7.3.

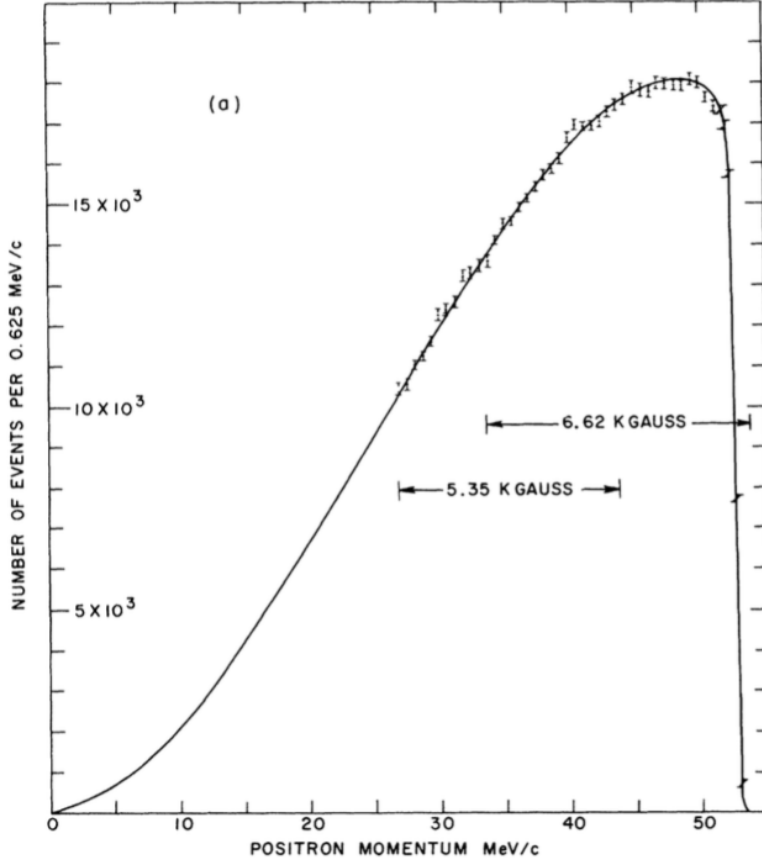


Figure 7.3: Energy spectrum of positrons emitted in muon decay $\mu^+ \rightarrow e^+ + \bar{\nu}_\mu + \nu_e$, and comparison to the V-A prediction.

The comparison of the total rate formula with the measured value of the muon lifetime gives a very accurate value of G_F :

$$G_F = (1.1663787 \pm 0.0000006) \cdot 10^{-5} \text{ GeV}^{-2} \quad (7.14)$$

There is one more interesting aspect of the prediction for muon decay. At the endpoint of e^- spectrum ($x_e = 1$), the configuration of the electron and the neutrinos is the one in Figure 7.4.

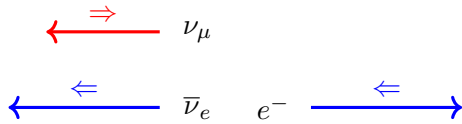


Figure 7.4: Configuration of electron and neutrinos in muon decay.

The ν_μ must be left-handed, the $\bar{\nu}_e$ must be right-handed, and the electron must be left-handed. So the angular momenta of the neutrinos cancel and the total angular

momentum in the final state is carried by the electron spin. This implies that the electron must be emitted in a direction opposite to the spin of the muon. In particular, the predicted distribution for electrons at the endpoint is:

$$\frac{d\Gamma}{d \cos \theta} \sim (1 - \cos \theta) \quad (7.15)$$

with a maximum when the electron is moving opposite to the muon spin and a zero when the electron is parallel to the muon spin. This prediction was checked explicitly in an experiment at the TRIUMF laboratory in Vancouver, Canada, in which μ^+ s from pion decay were stopped in an absorber and then allowed to decay. Muons from pion decay are perfectly polarized, a magnetic field was used to precess the spins of the stopped muons, and the decay electrons were counted as a function of time. The signal was seen to oscillate as the muons precess, as we can see from the data in Figure 7.5.

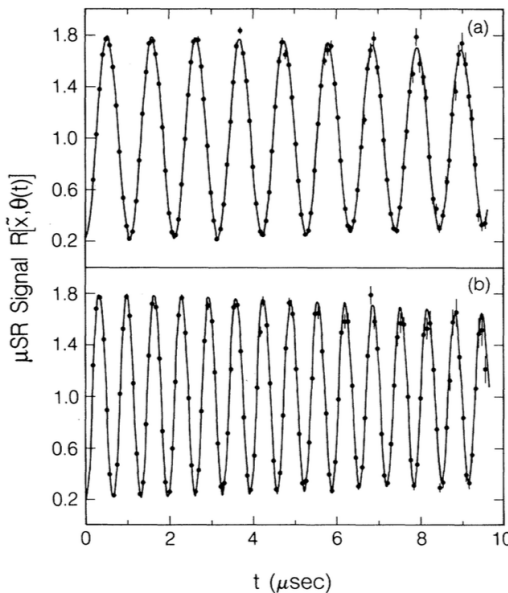


Figure 7.5: Signal rates as a function of time, as the muon spin is precessed in a magnetic field, in the TRIUMF measurement of the correlation of the positron direction with the muon spin.

7.1.2 Experimental tests: pion decay

The processes we are studying now is:



According to the V-A theory, the electron and the muon have identical weak interactions. However, the ratio of branching ratios for these processes is observed to be:

$$\frac{\Gamma(\pi^- \rightarrow e^- \bar{\nu}_e)}{\Gamma(\pi^- \rightarrow \mu^- \bar{\nu}_\mu)} = 1.23 \cdot 10^{-4} \quad (7.18)$$

Why is this happening and how can this be consistent with the V-A theory? The reason hides in the characteristics of the decay. The pion has spin 0, so in the decay we have in one side the electron, in the other side the antineutrino, which is right-handed. So the electron should be right-handed in order to have the momentum

conserved. So the electron has the wrong helicity and the same is true also for the muon. What is making the difference? The difference comes from the mass. If we calculate the decay rate for the two cases, we find:

$$\Gamma(\pi^- \rightarrow \mu^- \bar{\nu}_\mu) = \frac{G_F^2 f_\pi^2 m_\pi^3}{4\pi} \frac{m_\mu^2}{m_\pi^2} \left(1 - \frac{m_\mu^2}{m_\pi^2}\right)^2 \quad (7.19)$$

$$\Gamma(\pi^- \rightarrow e^- \bar{\nu}_e) = \frac{G_F^2 f_\pi^2 m_\pi^3}{4\pi} \frac{m_e^2}{m_\pi^2} \left(1 - \frac{m_e^2}{m_\pi^2}\right)^2 \quad (7.20)$$

So, the ratio of the branching ratio is equal to:

$$\frac{\Gamma(\pi^- \rightarrow e^- \bar{\nu}_e)}{\Gamma(\pi^- \rightarrow \mu^- \bar{\nu}_\mu)} = \frac{m_e^2}{m_\mu^2} \left(\frac{m_\pi^2 - m_e^2}{m_\pi^2 - m_\mu^2} \right)^2 = 1.28 \cdot 10^{-4} \quad (7.21)$$

in good agreement with the measured value quoted in 7.18.

7.1.3 Experimental tests: neutrino scattering

It is possible to create a neutrino beam using a proton beam from a high-energy accelerator. The method is to shoot the proton beam into a target, produce pions, allow the pions to pass through an empty volume in which they can decay ($\pi^\pm \rightarrow \mu^\pm \nu_\mu, \pi^\pm \rightarrow e^\pm \nu_e$), and then absorb all of the decay products except for the neutrinos, which interact only through the weak interactions and are thus highly penetrating. For example, at Fermilab the pion beam was shot horizontally underground, so the ground had the role of the absorber (of charged particles and other ones not in study). What we can do with the neutrino beam is to study interactions with other particles. The V-A theory predicts neutrino and antineutrino reactions with quarks and antiquarks:

$$\nu_L d_L \rightarrow \mu_L^- u_L \quad (7.22)$$

$$\bar{\nu}_R u_L \rightarrow \mu_R^+ d_L \quad (7.23)$$

$$\nu_L \bar{u}_R \rightarrow \mu_L^- \bar{d}_R \quad (7.24)$$

$$\bar{\nu}_R \bar{d}_R \rightarrow \mu_R^+ \bar{u}_R \quad (7.25)$$

and similar reactions on the s and c quarks and antiquarks in the parton sea. These reactions should be seen as events with hadronic energy deposition and an outgoing muon, called **charged-current events**. The neutrino experiments also observe **neutral-current events**, with a neutrino in the final state. An example is showed in Figure 7.6.

To predict the cross section for deep-inelastic neutrino scattering, we can look at the calculations done for deep-inelastic electron scattering and do something similar. We got for the electron-quark scattering:

$$\frac{d\sigma}{d \cos \theta} = \frac{\pi Q_f^2 \alpha^2}{s} \frac{s^2 + u^2}{t^2} \quad (7.26)$$

and we derived the matrix elements:

$$|\mathcal{M}(e_L^- q_L \rightarrow e_L^- q_L)|^2 = 4Q_f^2 e^4 \frac{s^2}{t^2} \quad (7.27)$$

$$|\mathcal{M}(e_L^- q_R \rightarrow e_L^- q_R)|^2 = 4Q_f^2 e^4 \frac{u^2}{t^2} \quad (7.28)$$

In neutrino scattering, the V-A interaction fixes the helicity to be left-handed for neutrinos and quarks and right-handed for antineutrinos and antiquarks. Changing the

Lecture 13.
Wednesday 22nd
April, 2020.
Compiled:
Wednesday 10th
June, 2020.

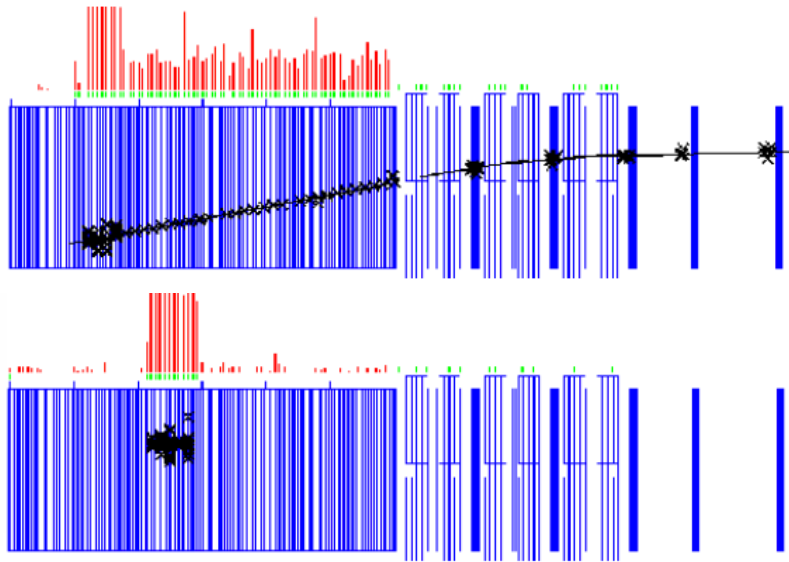


Figure 7.6: Event displays of charged-current (top) and neutral-current (bottom) neutrino deep inelastic scattering events recorded by the NuTeV experiment at Fermilab.

prefactors appropriately, the cross sections for neutrino and antineutrino scattering on u and d quarks are:

$$\frac{d\sigma}{d \cos \theta} = \frac{G_F^2}{2\pi s} \cdot s^2 \quad (7.29)$$

$$\frac{d\sigma}{d \cos \theta} = \frac{G_F^2}{2\pi s} \cdot u^2 \quad (7.30)$$

To derive the formulae for deep inelastic scattering, we integrate with the pdfs and average over the initial quark spins. We don't average over the neutrino or antineutrino spins since the neutrinos are produced completely polarized from π decay. So we get for neutrino scattering and antineutrino scattering:

$$\frac{d^2\sigma}{dxdy}(\nu p \rightarrow \mu^- X) = \frac{G_F s}{\pi} [x f_d(x) + x f_{\bar{u}}(x)(1 - y^2)] \quad (7.31)$$

$$\frac{d^2\sigma}{dxdy}(\bar{\nu} p \rightarrow \mu^+ X) = \frac{G_F s}{\pi} [x f_u(x)(1 - y^2) + x f_{\bar{d}}(x)] \quad (7.32)$$

plus small contributions from heavier sea quarks and antiquarks. If we concentrate only on the contribution of valence quarks in the proton, we expect the distributions:

$$\frac{d\sigma}{dy} \sim 1 \quad \text{for neutrinos} \quad (7.33)$$

$$\frac{d\sigma}{dy} \sim (1 - y)^2 \quad \text{for antineutrinos} \quad (7.34)$$

For neutrino scattering from nuclear targets with approximately equal numbers of protons and neutrons, the same regularities should hold.

The prediction is verified in a quite striking way, though there are small deviations from the ideal result due to the effects of antiquarks. It is possible to see this in Figure 7.7. The V-A theory is thus dramatically successful at describing the weak interactions of quarks and leptons.

7.2 Electroweak interaction

We saw that weak interaction is based on V-A theory and that neutrino interaction implies the existence of charged current (CC) and neutral current (NC). So, the

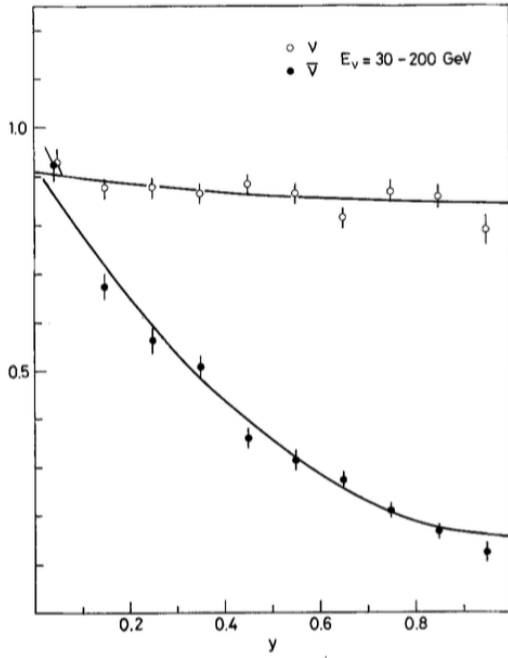


Figure 7.7: Distribution of neutrino and antineutrino deep inelastic scattering events in y , as measured by the CDHS experiment at CERN.

theory suggest that weak interaction is generated by a spin 1 boson, which will be called W^- . It must have an antiparticle, namely the W^+ , and it must be massive.

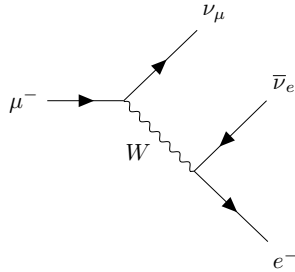


Figure 7.8: Feynman diagram of weak interaction in muon decay.

In the diagram in Figure 7.8, W^- appears as a resonance, with the Breit-Wigner denominator:

$$\frac{1}{q^2 - m_W^2} \quad (7.35)$$

But there was no sign of the q^2 -dependence in the experimental data. This implies that the W^- boson is heavier than about 30 GeV, in fact its mass is about 80 GeV. Our need for a massive spin 1 boson forces us to face a problem that we have avoided up to now: What is the wave equation for the associated massive spin 1 field? There is only one way known to solve this problem. That is to mix the two concepts of gauge invariance and spontaneous symmetry breaking.

The starting point is a gauge theory with complex fields and symmetry group $U(1)$:

$$\mathcal{L} = -\frac{1}{4}(F_{μν})^2 + |D_μφ|^2 - V(φ) \quad (7.36)$$

with:

$$D_μφ = (\partial_μ - ieQA_μ)φ \quad (7.37)$$

where Q is the charge of the field.

The next step is a gauge theory based on $SO(3)$ adding, with scalar field φ . Three bosons of $SO(3)$ are modified in 2 massive and 1 massless bosons. From this exercise we understand that we can unify the weak and the electromagnetic interactions. However, there is a problem. Particles are wrongly classified into triplets (E^+, ν, e^-) . The problem was solved by the Glashow-Salam-Weinberg theory, based on a symmetry group $SU(2) \times U(1)$. This theory contains 4 bosons, all of them massless. This is still not correct and the solution is to add a scalar field.

Lecture 14.
 Tuesday 28th
 April, 2020.
 Compiled:
 Wednesday 10th
 June, 2020.

When the Higgs was proposed, Weinberg and Salam showed that the required mass of the vector bosons and of the fermions can be acquired by the interaction with the H field. The potential of this field is:

$$V(\varphi) = -\mu^2|\varphi|^2 + \lambda(|\varphi|^2)^2 \quad (7.38)$$

The minimum of the potential is obtained by setting to zero the first derivative with respect to φ of the potential:

$$0 = -2\mu^2\varphi + 4\lambda\varphi|\varphi|^2 \implies |\varphi|^2 = \frac{\mu^2}{2\lambda} \quad (7.39)$$

If we compute the H field vacuum expectation value, we find:

$$v = \sqrt{2}\langle|\varphi|\rangle = \frac{\mu}{\sqrt{\lambda}} \quad (7.40)$$

It is different from zero and it spontaneously breaks the $SU(2) \times U(1)$ gauge symmetry. In the theory we need to introduce two coupling constants, g and g' , related to the two gauge groups. Putting all together the previous facts, it is possible to show that:

- One of the 4 bosons of theory remains massless and it is the photon.
- Two bosons are charged with mass, namely:

$$M_W = g \frac{v}{\sqrt{2}} \quad (7.41)$$

- One boson is neutral and massive, with mass:

$$M_{Z^0} = \sqrt{g'^2 + g^2} \frac{v}{2} \quad (7.42)$$

- If we define the Weinberg angle θ_W , we have:

$$\tan \theta_W = \frac{g'}{g} \quad (7.43)$$

- It holds:

$$M_W = M_Z \cos \theta_W \quad (7.44)$$

$$e = g \sin \theta_W = g' \cos \theta_W \quad (7.45)$$

W^\pm and Z^0 bosons couple to quarks and leptons. In order to describe these couplings two quantum numbers are needed: the **weak isospin** I and the **hypercharge** Y . The electric charge is then related to these quantities by:

$$Q = I_3 + \frac{Y}{2} \quad (7.46)$$

Experimentally, we see that left-handed particles couple to W^\pm bosons, but right-handed particles have not this behaviour. Quarks and leptons are grouped:

- Left-handed \Rightarrow doublet $\Rightarrow I = \frac{1}{2}$
- Right-handed \Rightarrow singlet $\Rightarrow I = 0$

Therefore the correct representation is:

$$\begin{pmatrix} \nu_L \\ e_L^- \end{pmatrix}, e_R^- \quad \begin{pmatrix} u_L \\ d_L \end{pmatrix}, u_R, d_R \quad (7.47)$$

Lecture 15.
Wednesday 29th
April, 2020.
Compiled:
Wednesday 10th
June, 2020.

7.3 Experimental tests of electroweak interaction

7.3.1 Discovery of the neutral current

The discovery of neutral currents lies in the development of the electroweak theory. The theory proposed by Sheldon Glashow, Steven Weinberg, and Abdus Salam in the 1960s tried to unify electromagnetic and weak interaction between elementary particles. Their theory predicted the existence of the W^\pm and Z^0 bosons as propagators of the weak force. Exchange of a Z^0 boson transfers momentum, spin, and energy but leaves the particle's quantum numbers unaffected. Since there is no transfer of electric charge, the exchange of a Z^0 is referred to as "neutral current". So, neutral currents were a prediction of the electroweak theory.

Their discovery takes place in the experiment Gargamelle. It was a bubble chamber at CERN designed to detect neutrinos. It was 4.8 metres long and 2 metres in diameter, weighed 1000 tonnes. It held nearly 12 cubic metres of heavy-liquid freon (CF_3Br) and not the usual liquid hydrogen. The discovery involved the search for two types of events:

- one involved the interaction of a neutrino with an electron in the liquid:



- in the other the neutrino scattered from a hadron (proton or neutron), for example:



In the latter case, the signature of a neutral current event was an isolated vertex from which only hadrons were produced. So, we can have neutral current or charged current events:



which are distinguished respectively by the absence of any possible muon, or the presence of one, and only one, possible muon.

Concerning the experimental setup, neutrino/antineutrino beams were directed to Gargamelle. To bend the tracks of charged particles, Gargamelle was surrounded by a magnet providing a 2 Tesla field. The coils of the magnet was made of copper cooled down with water, and followed the oblong shape of Gargamelle. In order to maintain the liquid at an adequate temperature several water tubes surrounded the

chamber body, to regulate the temperature. When recording an event, the chamber was illuminated and photographed. The illumination system emitted light that was scattered at 90° by the bubbles, and sent to the optics.

By this way it was possible to measure the following cross sections of the processes listed previously:

$$\frac{d^2\sigma}{dxdy}(-)_{\nu}N \rightarrow \mu^{(+)}X \quad (7.55)$$

The leptonic events have small cross-sections, but correspondingly small background. The hadronic events have larger backgrounds, most extensively due to neutrons produced when neutrinos interact in the material around the chamber. Neutrons, being of no charge, would not be detected in the bubble chamber, and the detection of their interactions would mimic neutral currents events. In order to reduce the neutron background, the energy of the hadronic events had to be greater than 1 GeV. So, the quantity we have to measure is the ratio between NC and CC events:

$$R^{\nu} = \frac{\sigma(\nu, \text{nc})}{\sigma(\nu, \text{cc})} \quad R^{\bar{\nu}} = \frac{\sigma(\bar{\nu}, \text{nc})}{\sigma(\bar{\nu}, \text{cc})} \quad (7.56)$$

Moreover, an interesting result comes out if we compute the ratio of the different cross sections:

$$r = \frac{\sigma(\bar{\nu}, -\text{cc})}{\sigma(\nu, \text{cc})} \quad (7.57)$$

In fact, it is not equal to 1. This is due to the fact that the target is made of matter and so we don't have a symmetric situation.

By July 1973, the collaboration of the experiment had confirmed as many as 166 hadronic events, and one electron event. In both cases, the neutrino enters invisibly, interacts and then moves on, again invisibly. On 3 September the collaboration published two papers on these events in the same issue of Physics Letters. In its short career at the SPS, Gargamelle succeeded in observing for the first time a touchstone weak interaction, involving only leptons, in which a muon-type neutrino hits an electron, producing an electron-neutrino and a muon. However in 1979 the chamber ceased operation after cracks had appeared that proved impossible to repair.

7.3.2 Discovery of W^{\pm} and Z^0 bosons

The discovery of the W^{\pm} and Z^0 bosons themselves had to wait for the construction of a particle accelerator powerful enough to produce them. The first such machine that became available was the Super Proton Synchrotron, where unambiguous signals of W bosons were seen in January 1983 during a series of experiments made possible by Carlo Rubbia and Simon van der Meer. The actual experiments were called UA1 (led by Rubbia) and UA2 (led by Pierre Darriulat), and were the collaborative effort of many people.

The first physics run of the CERN collider took place at the end of 1981. The total integrated luminosity recorded by the two experiments during that run was not yet sufficient to detect the W and Z bosons, but that run demonstrated that there were no conceptual obstacles to further increase the luminosity to the required values by a careful tuning of all the machines involved in the collider operation (PS, AA, SPS) and of the interconnecting beam transfer lines.

W^{\pm} bosons

The W boson decays predominantly ($\sim 70\%$) to quark–antiquark pairs ($q\bar{q}'$), which appear as two hadronic jets. Such configurations are overwhelmed by two-jet pro-

duction from hard parton scattering, hence both experiments had chosen to detect the W by identifying its leptonic decays:

$$W^\pm \rightarrow e^\pm \nu_e (\bar{\nu}_e) \quad \text{UA1 and UA2} \quad (7.58)$$

$$W^\pm \rightarrow \mu^\pm \nu_\mu (\bar{\nu}_\mu) \quad \text{UA1 only} \quad (7.59)$$

The signal from $W \rightarrow e\nu_e$ was expected to have the following features:

- the presence of a high transverse momentum (p_T) isolated electron;
- a peak in the electron p_T distribution at $\frac{m_W}{2}$ (the ‘‘Jacobian’’ peak);
- the presence of high missing transverse momentum from the undetected neutrino.

These features are the consequence of the main mechanism of W production (quark-antiquark annihilation), which results mainly in W bosons almost collinear with the beam axis, hence the decay electron and neutrino emitted at large angles to the beam axis have large p_T . We note that the missing longitudinal momentum cannot be measured at hadron colliders because of the large number of high-energy secondary particles emitted at very small angles to the beam which cannot be detected because their trajectories are inside the machine vacuum pipe. The missing transverse momentum vector (\vec{p}_T^{miss}) is defined as:

$$\vec{p}_T^{\text{miss}} = - \sum_{\text{cells}} \vec{p}_T \quad (7.60)$$

where \vec{p}_T is the transverse component of a vector associated with each calorimeter cell, with direction from the event vertex to the cell centre and length equal to the energy deposition in that cell, and the sum is extended to all cells with an energy deposition larger than zero. In an ideal detector with no measurement errors, for events with an undetected neutrino in the final-state it follows from momentum conservation that \vec{p}_T^{miss} is equal to the neutrino transverse momentum.

Figure 7.9 shows that $|\vec{p}_T^{\text{miss}}|$ distribution, as measured by UA1 from the 1982 data. There is a component decreasing approximately as $|\vec{p}_T^{\text{miss}}|^2$ due to the effect of calorimeter resolution in events without significant $|\vec{p}_T^{\text{miss}}|$, followed by a flat component due to events with genuine $|\vec{p}_T^{\text{miss}}|$. Six events with high $|\vec{p}_T^{\text{miss}}|$ in the distribution contain a high p_T electron. The \vec{p}_T^{miss} vector in these events is almost back-to-back with the electron transverse momentum vector. These events are interpreted as due to $W \rightarrow e\nu_e$ decay. This result was first announced at a CERN seminar on January 20, 1983. The results from the UA2 search for the same events was presented at a CERN seminar on the following day.

Z bosons

The process searched for Z boson discovery was:

$$Z \rightarrow e^+ e^- \quad (7.61)$$

The first step of the analysis required the presence of two calorimeter clusters consistent with electrons and having a transverse energy $E_T > 25$ GeV. Among the data recorded during the 1982–83 collider run, 152 events were found to satisfy these conditions. The next step required the presence of an isolated track with $p_T > 7$ GeV/c pointing to at least one of the two clusters. Six events satisfy this requirement, showing already a clustering at high invariant mass values, as expected from $Z \rightarrow e^+ e^-$ decay. Of these events, four were found to have an isolated tracks with $p_T > 7$ GeV/c

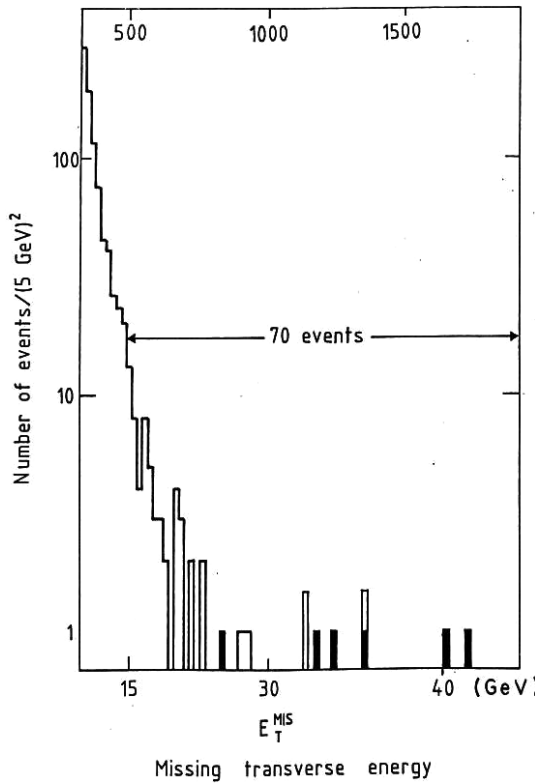


Figure 7.9: UA1 distribution of the missing transverse momentum. The events shown as dark areas in this plot contain a high p_T electron.

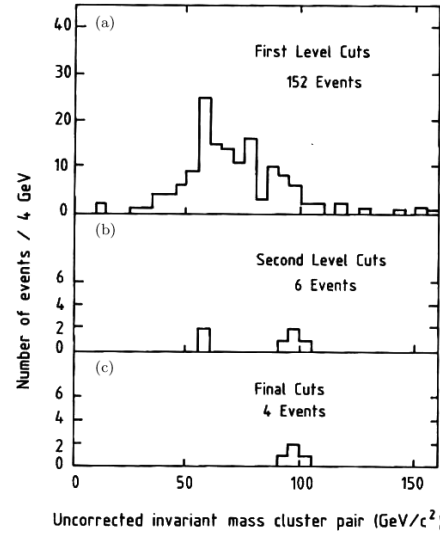


Figure 7.10: Search for the decay $Z \rightarrow e^+e^-$ in UA1.

pointing to both clusters. They were consistent with a unique value of the e^+e^- invariant mass within the calorimeter resolution. This search is illustrated in Figure 7.10. One of these events is displayed in Figure 7.11.

An event consistent with the decay $Z \rightarrow \mu^+\mu^-$ was also found by UA1 among the data collected in 1983. The mean of the mass distribution of all lepton pairs found by UA1 was:

$$m_Z = 95.2 \pm 2.5 \pm 3.0 \text{ GeV} \quad (7.62)$$

where the first error is statistical and the second one originates from the systematic uncertainty on the calorimeter energy scale.

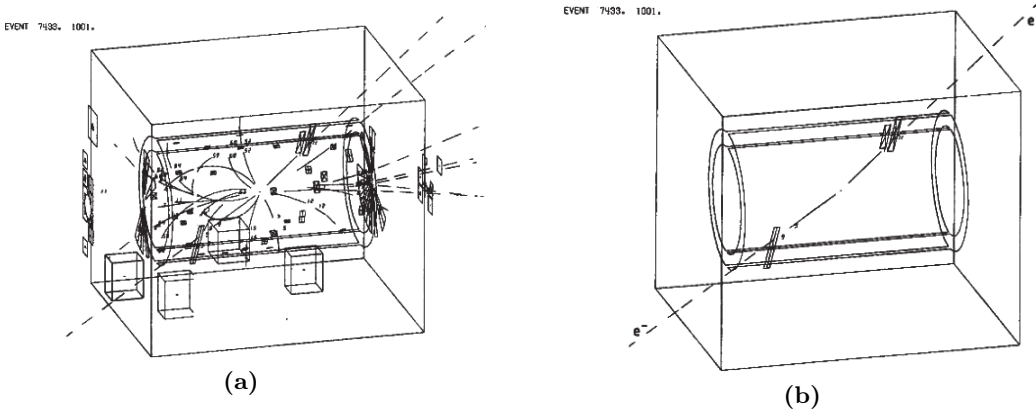


Figure 7.11: One of the $Z \rightarrow e^+e^-$ events in UA1: (a) display of all reconstructed tracks and calorimeter hit cells; (b) only tracks with $p_T > 2$ GeV/c and calorimeter cells with $E_T > 2$ GeV are showed.

Concerning the UA2 search for the decay $Z \rightarrow e^+e^-$ among the 1982-83 data, first, pairs of energy depositions in the calorimeter consistent with two isolated electrons and with $E_T > 25$ GeV were selected. Then, an isolated track consistent with an electron (from preshower information) was required to point to at least one of the clusters. Eight events satisfied these requirements: of these, three events had isolated tracks consistent with electrons pointing to both clusters. The weighted average of the invariant mass values for the eight events was:

$$m_Z = 91.9 \pm 1.3 \pm 1.4 \text{ GeV} \quad (7.63)$$

where the first error is statistical and the second one originates from the systematic uncertainty on the calorimeter energy scale. The latter is smaller than the corresponding UA1 value because the smaller size of the UA2 calorimeter, and its modularity, allow frequent recalibrations on electron beams of known energies from the CERN SPS.

Figure 7.12 shows the energy deposited in the UA2 calorimeter by a $W \rightarrow e\nu$ and by a $Z \rightarrow e^+e^-$ event. Such distributions, usually called ‘‘Lego plots’’, illustrate the remarkable topologies of such events, with large amounts of energy deposited in a very small number of calorimeter cells, and little or no energy in the remaining cells.

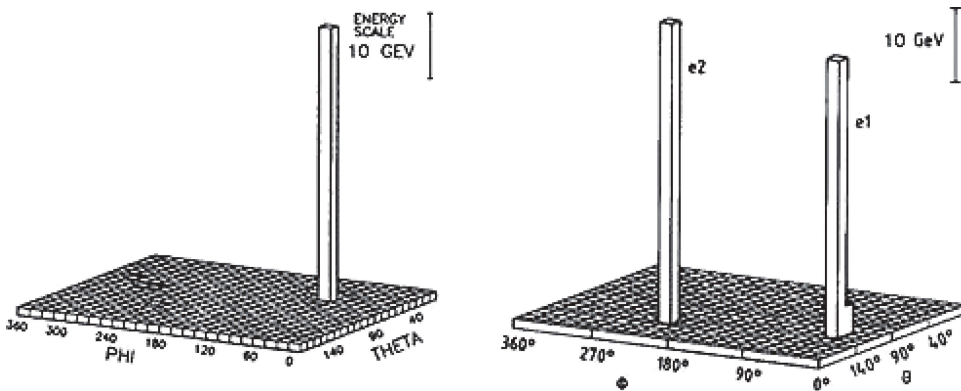


Figure 7.12: The energy deposited in the UA2 calorimeter for a $W \rightarrow e\nu$ (on the left) and a $Z \rightarrow e^+e^-$ event (on the right).

7.3.3 Measurements of W^\pm mass

After the discovery of the W and Z bosons at SPS in UA1 and UA2 experiments, Tevatron collider was built at Fermilab, where $p\bar{p}$ collisions at $\sqrt{s} = 1.8$ TeV were studied. The idea was to increase the energy in order to discover new particles and to produce a higher quantity of W and Z bosons. In particular, a sufficient quantity of W bosons was needed to measure its mass, which was an important point for EW theory. In fact, the mass m_W is connected to one of the coupling constants and to the Higgs field vacuum expectation.

In the experiment, the following decay process was studied:

$$W^\pm \rightarrow e^\pm \nu(\bar{\nu}) \quad (7.64)$$

It was not possible to detect directly neutrino, but since they appear as momentum missing, it was possible to know they were in the final state. For this reason, the invariant transverse mass was reconstructed rather than the more common invariant mass. For the W boson, the invariant mass reads:

$$M_W^2 = (p_e + p_\nu)^2 = 2p_e \cdot p_\nu = 2(E_e E_W - \vec{p}_e \cdot \vec{p}_\nu) \quad (7.65)$$

We assume that the mass of the neutrino and of the electron is approximately zero, so the energies E_e and E_ν are equal. For the invariant transverse mass, first of all we take the transverse plane to the axis, namely the z axis, to which the momenta of p and \bar{p} are parallel/antiparallel. Therefore, we get:

$$M_{W,T}^2 = 2(E_e E_\nu - \vec{p}_{T,e} \cdot \vec{p}_{T,\nu}) \quad (7.66)$$

So, going to the transverse plane removes the uncertainties on the energy along z . The results obtained from this analysis in the experiment are in Figure 7.13.

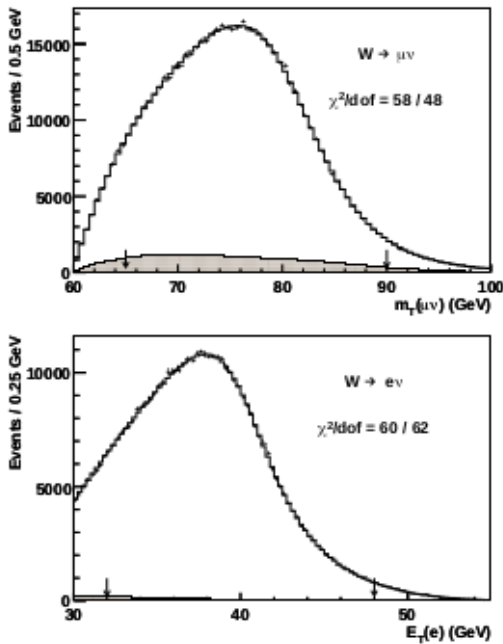


Figure 7.13: The M_T distribution for muons (top) and the $p_{e,T}$ distribution for electrons (bottom). The data (points) and the best-fit simulation template (histogram) including backgrounds (shaded) are showed. The arrows indicate the fitting range.

How can we translate the transverse invariant mass into the invariant mass? Using Monte Carlo simulations, we can generate samples of events (toy experiments) where

we assume the EW theory is correct and M_W is considered a parameter, since we don't know it exactly, but we have a range in which it is bounded. Then, we perform a global fit of the $M_{W,T}$, E_T or p_T using templates made by Monte Carlo data. Using this method, it is possible to extract the W invariant mass.

A list of several measurements of the W^\pm bosons mass is showed in Figure 7.14. There are several sources that contribute to the uncertainty. The most significant ones are provided by the parton distribution, by the lepton energy scale and resolution and by the recoil energy scale and resolution.

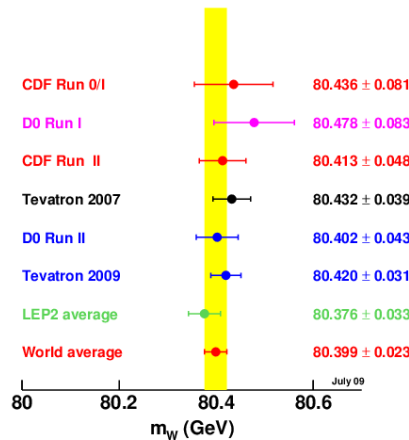


Figure 7.14: W mass measurements in several experiments and comparison.

7.3.4 Measurements of Z^0 mass

One of the most successful measurement of the Z^0 boson mass was performed at LEP (Large Electron-Positron) collider. It was built at CERN and its structure is showed in Figure 7.15.

Lecture 16.
Tuesday 5th May,
2020.
Compiled:
Wednesday 10th
June, 2020.

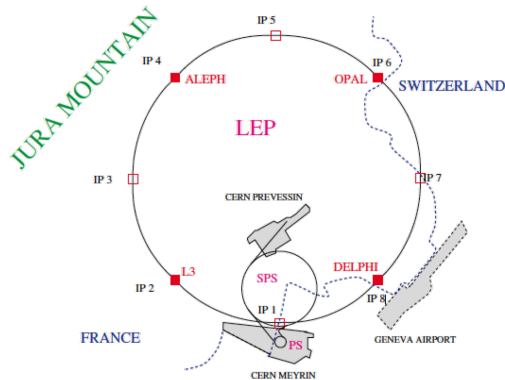


Figure 7.15: Map of LEP collider.

The tunnel is 27 kilometers long and it has four interaction points: ALEPH, OPAL, DELPHI and L3. When the LEP collider started operation in August 1989 it accelerated the electrons and positrons to a total energy of 45 GeV each to enable production of the Z boson, which has a mass of 91 GeV. The accelerator was upgraded later to enable production of a pair of W bosons, each having a mass of 80 GeV. LEP collider energy eventually topped at 209 GeV at the end in 2000. At a Lorentz factor of over 200,000 (given by the particle energy divided by rest mass, so 104.5 GeV/0.511 MeV),

LEP still holds the particle accelerator speed record, extremely close to the limiting speed of light. At the end of 2000, LEP was shut down and then dismantled in order to make room in the tunnel for the construction of the Large Hadron Collider (LHC). LEP was fed with electrons and positrons delivered by CERN's accelerator complex. The particles were generated and initially accelerated by the LEP Pre-Injector, and further accelerated to nearly the speed of light by the Proton Synchrotron and the Super Proton Synchrotron. From there, they were injected into the LEP ring. As in all ring colliders, the LEP's ring consisted of many magnets which forced the charged particles into a circular trajectory (so that they stay inside the ring), RF accelerators which accelerated the particles with radio frequency waves, and quadrupoles that focussed the particle beam (i.e. keep the particles together). The function of the accelerators was to increase the particles' energies so that heavy particles can be created when the particles collide. When the particles were accelerated to maximum energy (and focused to bunches), an electron and a positron bunch were made to collide with each other at one of the collision points of the detector. When an electron and a positron collide, they annihilate to a virtual particle, either a photon or a Z boson. The virtual particle almost immediately decays into other elementary particles (fermion and antifermion), which are then detected by the four huge particle detectors.

Let's see now one of the most important measurements done by LEP: the Z^0 line shape. The method employed consists in scanning the e^-e^- cross section in steps of energy. This can be achieved by preparing e^- and e^+ at a precise energy such that the energy in the center of mass \sqrt{s} is equal to the value of the step under study. By doing several experiments in which the energy is increased, we get the cross section dependence on \sqrt{s} . What can be observed in its plot is a resonance at around 91 GeV, modeled by a Breit-Wigner:

$$\sigma \sim \left| \frac{1}{s - m_Z^2 + im_Z\Gamma_Z} \right| \quad (7.67)$$

where Γ_Z is the width of the shape. The energy resolution of LEP ΔE_{LEP} is much smaller than Γ_Z , for this reason the Breit-Wigner shape is clearly visible in experimental data. The result is showed in Figure 7.16.

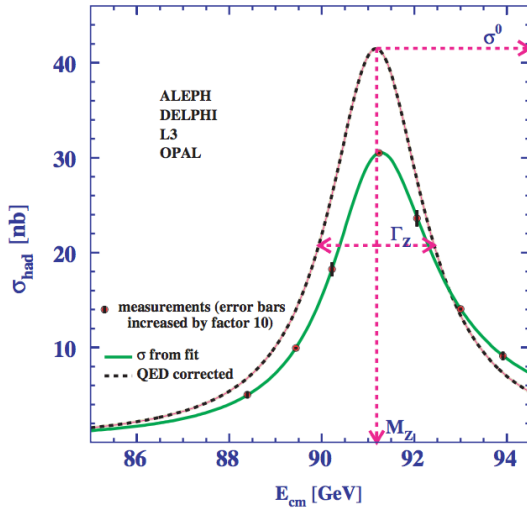


Figure 7.16: Cross section dependence on \sqrt{s} and resonance.

Before extracting from the fit the width Γ_Z , we have to be sure that the cross section prediction (i.e. the fit model) should take into account radiative corrections (photons attached to the external legs of e^- and e^+ in the Feynman diagrams). The Initial

State Radiation (ISR) causes a reduction in the height of the peak in the cross section for $\sqrt{s} \leq 91$ GeV. For $\sqrt{s} > 91$ GeV, ISR increases the height of the peak.

The experimental results of LEP and other experiments for Z^0 mass measurement are given in Figure 7.17. The most precise measurement up to now is:

$$M_Z = 91.1876 \pm 0.0021 \text{ GeV} \quad (7.68)$$

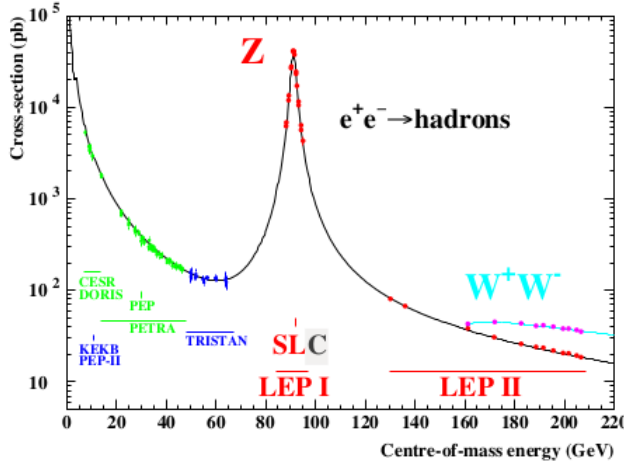


Figure 7.17: Experimental data on $e^+e^- \rightarrow \text{hadrons}$ cross section from several experiments.

The second thing that we can measure is the number of neutrino families. The width of the Z has several contributions:

$$\Gamma_Z = \Gamma_{ee} + \Gamma_{\mu\mu} + \Gamma_{\tau\tau} + \Gamma_{\text{had}} + \Gamma_{\text{inv}} = \Gamma_{\ell\ell} + \Gamma_{\text{had}} + \Gamma_{\text{inv}} \quad (7.69)$$

Concerning the first three pieces, we can write them in a unique $\Gamma_{\ell\ell}$ since it is experimentally proved by measuring the branching ratio that the contribution for every type of lepton is the same. Γ_{inv} can be written as the number of neutrino families multiplied by every $\Gamma_{\text{inv},i}$ if the only invisibles are the neutrinos. By fitting the cross section with the number of neutrino families as a free parameter, we get a result like the one in Figure 7.18.

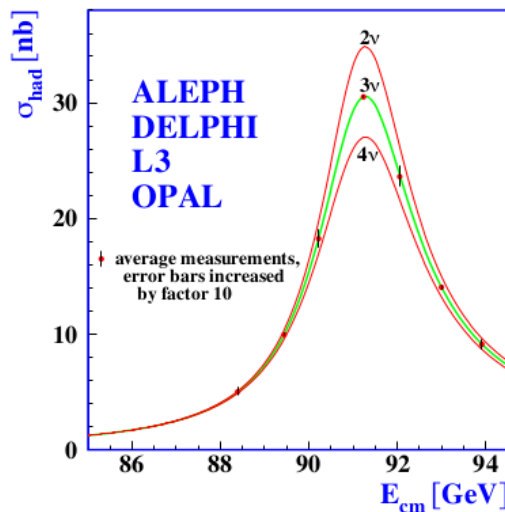


Figure 7.18: Shape of the Z boson cross section curve with respect to the number of neutrino families and fit with experimental data.

The result of this procedure is that the number of neutrino families is:

$$N_\nu = 2.9840 \pm 0.0082 \quad (7.70)$$

7.3.5 Measurement of A_{BF}

Another quantity that can be measured in e^+e^- annihilation process is the Forward-Backward Asymmetry. Its definition is:

$$A_{\text{FB}} = \frac{N_F - N_B}{N_F + N_B} \quad (7.71)$$

where N_F is the number of events with forward production of particles and N_B is the number of events with backward production. More precisely, the products of the e^+e^- collisions are emitted at an angle θ with respect to the beam axis. If $\cos \theta$ is greater than zero, this is a “forward event”, otherwise it is a “backward event”. What we can do is to measure N_F and N_B for different final states ($f\bar{f}$: $\mu^+\mu^-$, $\tau^+\tau^-$, $b\bar{b}$, $c\bar{c}$, ...) and for different center of mass energies. An example of the experimental results for $b\bar{b}$ and $c\bar{c}$ products is showed in Figure 7.19.

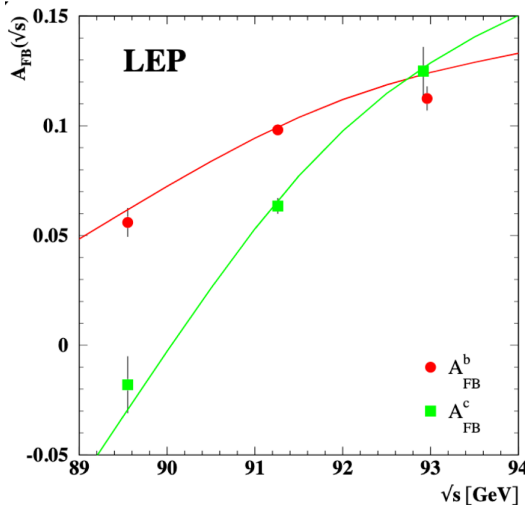


Figure 7.19: Forward-Backward Asymmetry for $b\bar{b}$ (in red) and $c\bar{c}$ (in green) depending on the center of mass energy \sqrt{s} .

Concerning the width, we have the following dependence:

$$\Gamma(Z^0 \rightarrow f\bar{f}) \approx \frac{g^2}{\cos^2 \theta_W} m_Z (I_3 - Q \sin^2 \theta_W) \quad (7.72)$$

So the asymmetry is due to a different way of producing the leptons or the hadrons in the final state, related to the isospin of the final state and to the cos and sin of the Weinberg angle.

Forward-Backward Asymmetry has been measured in several decay channels in order to obtain sufficient data to get the Weinberg angle. Among these, the decay into $b\bar{b}$ is particularly important for New Physics searches.

7.3.6 Determination of the Weinberg angle

The measurement of the Weinberg angle was performed by the collaboration of several experiments, in particular LEP and the Stanford Linear Accelerator Center (SLAC). The Stanford Linear Collider (SLC) was a linear accelerator that collided electrons and positrons at SLAC. The center of mass energy was about $\sqrt{s} = 90$ GeV, equal

to the mass of the Z boson, which the accelerator was designed to study. Although largely overshadowed by the Large Electron–Positron Collider at CERN, which began running in 1989, the highly polarized electron beam at SLC (close to 80%) made certain unique measurements possible, such as parity violation in Z Boson- b quark coupling. The structure of the facility is showed in Figure 7.20.

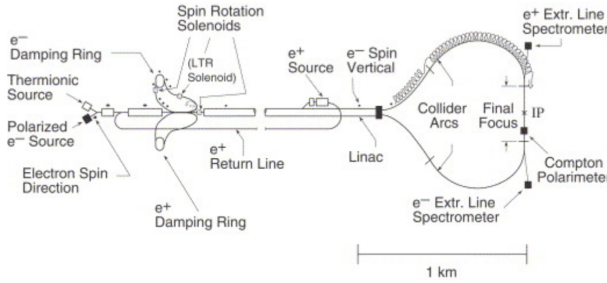


Figure 7.20: Structure of the SLC experiment.

At the SLC, the asymmetry A_e was measured as an asymmetry in the total rate of Z production from e^+e^- . In a circular accelerator, electron beam polarization is typically destroyed as the beams carry out many circuits of the ring. However, linear acceleration naturally preserves the electron polarization. The experiments at SLAC took advantage of this. Using polarized laser light, electrons were produced with preferential left- or right-handed polarization at the front of the accelerator, transported over 4 km to the collider interaction point, and then annihilated with positrons to create Z bosons. The correlation of the laser polarization with the rate for Z production allowed a measurement of the asymmetry in which almost all systematic errors cancelled. The experiment measured:

$$A_e = 0.1516 \pm 0.0021 \quad (7.73)$$

It is interesting that:

$$A_e \frac{\left(\frac{1}{2} - s_w^2\right)^2 - s_w^2}{\left(\frac{1}{2} - s_w^2\right)^2 + s_w^2} = \frac{\frac{1}{4} - s_w^2}{2s_w^4 + (\frac{1}{4} - s_w^2)} \approx 8\left(\frac{1}{4} - s_w^2\right) \quad (7.74)$$

where s_w is the sine of the Weinberg angle. Since the actual value of s_w^2 is close to $\frac{1}{4}$, this very accurate value of A_e turns into an even more accurate value of s_w^2 :

$$s_w^2 = 0.23109 \pm 0.00026 \quad (7.75)$$

For b quarks, the polarization asymmetry is expected to be almost maximal. This prediction could be tested at the SLC by using the polarized e^- beam to produce events with b quarks in the final state. Recall that the angular distributions in polarized e^+e^- annihilation depend on the fermion polarizations:

$$\frac{d\sigma}{d \cos \theta} \sim (1 + \cos \theta)^2 \quad (7.76)$$

$$\frac{d\sigma}{d \cos \theta} \sim (1 - \cos \theta)^2 \quad (7.77)$$

If the production of b_L dominates, the angular distribution should be highly forward peaked for an e_L^- beam and highly backward peaked for an e_R^- beam. The data from the experiment at the SLC are showed in Figure 7.21. Note that in the x axis it is reported the cosine of θ_{thrust} . This is due to the fact that the angle is calculated with respect to the thrust axis \hat{n} , defined through the following quantity:

$$T = \max \left(\frac{\sum_i |\vec{p}_i| \cdot \hat{n}}{\sum_i |\vec{p}_i|} \right) \quad (7.78)$$

Lecture 17.
Wednesday 6th
May, 2020.
Compiled:
Wednesday 10th
June, 2020.

The reason why we introduce this concept is due to the fact that experimentally in the final state we do not have a single particle to detect, but a shower since a jet is produced, and the thrust axis is the most reliable direction of the initial particle that generates the jet.

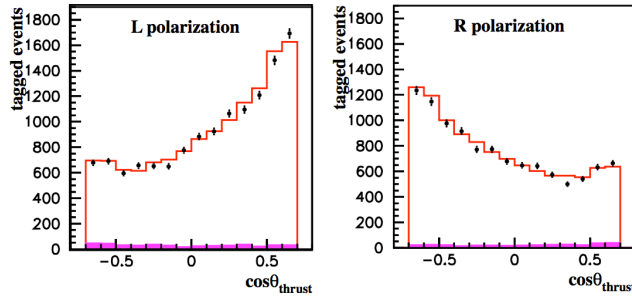


Figure 7.21: Results of SLC for $e_L^- e_R^+ \rightarrow b_L \bar{b}_R$ and $e_R^- e_L^+ \rightarrow b_L \bar{b}_R$.

The asymmetries are diminished because it is difficult to distinguish the b from the \bar{b} jet, but, nevertheless, the effect is striking. The observed distributions are consistent with the almost maximal asymmetry predicted by the $SU(2) \times U(1)$ theory. A summary on the results obtained for the Weinberg angle is given in Figure 7.22. What is clearly visible is that the measurement from SLD experiment at SLAC is very accurate, however is more than 2σ far from the average value taken from different experiments.

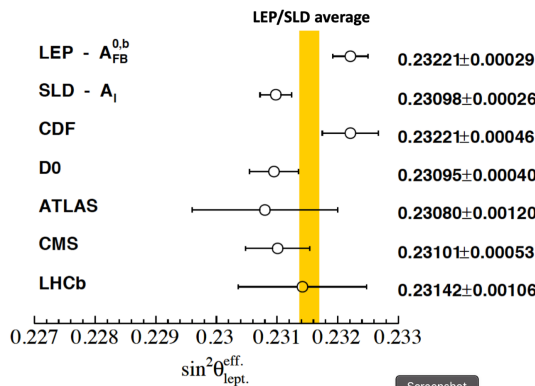


Figure 7.22: Summary on Weinberg angle measurements.

This variability in Weinberg angle is due to an (up to now) unknown behaviour. Indeed, the specific value of the angle is not a prediction of the Standard Model: it is an open, unfixed parameter. However, it is constrained and predicted through other measurements of Standard Model quantities. At this time, there is no generally accepted theory that explains why the measured value is what it is.

7.3.7 Global fit of SM measurements

The global fit to electroweak precision data routinely performed by the LEP electroweak working group and others, demonstrates impressively the predictive power of electroweak unification and quantum loop corrections. The fit is performed using the most recent experimental measurements and state-of-the-art SM predictions. Some examples of this powerful procedure are presented in Figure 7.23.

Lecture 18.

Tuesday 12th May,
2020.

Compiled:
Wednesday 10th
June, 2020.

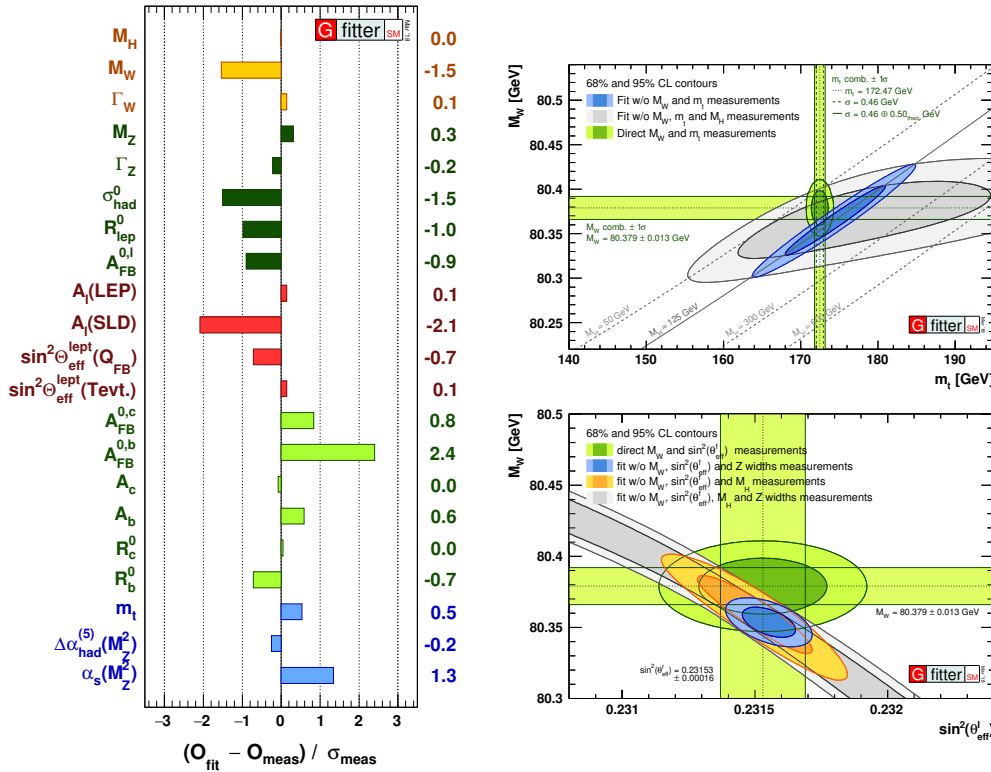


Figure 7.23: Several GFitter examples.

(Left) Comparing fit results with direct measurements: pull values for the SM fit, i.e. deviations between experimental measurements and theoretical calculations in units of the experimental uncertainty.

(Top-Right) Contours of 68% and 95% confidence level obtained from scans of fits with fixed variable pairs M_W vs. m_t . The narrower blue and larger grey allowed regions are the results of the fit including and excluding the M_H measurement, respectively. The horizontal bands indicate the 1σ regions of the M_W and m_t measurements.

(Bottom-Right) Contours of 68% and 95% confidence level obtained from scans of fits with fixed variable pairs M_W vs. $\sin^2 \theta_{\text{eff}}$. The narrower blue and larger grey allowed regions are the results of the fit including and excluding the M_H measurements, respectively. The horizontal bands indicate the 1σ regions of the M_W and $\sin^2 \theta_{\text{eff}}$ measurements (world averages).

7.4 Cabibbo Theory and CKM matrix

The theory of the weak interaction developed so far still omits some of the processes with which we began our discussion of this theory. We still have not proposed a mechanism for the strangeness changing decays such as:

$$K^0 \rightarrow \pi^- e^+ \nu \quad (7.79)$$

$$\Lambda^0 \rightarrow p e^- \bar{\nu} \quad (7.80)$$

These decays seem to call for a contribution to the weak charged current of the form:

$$u_L^\dagger \bar{\sigma}^\mu s_L \quad (7.81)$$

However, there is a strong constraint on this modification of the V-A theory. Although the charged-current weak interaction has sizable terms that change quark generation, the neutral-current weak interaction does not. Our theory of weak interactions must provide for flavor-changing charged-current decays while restricting flavor-changing neutral current decays.

7.4.1 The Cabibbo mixing angle

To begin, we must work out what interaction strength we need for the $s \rightarrow u$ weak decays. Writing the matrix elements for the weak interaction as a V-A interaction with the Fermi constant measured in muon decay, the weak interaction current will read:

$$j^{\mu+} = \nu^\dagger \bar{\sigma} \mu_L + \dots + V_{us} u_L^\dagger \bar{\sigma}^\mu s_L + \dots \quad (7.82)$$

That is, V_{us} gives the strength of the strangeness changing interaction relative to the strength of the weak interaction in muon decay.

It is possible to determine the value of V_{us} from the rates of Λ^0 , Σ^- , and K meson β decay. For example, by measuring the rate of $k \rightarrow \pi e \nu$ decays, the KLOE experiment at the INFN Frascati laboratory in Frascati determined:

$$V_{us} = 0.2249 \pm 0.0010 \quad (7.83)$$

This question is coupled to another one. To a first approximation, the strength of the V-A interaction in the β decay of nuclei is equal to that in muon decay. But, is this equality exact? Beginning in the late 1950's, attempts were made to measure the strength of the weak interaction in β decay precisely. To discuss this strength quantitatively, we might parametrize the $d \rightarrow u$ term in the V-A charged current as a term in Eq. 7.82 of the form:

$$j^{\mu+} = \dots + V_{ud} u_L^\dagger \bar{\sigma}^\mu d_L + \dots \quad (7.84)$$

In $SU(2) \times U(1)$ theory gauge invariance would require that the W boson couple to muon, electron and (u, d) doublets with the same strength. Then, we would have $V_{ud} = 1$. However, persistently, the values from experiment were somewhat smaller. The best experimental determinations come from the rates of superallowed β decay transitions between 0^+ nuclei. These use only the vector current. V_{ud} can be extracted as a normalization factor from the rates of the weak interaction decays. The best current value obtained from these measurements is:

$$V_{ud} = 0.97425 \pm 0.00022 \quad (7.85)$$

This value is significantly less than 1.

In 1963, working from the much more uncertain numbers then available, Cabibbo suggested that these two values fit together through the relation:

$$|V_{ud}|^2 + |V_{us}|^2 = 1 \quad (7.86)$$

That is, we can represent:

$$V_{ud} = \cos \theta_C \quad (7.87)$$

$$V_{us} = \sin \theta_C \quad (7.88)$$

where θ_C is called the **Cabibbo angle**. Evaluating the relation from the numbers above, we get:

$$|V_{ud}|^2 + |V_{us}|^2 = 0.9997 \pm 0.0005 \quad (7.89)$$

Apparently, the $SU(2)$ gauge interaction does couple with the same strength to quarks as to leptons, as is required by the structure of the gauge theory, but it couples the u quark to a linear combination of d and s .

7.4.2 Quark and lepton mass terms in the Standard Model

The structure just described can arise in a natural way in the $SU(2) \times U(1)$ model. To understand this, we must first explore how quark and lepton masses arise in that model. A mass term is a term in the Lagrangian:

$$\Delta\mathcal{L} = -m_f(f_R^\dagger f_L + f_L^\dagger f_R) \quad (7.90)$$

linking the two chiral components of a fermion field. However, we are forbidden to write such a term for any quark or lepton. The $SU(2) \times U(1)$ theory puts the left-handed quarks and leptons into $I = \frac{1}{2}$ doublets, but assigns the right-handed quarks and leptons $I = 0$. Thus, any mass term violates the $SU(2)$ gauge symmetry.

Thus, generation of mass for any quark or lepton requires the spontaneous breaking of $SU(2) \times U(1)$. The Higgs field φ has the quantum numbers $I = \frac{1}{2}$, $Y = \frac{1}{2}$. So, it is consistent with all symmetries of theory to add to the Lagrangian the terms:

$$\Delta\mathcal{L} = -y_e L_a^\dagger \varphi_a e_R - y_d Q_a^\dagger \varphi_a d_R - y_u Q_a^\dagger \varepsilon_{ab} \varphi_b^* u_R + \text{h.c.} \quad (7.91)$$

where $a, b = 1, 2$, and:

$$L = \begin{pmatrix} \nu \\ e^- \end{pmatrix}_L \quad Q = \begin{pmatrix} u \\ d \end{pmatrix}_L \quad (7.92)$$

The coefficients y_f are called **Yukawa couplings**. Each term is invariant under isospin, and each term has the sum of the hypercharges of the fields summing to zero. If we replace the Higgs field by its vacuum expectation value:

$$\varphi \longrightarrow \begin{pmatrix} 0 \\ \frac{v}{\sqrt{2}} \end{pmatrix} \quad (7.93)$$

we find that Eq. 7.91 becomes:

$$\Delta\mathcal{L} = -\frac{y_e v}{\sqrt{2}} e_L^\dagger e_R - \frac{y_d v}{\sqrt{2}} d_L^\dagger d_R - \frac{y_u v}{\sqrt{2}} u_L^\dagger u_R + \text{h.c.} \quad (7.94)$$

By comparison, we see that it has just the structure of mass terms for the e , d , and u . Then:

$$m_f = y_f \frac{v}{\sqrt{2}} \quad (7.95)$$

for all three species and this is what we want to measure. Note that in the previous Lagrangian mass terms do not appear the ones for the neutrinos. This is an excellent approximation for particle physics at GeV energies. However, the assumption that the neutrino masses are zero has important consequences and will be discussed in the following lectures.

The construction presented here gives an origin for the quark and lepton mass terms. But, it does not solve the problem of the large range of values of these terms. It only pushes the problem back one level, onto the physics of the fermion couplings to the Higgs field. This does not make the problem of quark and lepton masses any less mysterious.

7.4.3 Discrete space-time symmetries and the Standard Model

In nature, we see three fermions with each type of quantum number, for example, e , μ , and τ for charged leptons. We refer to the three states of each kind as belonging to three **generations**. To give mass to the second and third generations, we could

simply repeat the structure above. However, it is instructive to write a more general set of Yukawa couplings, in fact, the most general set of couplings consistent with $SU(2) \times U(1)$ gauge invariance.

Gauge invariance requires that the gauge couplings of the fermions of the three generations are absolutely identical. But, gauge invariance puts much weaker constraints on the Yukawa couplings. The most general Yukawa couplings consistent with gauge invariance include arbitrary mixtures of couplings among the three generations. Letting $i, j = 1, 2, 3$ label generations, this most general set of Yukawa couplings is written:

$$\Delta\mathcal{L} = -y_e^{ij} L_a^{\dagger i} \varphi_a e_R^j - y_d^{ij} Q_a^{\dagger i} \varphi_a d_R^j - y_u^{ij} Q_a^{\dagger i} \varepsilon_{ab} \varphi_b^* u j_R + \text{h.c.} \quad (7.96)$$

where the y_f^{ij} are complex-valued 3×3 matrices of general symmetry.

We can simplify this structure by diagonalizing the y_f matrices and making appropriate changes of variables among the fields. The Yukawa matrices are not Hermitian. But, they can be diagonalized by considering:

$$y_f y_f^\dagger \quad y_f^\dagger y_f \quad (7.97)$$

These are Hermitian and positive and have the same eigenvalues. We can represent them as:

$$y_f y_f^\dagger = U_L^{(f)} \mathbf{Y}_f U_L^{(f)\dagger} \quad (7.98)$$

$$y_f^\dagger y_f = U_R^{(f)} \mathbf{Y}_f U_R^{(f)\dagger} \quad (7.99)$$

where $U_L^{(f)}$ and $U_R^{(f)}$ are (in general, different) unitary matrices and \mathbf{Y}_f is real, positive and diagonal, identical in the two formulae. Then, if:

$$Y_f := \sqrt{\mathbf{Y}_f} \quad (7.100)$$

we have:

$$y_f = U_L^{(e)} Y_f U_R^{(f)\dagger} \quad (7.101)$$

For leptons, we now make the change of variables:

$$e_R^i \longrightarrow U_{R,ij}^{(e)} e_R^j \quad (7.102)$$

$$L^i \longrightarrow U_{L,ij}^{(e)} L^j \quad (7.103)$$

The matrices $U_L^{(e)}$ and $U_R^{(e)}$ disappear from the Yukawa couplings. The lepton mass terms are now diagonal in generation, and the new fields L^i , e_R^i correspond to mass eigenstates. These are now the fields of the familiar leptons e , μ and τ . This change of variables moves the matrices $U_L^{(e)}$ and $U_R^{(e)}$ to the lepton kinetic terms. But these matrices cancel out completely, because the three generations have the same gauge interactions. For example:

$$e_R^\dagger (i\sigma \cdot D) e_R \longrightarrow e_R^\dagger U_R^{(e)\dagger} (i\sigma \cdot D) U_R^{(e)} e_R = e_R^\dagger (i\sigma \cdot D) U_R^{(e)\dagger} U_R^{(e)} e_R = e_R^\dagger (i\sigma \cdot D) e_R \quad (7.104)$$

There are no interactions remaining that couple the lepton generations. Thus, lepton number conservation, separately for each generation, is a consequence, not an assumption, of the $SU(2) \times U(1)$ theory. However, we have not considered neutrino mass terms. If we had included a neutrino mass term, the matrices $U_L^{(e)}$ and $U_R^{(e)}$ would not

have cancelled out of that term and we would have very small generation-changing interactions proportional to the neutrino masses.

The construction for the quarks is somewhat more complicated. We make the change of variables:

$$u_R^i \rightarrow U_{R,ij}^{(u)} u_R^j \quad (7.105)$$

$$u_L^i \rightarrow U_{L,ij}^{(u)} u_L^j \quad (7.106)$$

$$d_R^i \rightarrow U_{R,ij}^{(d)} d_R^j \quad (7.107)$$

$$d_L^i \rightarrow U_{L,ij}^{(d)} d_L^j \quad (7.108)$$

After this change of variables, the matrices U_L , U_R have disappeared from the Yukawa couplings. The new u^i and d^i fields correspond to mass eigenstates, i.e. the physical quarks u , c , t and d , s , b . The unitary matrices are transferred to the quark kinetic terms. Then they cancel, just as for the leptons, at least, in the couplings to the gluon, photon, and Z boson. We now see that, for the most general structure of Yukawa couplings, the neutral current interaction mediated by the Z boson is always diagonal in flavor. In the coupling to the W boson, the unitary matrices do not completely cancel. Instead, we find:

$$u^\dagger(i\bar{\sigma}^\mu)d_L \rightarrow u_L^\dagger U_L^{(u)\dagger}(i\bar{\sigma}^\mu)U_L^{(d)}d_L = u_L^\dagger(i\bar{\sigma}^\mu)V_{CKM}d_L \quad (7.109)$$

where:

$$V_{CKM} = U_L^{(u)\dagger} U_L^{(d)} \quad (7.110)$$

The U_L matrices can thus be combined into a single unitary matrix, V_{CKM} , called **Cabibbo-Kobayashi-Maskawa matrix**. After the changes of variables, this is the only term in the weak interaction Lagrangian that contains generation-changing interactions. The matrix elements of V_{CKM} are exactly the parameters V_{ud} , V_{us} , etc., that were introduced before. So:

$$V_{CKM} = \begin{pmatrix} V_{ud} & V_{us} & V_{ub} \\ V_{cd} & V_{cs} & V_{cb} \\ V_{td} & V_{ts} & V_{tb} \end{pmatrix} \quad (7.111)$$

Thus, each physical u quark is linked by charged-current interactions to a different linear combination of the d quarks. V_{CKM} is a unitary matrix, and so these linear combinations are orthogonal. At this point, the combinations have complex coefficients. The imaginary parts of the coefficients can be shown to lead to CP and T violating interactions.

However, we can simplify the structure even further. A 3×3 unitary matrix has 9 parameters. If this matrix were real-valued, it would be a rotation matrix in 3 dimensions, parametrized by 3 Euler angles. So a 3×3 unitary matrix is parametrized by 3 angles and 6 phases. By a further change of variables to change the phases of the quark fields:

$$u_L^j \rightarrow e^{i\alpha_j} u_L^j \quad (7.112)$$

$$d_L^j \rightarrow e^{i\beta_j} d_L^j \quad (7.113)$$

we can remove 5 phases. The overall phase of the quark fields drops out of the Lagrangian and cannot be used to simplify V_{CKM} . So, finally, V_{CKM} can be written with 4 parameters: 3 angles and 1 phase. This phase is a single parameter that produces CP and T violation in the weak interaction.

A very convenient parametrization of the CKM matrix is that developed by Wolfenstein (1983). This parametrization uses the fact that V_{us} , V_{cb} , and V_{ub} are successively smaller. From these elements, the whole unitary matrix can be constructed using the requirement that, in a unitary matrix, the rows and the column are orthogonal vectors. The following formula maintains this orthogonality up to terms of order V_{us}^4 :

$$V_{\text{CKM}} = \begin{pmatrix} 1 - \frac{\lambda^2}{2} & \lambda & A\lambda^3(\rho - i\eta) \\ -\lambda & 1 - \frac{\lambda^2}{2} & A\lambda^2 \\ A\lambda^3(1 - \rho - i\eta) & -A\lambda^2 & 1 \end{pmatrix} + O(\lambda^4) \quad (7.114)$$

where:

$$\lambda = \frac{|V_{us}|}{\sqrt{|V_{ud}|^2 + |V_{us}|^2}} \quad (7.115)$$

$$A\lambda^2 = \lambda \frac{|V_{cb}|}{|V_{us}|} \quad (7.116)$$

$$A\lambda^3(\rho + i\eta) = V_{ub}^* \quad (7.117)$$

Lecture 19.

Wednesday 13th
May, 2020.
Compiled:
Wednesday 10th
June, 2020.

A useful way to visualize the phase of the CKM matrix is to plot the complex parameter $(\rho + i\eta)$ and use it to define a triangle, called the **unitarity triangle**, represented in Figure 7.24.

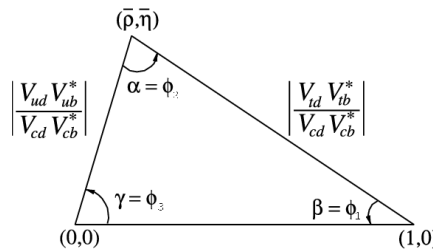


Figure 7.24: Unitarity triangle from CKM matrix.

The internal angles of the triangle are called (α, β, γ) or, alternatively, $(\varphi_2, \varphi_1, \varphi_3)$. The angle γ is the phase of $(\rho + i\eta)$. The angle β is defined in $A\lambda^3(1 - \rho - i\eta) = \mathcal{C}e^{-i\beta}$. There is CP violation as long as β and γ are nonzero and the triangle does not collapse to a line (degenerate triangle).

The following relations for CKM matrix elements hold:

$$\sum_{i,j} V_{ij} V_{ik}^* = \delta_{jk} \quad (7.118)$$

$$\sum_{i,j} V_{ij} V_{kj}^* = \delta_{ik} \quad (7.119)$$

The left and right sides of this triangle can be expressed more generally as:

$$(\rho + i\eta) = -\frac{V_{ud} V_{ub}^*}{V_{cd} V_{cb}^*} \quad (7.120)$$

$$(\rho + i\eta - 1) = \frac{V_{td} V_{tb}^*}{V_{cd} V_{cb}^*} \quad (7.121)$$

It should be noted that these ratios of V_{CKM} matrix elements are invariant to changes of phase of the quark fields. The closure of the triangle:

$$1 - (\rho + i\eta) - (1 - \rho - i\eta) = 0 \quad (7.122)$$

is equivalent to the relation:

$$V_{ud}V_{ub}^* + V_{cd}V_{cb}^* + V_{td}V_{tb}^* = 0 \quad (7.123)$$

which expresses the orthogonality of the first and third columns of the CKM matrix.

7.4.4 Experimental determination of V_{ud} , V_{cs} , V_{us} and V_{cd}

These terms describe the transitions between the quarks of the two lightest families and form the original 2×2 Cabibbo matrix. In the complete 3×3 CKM matrix, a CP violating phase appears, which can contribute also to these terms. Experimentally, it is however observed that CP violation is very small in these CKM matrix elements compared to the CP -conserving part. Leptonic and semileptonic transitions between hadrons containing u , d , s and/or c quarks are exploited to measure these elements. The amplitudes for the corresponding branching ratios are generally expressed as the product of a CKM matrix element with a hadronic parameter describing the hadronisation of the initial and final quarks into hadrons (decay constants and form factors for leptonic and semi-leptonic decays, respectively). The latter are generally obtained from lattice QCD simulations. Additional electromagnetic corrections are added, when known (mostly for leptonic decays of light mesons).

V_{ud} measurement

The most precise measurements of V_{ud} are obtained from the decay rates of nuclei experiencing superallowed β decays. In these favoured nuclear transitions, the wave function of the entire nucleus is left unchanged since these decays involve no change in angular momentum nor parity. These processes provide thus clean theoretical predictions, can be evaluated by precise calculations that do not require strong assumptions or approximations, allowing for a very precise determination of V_{ud} . To date, the half-lives of 14 superallowed β decays have been measured and the average value of V_{ud} is found to be:

$$|V_{ud}| = 0.97420 \pm 0.00021 \quad (7.124)$$

where the error is dominated by theoretical uncertainties from nuclear Coulomb distortions and radiative corrections.

This CKM matrix element is also accessible from the measurement of the neutron lifetime, although this determination is limited by the knowledge of the ratio of the axial vector and vector (both states with spin 1 but even and odd parity, respectively) couplings and exhibits inconsistent values from different experiments. The analogous transition to β decays in the pion sector, known as the pion β decay ($\pi^+ \rightarrow \pi^0 e^+ \nu_e$, is free of nuclear-structure corrections and provides a stringent test of weak decays. The PIBETA experiment used this transition to extract a measurement of V_{ud} with a precision of 0.3%.

V_{us} measurement

Semileptonic and leptonic kaon decays are used to measure V_{us} , including charged and neutral $K \rightarrow \pi \ell \nu_\ell$ decays and the leptonic $K^+ \rightarrow \mu^+ \nu_\mu$ decay, with the main limitation arising from the knowledge on the form factors and decay constant, respectively. Including the latest results from the KLOE experiment, the average from these measurements provides:

$$|V_{us}| = 0.2243 \pm 0.0005 \quad (7.125)$$

This element can be also extracted from hyperon decays and hadronic τ decays like $\tau^- \rightarrow K^- \nu_\tau$ measured at LEP as well as by the Belle and BaBar collaborations, but with a larger uncertainty. In all the cases theoretical input on the relevant hadronic quantities (decay constants or form factors) is needed and generally taken from lattice QCD simulations to extract V_{us} .

V_{cd} measurement

Analogously, the determination of V_{cd} , is currently based on leptonic and semileptonic charm decays, namely $D \rightarrow \pi e^- \bar{\nu}_e$ and $D^+ \rightarrow \mu^+ \nu_\mu$, explored by the CLEO-c, Belle, BaBar and BESIII collaborations, and the relevant lattice QCD form factors. Earlier measurements were obtained from neutrino scattering data, from the difference in the ratio of double-muon production ($\nu_\mu + N \rightarrow \mu + c \rightarrow \mu^+ \mu^- + X$), which proceeds through charm production, and single-muon production ($\nu_\mu + N \rightarrow \mu + X$) in neutrino and anti-neutrino beams, at the CDSHS, CCFR and CHARM II experiments. The current world average gives:

$$|V_{cd}| = 0.218 \pm 0.004 \quad (7.126)$$

dominated by the measurements from semileptonic decays, whose precision is limited by the theoretical uncertainty of the form factors.

V_{cs} measurement

Also V_{cs} can be obtained from semileptonic D decays like $D \rightarrow K \ell \nu_\ell$ and leptonic D_s^+ decays like $D_s^+ \rightarrow \mu^+ \nu_\mu$ or $D_s^+ \rightarrow \tau^+ \nu_\tau$ and lattice QCD form factors or decay constants. The Belle, CLEO-c, BaBar and BESIII experiments have measured these decays with precision, leading to the average:

$$|V_{cs}| = 0.997 \pm 0.017 \quad (7.127)$$

where the uncertainty is dominated by the experimental precision for leptonic decays and by the theoretical knowledge of the form factors for semileptonic decays. The tagged measurement of $W^+ \rightarrow c \bar{s}$ from the DELPHI experiment gives also a direct determination of V_{cs} , far less precise than leptonic and semileptonic decays of charm hadrons.

7.4.5 Experimental determination of V_{ub} , V_{cb} and V_{tb}

Similarly to the matrix elements of the first two generations, the moduli of V_{cb} and V_{ub} can be accessed through the semileptonic $b \rightarrow (u, c)\ell \nu_\ell$ decays ($\ell = e, \mu$). A long-standing discrepancy exists between the determinations obtained from exclusive decays and from inclusive modes, which are treated with different approaches.

V_{cb} measurement

In the case of V_{cb} , one can first use the inclusive decay $B \rightarrow X_c \ell \nu_\ell$ (X_c denoting all final states with a charm quark). Using the tool of Operator Product Expansion (OPE), one can express the decay rate as the product of $|V_{cb}|$ by a series in $1/m_b$ and $1/m_c$, with coefficients that can be determined experimentally. This is obtained by considering moments of the differential branching ratio of $B \rightarrow X_c \ell \nu_\ell$ with respect to the leptonic or the hadronic invariant mass. These coefficients can be determined together with $|V_{cb}|$ through a global fit to experimental measurements, yielding the so-called inclusive value of $|V_{cb}|$.

One can also consider exclusive decays. There are determinations of the $B \rightarrow D\ell\nu$ form factors based on lattice QCD that provide the normalisation at momentum transfer $q^2 = 0$ (where the momentum transfer $q = p_B - p_D$ is the difference of the B and D 4-momenta). This normalisation is needed to analyse the experimental measurements which yield the product of the vector form factor at $q^2 = 0$ by $|V_{cb}|$. The situation is less satisfying for $B \rightarrow D^*\ell\nu_\ell$. On the experimental side, one of the main issues comes from the existence of a background $B \rightarrow D^{**}\ell\nu_\ell$ of wide charm resonances which is not very well understood currently. On the theoretical side, due to the lack of a complete lattice QCD determination of the form factors involved, heavy-quark effective theory (HQET) is used to simplify the expression of the form factors and to constrain their dependence on the lepton energy. The HQET approach starts from the limit where both the b and the c quarks are considered as very heavy and expands the form factors in powers of $1/m_b$ and $1/m_c$. The resulting parametrisation (called CLN parametrisation) of the form factors depends only on a few coefficients that can be estimated using dedicated theoretical methods (e.g. sum rules). The values of $|V_{cb}|$ extracted from data from B factories using the CLN parametrisation tend to disagree with the inclusive determination described above. The accuracy of the CLN parametrisation has been questioned recently: it is possible to resort to a more general parametrisation of the form factors (called BGL parametrisation) and fit this expression to the decay rate obtained from B -factories. However, the fits of Babar and Belle data on exclusive decays to CLN and BGL parametrisations turn out to provide similar values for $|V_{cb}|$. The agreement between the various extractions remain thus still under debate, with the current world averages:

$$|V_{cb}| = (42.2 \pm 0.8) \cdot 10^{-3} \text{ (inclusive)} \quad (7.128)$$

$$|V_{cb}| = (41.9 \pm 2.0) \cdot 10^{-3} \text{ (exclusive)} \quad (7.129)$$

V_{ub} measurement

In the case of V_{ub} , one can also use either exclusive or inclusive measurements to extract the CKM matrix element. The exclusive determination benefits from lattice QCD computations for the vector form factor of the decay $B \rightarrow \pi\ell\nu$, which can be combined with measurements of the differential decay rate.

The inclusive determination is more challenging. The full decay rate cannot be accessed, because a cut in the lepton energy must be performed to eliminate the huge $b \rightarrow c\ell\nu_\ell$ background. The OPE expansion in $1/m_b$ must be modified, introducing poorly known shape functions describing the b quark dynamics in the B meson. They can be constrained partly from $B \rightarrow X_s\gamma$, with some questions concerning the convergence rate of the series in $1/m_b$. The current world averages are:

$$|V_{ub}| = (4.49 \pm 0.15^{+0.16}_{-0.17} \pm 0.17) \cdot 10^{-3} \text{ (inclusive)} \quad (7.130)$$

$$|V_{ub}| = (3.70 \pm 0.10 \pm 0.12) \cdot 10^{-3} \text{ (exclusive)} \quad (7.131)$$

The element $|V_{ub}|$ can also be determined from the leptonic decay $B \rightarrow \tau^-\nu_\tau$ which has been studied at factories, favouring values in agreement with the average of inclusive and exclusive determinations. The measurement of this leptonic decay is rather challenging, as it requires a very good understanding of τ decays for their reconstruction and the elimination of a large set of significant backgrounds.

These determinations, which are essentially dominated by systematic uncertainties related to hadronic inputs, have thus led to a long-standing discrepancy between inclusive and exclusive determinations for $|V_{ub}|$ and $|V_{cb}|$. Currently, global fits use averages of both kinds of determination as inputs, and their outcome favours exclusive measurements for $|V_{ub}|$ and inclusive measurements for $|V_{cb}|$.

V_{tb} measurement

Finally, the CKM element V_{tb} can be obtained from the cross section for single top quark production. The combination of Tevatron and LHC data yields:

$$|V_{tb}| = 1.029 \pm 0.025 \quad (7.132)$$

which is not competitive with the very accurate determination of this element within the SM based on the rest of the constraints on the CKM parameters combined with the unitarity of the CKM matrix. Less stringent constraints on $|V_{tb}|$ can be obtained from the ratio of branching ratios:

$$\frac{\text{Br}(t \rightarrow Wb)}{\text{Br}(t \rightarrow Wq)} \quad (7.133)$$

and from LEP electroweak precision measurements.

7.4.6 Experimental determination of V_{td} and V_{ts}

In the Standard Model, neutral mesons with a given flavour content can mix with their antiparticles through $\Delta F = 2$ box diagrams, where F is the flavour of the heavier quark, with two W bosons being exchanged, involving therefore products of the CKM matrix (see Figure 7.25 for an example in the case of B^0 and \bar{B}_q^0). It turns out that the mixing of charmed meson D^0 ($c\bar{u}$) into its antiparticle cannot be exploited to set constraints on the CKM matrix due to large and poorly known effects from the strong interaction at low energy for example, but other neutral mesons can provide interesting constraints.

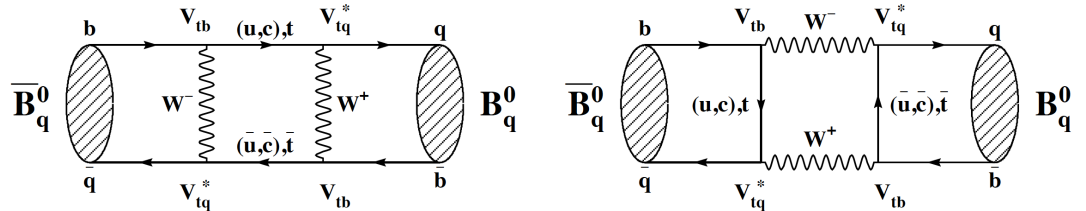


Figure 7.25: Box diagrams describing B_q - \bar{B}_q mixing, where q can be a d or an s quark.

Concerning the neutral kaon system, indirect CP violation was observed in the decay of particles to a pair of pions. The $\pi\pi$ final state system has a $CP = +1$, therefore it was shown that this transition is possible because the meson (which decays to the $CP = -1$ final state $\pi\pi\pi$ in the majority of the cases) contains also a $CP = +1$ component. The complex observable ε_K defined as the ratio of decay amplitudes:

$$\varepsilon_K = \frac{\Gamma(K_L \rightarrow \pi\pi)_{I=0}}{\Gamma(K_S \rightarrow \pi\pi)_{I=0}} \quad (7.134)$$

where the final states have a null value of isospin, encodes the neutral kaon mixing. It is possible to relate ε_K with the parameters from the formalism which describes the K^0 - \bar{K}^0 oscillations where K^0 is $(\bar{s}d)$ and \bar{K}^0 is $(\bar{d}s)$.

Experimentally, the kaon mixing observables were measured in dedicated fixed-target experiments such as NA48 at CERN and KTeV at Fermilab. The current experimental values which are derived from the measurements of the decay amplitudes for $K \rightarrow \pi^+\pi^-$ and $K \rightarrow \pi^0\pi^0$ are the modulus and phase of ε_K :

$$|\varepsilon_K| = 2.228(11) \cdot 10^{-3} \quad (7.135)$$

$$\varphi_{\varepsilon_K} = 42.52(5) \quad (7.136)$$

leading to a combined constraint on $V_{td}V_{ts}^*$ and $V_{cd}V_{cs}^*$.

We turn now to the mixing of neutral b -mesons. Because top quarks decay very quickly into jets that cannot be tagged easily according to their content in light quarks, the only way of measuring is through the measurement of the mixing of B^0 - \bar{B}^0 and B_s^0 - \bar{B}_s^0 mesons (as these processes are dominated by top-quark boxes in the SM as shown in Figure 7.25). For each of these mesons, the two mass eigenstates resulting from mixing have different masses, and their difference of masses Δm_d and Δm_s (related to and respectively) can be accessed by looking at the time evolution of mesons, using their decays in order to determine the frequency with which they evolve into their antiparticles. The current world averages for them are:

$$\Delta m_d = (0.5064 \pm 0.0019) \text{ ps}^{-1} \quad (7.137)$$

$$\Delta m_s = (17.757 \pm 0.021) \text{ ps}^{-1} \quad (7.138)$$

It is interesting to notice that even though the mesons differ only in the flavour of their spectator quark, because of the different factors from the CKM matrix, the frequency of the mixing is significantly higher than the one. Once the frequencies are measured and using lattice QCD input for the so called bag factors describing the hadronisation of the quark-level box diagrams into the oscillation between B -mesons, the CKM parameters can be extracted:

$$|V_{td}| = (8.1 \pm 0.5) \cdot 10^{-3} \quad (7.139)$$

$$|V_{ts}| = (39.4 \pm 2.3) \cdot 10^{-3} \quad (7.140)$$

The current accuracy of these values is limited by theoretical uncertainties on hadronic effects (encoded in bag parameters), which cancel largely in the following ratio thanks to $SU(3)$ flavour symmetry.

7.5 CP violation

In this section, we will discuss the evidence for CP violation in hadronic weak decays. We will see that CP violation, though it has a very small effect, is clearly observed in specific weak interaction processes. These observations are well explained by the CKM phase in the mixing matrix for charge-changing weak interactions.

CP violation is difficult to observe directly if we use the standard observables discussed so far. Typically, it leads to only very small asymmetries in the rates of weak interaction decays between particles and antiparticles. The most compelling evidence for CP violation comes from a different kind of experiment in which we observe the time-dependent evolution of a particle that decays through the weak interaction. In such a system, CP violation can be observed as a nonzero phase in the quantum interference of two components of the wavefunction of the decaying state. In some cases, this quantum interference plays out over macroscopic distances, of the order of meters.

7.5.1 CP violation in the K^0 - \bar{K}^0 system

There is a very small amplitude that mixes the K^0 and \bar{K}^0 states. This observation leads to some unexpected phenomena in K^0 decays even in the case where CP is conserved.

The neutral K meson is a 2-state quantum system that evolves according to:

$$e^{-i\mathbf{M}\tau} \quad (7.141)$$

Lecture 20.
Tuesday 19th May, 2020.
Compiled:
Wednesday 10th June, 2020.

where τ is the time measured in the rest frame (proper time) and \mathbf{M} is a mass matrix for the two-state system. If CP is conserved, \mathbf{M} has the form:

$$\mathbf{M} = \begin{pmatrix} \bar{m} - i\frac{\bar{\Gamma}}{2} & \delta m - i\frac{\delta\Gamma}{2} \\ \delta m - i\frac{\delta\Gamma}{2} & \bar{m} - i\frac{\bar{\Gamma}}{2} \end{pmatrix} \quad (7.142)$$

symmetrical between particles and antiparticles. The parameters \bar{m} and δm contribute to the masses of the eigenstate particles. The parameters $\bar{\Gamma}$ and $\delta\Gamma$ contribute to their decay rates. The factor $(-i)$ turns the system evolution into an exponential decay. CPT theorem requires that the diagonal elements of this matrix are equal. So, C and P act on $|K^0\rangle$ and $|\bar{K}^0\rangle$ as:

$$P|K^0\rangle = -|K^0\rangle \quad (7.143)$$

$$P|\bar{K}^0\rangle = -|\bar{K}^0\rangle \quad (7.144)$$

$$C|K^0\rangle = +|\bar{K}^0\rangle \quad (7.145)$$

$$C|\bar{K}^0\rangle = +|K^0\rangle \quad (7.146)$$

Thus, CP symmetry implies that the off-diagonal elements of the matrix \mathbf{M} are equal. The eigenstates of this mass matrix are CP eigenstates:

$$|K_S^0\rangle = \frac{1}{\sqrt{2}}(|K^0\rangle - |\bar{K}^0\rangle) \quad CP = +1 \quad (7.147)$$

$$|K_L^0\rangle = \frac{1}{\sqrt{2}}(|K^0\rangle + |\bar{K}^0\rangle) \quad CP = -1 \quad (7.148)$$

The corresponding mass and decay rate eigenvalues are:

$$M_S = \bar{m} - \delta m - i\frac{\bar{\Gamma} - \delta\Gamma}{2} \quad (7.149)$$

$$M_L = \bar{m} + \delta m - i\frac{\bar{\Gamma} + \delta\Gamma}{2} \quad (7.150)$$

A particle produced as a K^0 will propagate as a linear combination of K_S^0 and K_L^0 . The two components of the wavefunction will have different decay rates and will oscillate with different frequencies.

The K^0 and \bar{K}^0 are stable with respect to the strong interactions, but can decay by the weak interaction. There are several possibilities:

$$s \rightarrow ue^-\bar{\nu}_e \quad (7.151)$$

$$s \rightarrow u\mu^-\bar{\nu}_\mu \quad (7.152)$$

$$s \rightarrow ud\bar{u} \quad (7.153)$$

QCD corrections gives a large enhancement for the purely hadronic decay modes. In particular:

$$K^0, \bar{K}^0 \rightarrow \pi\pi \quad (7.154)$$

is enhanced by about a factor of 100 relative to other modes. The decay:

$$K^0, \bar{K}^0 \rightarrow \pi\pi\pi \quad (7.155)$$

also has QCD enhancement, but at the same time it is suppressed by the large denominator in the formula for 3-body phase space and by the fact that $(m_K - 3m_\pi)$ is small. For pions in an S-wave, the dominant final states are:

$$CP|\pi\pi\rangle = +|\pi\pi\rangle \quad (7.156)$$

$$CP|\pi\pi\pi\rangle = -|\pi\pi\pi\rangle \quad (7.157)$$

Then, the state K_S^0 is allowed to decay to $\pi\pi$, but the state K_L^0 can not decay in the same way since CP conservation forbids it. This has the outcome that the two mass eigenstates of the K^0 - \bar{K}^0 system gave two very different lifetimes:

$$\tau_S = 0.895 \cdot 10^{-10} \text{ s} \quad \Rightarrow \quad c\tau_S = 2.68 \text{ cm} \quad (7.158)$$

$$\tau_L = 5.116 \cdot 10^{-8} \text{ s} \quad \Rightarrow \quad c\tau_L = 15.34 \text{ m} \quad (7.159)$$

The two states are appropriately called “ K -short” and “ K -long”. It is an interesting accident that the K_L^0 - K_S^0 mass difference:

$$m_L - m_S = 3.48 \cdot 10^{-15} \text{ GeV} \implies \frac{\hbar}{2(m_L - m_S)} = 0.95 \cdot 10^{-10} \text{ s} \quad (7.160)$$

corresponds to a time very close to the lifetime if the K_S^0 .

So far, we have analyzed the K^0 - \bar{K}^0 system under the assumption that CP is conserved. However, in 1964, the picture was made more complicated. In an experiment at the Brookhaven National Laboratory, Christenson, Cronin, Fitch, and Turlay (1964) carefully observed K_L^0 decays in a meters-long decay region filled with helium. They discovered that there is a small component of decays to $\pi^+\pi^-$ with the time dependence of the K_L^0 lifetime. This decay:

$$|K_L^0\rangle \longrightarrow |\pi\pi\rangle \quad (7.161)$$

cannot proceed unless CP is violated. The branching ratio is:

$$\text{BR}(K_L^0 \rightarrow \pi\pi) = 2.8 \cdot 10^{-3} \quad (7.162)$$

so the effect is doubly small, a small effect in comparison to the already small K_L^0 decay rate.

There is a place for this CP violating effect within the Standard Model. The t quark can appear as an intermediate state in the K^0 - \bar{K}^0 mixing amplitude, and diagrams with the t quark can carry a phase, like in the diagram in Figure ??.

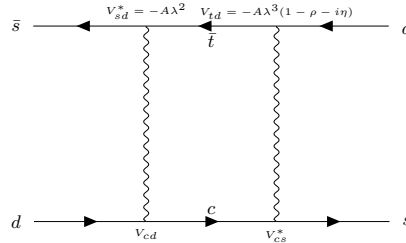


Figure 7.26: Box diagram of K^0 - \bar{K}^0 mixing, with a t quark as intermediate state.

The effect on the K^0 - \bar{K}^0 mass matrix is to change \mathbf{M} in the following way:

$$\mathbf{M} = \begin{pmatrix} \bar{m} - i\frac{\Gamma}{2} & \delta m(1 + i\zeta) - i\frac{\delta\Gamma}{2} \\ \delta m(1 - i\zeta) - i\frac{\delta\Gamma}{2} & \bar{m} - i\frac{\Gamma}{2} \end{pmatrix} \quad (7.163)$$

The eigenstates of this matrix are (to first order in ζ):

$$|K_S^0\rangle = \frac{1}{\sqrt{2}}[(1 + \varepsilon)|K^0\rangle - (1 - \varepsilon)|\bar{K}^0\rangle] \quad (7.164)$$

$$|K_L^0\rangle = \frac{1}{\sqrt{2}}[(1 + \varepsilon)|K^0\rangle + (1 - \varepsilon)|\bar{K}^0\rangle] \quad (7.165)$$

where:

$$\varepsilon = \frac{i\zeta}{\delta m - i\frac{\delta\Gamma}{2}} \quad (7.166)$$

The states $|K_S^0\rangle$ and $|K_L^0\rangle$ are not orthogonal, but this is permitted because the modified mass matrix is not Hermitian.

The parameter δm is half of the $K_L^0 - K_S^0$ mass difference. The K_S^0 and K_L^0 decay rates are:

$$\Gamma_S = \bar{\Gamma} - \delta\Gamma \quad (7.167)$$

$$\Gamma_L = \bar{\Gamma} + \delta\Gamma \quad (7.168)$$

which implies:

$$\delta\Gamma \approx -\frac{1}{2}\Gamma_S \quad (7.169)$$

Using these relations, we find:

$$\varepsilon = \frac{2i\zeta}{m_L - m_S + i\frac{\Gamma_S}{2}} \quad (7.170)$$

The real and imaginary parts of the denominator are almost equal. This predicts the phase of ε :

$$\varepsilon = |\varepsilon| e^{i\varphi} \quad \text{with} \quad \varphi = 44^\circ \quad (7.171)$$

To describe the effects of this change in the mass matrix, it is useful to write the eigenstates of \mathbf{M} in terms of the CP eigenstates, denoted by $|K_+\rangle$ and $|K_-\rangle$. We find:

$$|K_S^0\rangle = |K_+\rangle + \varepsilon |K_-\rangle \quad (7.172)$$

$$|K_L^0\rangle = |K_-\rangle + \varepsilon |K_+\rangle \quad (7.173)$$

It follows from this formula that:

$$\frac{\Gamma(K_L^0 \rightarrow \pi\pi)}{\Gamma(K_S^0 \rightarrow \pi\pi)} = |\varepsilon|^2 \quad (7.174)$$

Evaluating this formula, we find:

$$|\varepsilon| = 2.23 \cdot 10^{-3} \quad (7.175)$$

Each of the states K_S^0 , K_L^0 evolves, in its rest frame, according to:

$$e^{-im\tau} e^{-\Gamma \frac{\tau}{2}} \quad (7.176)$$

where τ is proper time. For a moving K^0 state, the oscillation plays out as function of position along its path. A coherent state of K_S^0 and K_L^0 then displays an interference pattern. Since both states can decay to $\pi^+\pi^-$, we can see this interference in the decay rate to $\pi^+\pi^-$. For a K meson state behind a regenerator, with the wavefunction:

$$a |K^0\rangle + b |\bar{K}^0\rangle = \alpha |K_L^0\rangle + \beta |K_S^0\rangle \quad (7.177)$$

the decay rate is proportional to:

$$\begin{aligned} \Gamma(K^0 \rightarrow \pi\pi) &\sim \left| \varepsilon \alpha e^{-im_L\tau - \Gamma_L \frac{\tau}{2}} + \beta e^{-im_S\tau - \Gamma_S \frac{\tau}{2}} \right|^2 \\ &\sim |\beta|^2 \left| e^{-\Gamma_S \frac{\tau}{2}} + \frac{\varepsilon \alpha}{\beta} e^{-i(m_L - m_S)\tau - \Gamma_L \frac{\tau}{2}} \right|^2 \end{aligned} \quad (7.178)$$

This function has the form of an oscillation superposed on an exponential decay. This is quantum interference over a macroscopic length scale. Some examples of such interference patterns seen in real experiments are showed in Figure 7.27

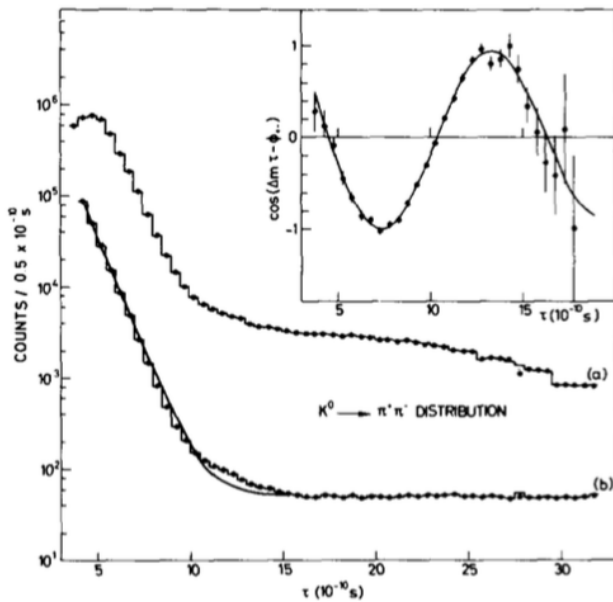


Figure 7.27: Distribution of $K^0 \rightarrow \pi^+\pi^-$ decays behind a regenerator as a function of proper time.

7.5.2 CP violation in B -meson system

In the Standard Model, CP violation is expected to come from an order-1 phase associated with heavy quarks. If this is true, there must be a heavy quark weak interaction process with order-1 CP violation. Bigi, Carter, and Sanda suggested that one could see order-1 effects of the CKM phase in the time-dependence of decays of B mesons to exclusive final states with definite CP . The simplest example is:

$$B^0, \bar{B}^0 \rightarrow J/\psi K_S^0 \quad (7.179)$$

If we consider the decay of $\bar{B}^0(b\bar{d})$, the \bar{B}^0 can reach the $J/\psi K_S^0$ final state in two ways. First, it can decay directly, through the weak interaction process $b \rightarrow c\bar{c}s$, as represented in Figure 7.28.

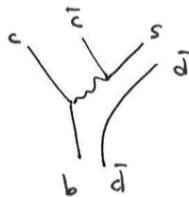


Figure 7.28: Weak interaction process $b \rightarrow c\bar{c}s$. The diagram represents a term proportional to $V_{cb}V_{cs}^*$.

But also, it can decay through $B^0-\bar{B}^0$ mixing, followed by the process $\bar{b} \rightarrow \bar{c}c\bar{s}$. The $K^0-\bar{K}^0$ mixing matrix must also be used to cause the final states to interfere. This is represented in Figure 7.29

The $B^0-\bar{B}^0$ mixing amplitude is dominated by the process in Figure 7.30.

The $K^0-\bar{K}^0$ mixing amplitude is dominated by the process in Figure 7.31.

The two paths differ by a relative factor proportional to:

$$-[V_{cb}^*V_{cs}V_{tb}V_{td}^*V_{cs}^*V_{cd}]^2 \quad (7.180)$$

where the extra minus sign is that in the K_S^0 wavefunction. In the Wolfenstein parametrization of the CKM matrix, the only factor in this formula is that has a

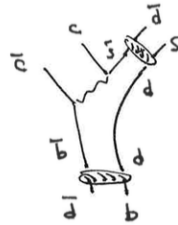


Figure 7.29: Decay through B^0 - \bar{B}^0 mixing, followed by the process $\bar{b} \rightarrow \bar{c}c\bar{s}$. The diagram represents a term proportional to $V_{cb}^* V_{cs}$.

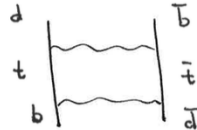


Figure 7.30: The diagram represents a term proportional to $V_{tb} V_{td}^* V_{td} V_{tb}$.

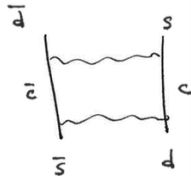


Figure 7.31: The diagram represents a term proportional to $V_{cs}^* V_{cd} V_{cd} V_{cs}$.

phase is V_{td} , which can be represented as:

$$V_{td} = A\lambda^3(1 - \rho i\eta) = \mathcal{C}e^{-i\beta} \quad (7.181)$$

Therefore, the relative phase between the two paths is $-e^{2i\beta}$. Any phases arising from the strong interaction matrix elements are identical along the two paths and factor out of the decay amplitude.

The B^0 - \bar{B}^0 system is somewhat simpler than the K^0 - \bar{K}^0 system, in that the hadronic decays of the B meson are decays to complex multiparticle final states with both possible values of CP . Hence, the decay rates of the two mass eigenstates are nearly equal, so that $4\delta\Gamma$ can be neglected. The B^0 - \bar{B}^0 mass matrix is then well approximated by:

$$\mathbf{M} = \begin{pmatrix} \bar{m} - i\frac{\Gamma}{2} & -e^{2i\beta}\delta m \\ -e^{2i\beta}\delta m & \bar{m} - i\frac{\Gamma}{2} \end{pmatrix} \quad (7.182)$$

The parameter δm is real-valued and it turns out to be positive. The lifetime of the B^0 mesons is:

$$\tau = 1.52 \cdot 10^{-12} \text{ s} \quad (7.183)$$

corresponding to a decay rate:

$$\Gamma = 4.3 \cdot 10^{-13} \text{ GeV} \quad (7.184)$$

The eigenstates of the matrix \mathbf{M} are:

$$|B_L^0\rangle = \frac{1}{\sqrt{2}}(|B^0\rangle + e^{-2i\beta}|\bar{B}^0\rangle) \quad (7.185)$$

$$|B_H^0\rangle = \frac{1}{\sqrt{2}}(|B^0\rangle - e^{-2i\beta}|\bar{B}^0\rangle) \quad (7.186)$$

with eigenvalues:

$$\bar{m} - \frac{\delta m}{2} - i\frac{\Gamma}{2} \quad (7.187)$$

$$\bar{m} + \frac{\delta m}{2} - i\frac{\Gamma}{2} \quad (7.188)$$

for B_L^0 and B_H^0 respectively. The mass difference of the two states is:

$$m_H - m_L = \delta m = 3.3 \cdot 10^{-13} \text{ GeV} \quad (7.189)$$

The value of $(m_H - m_L)$ is accidentally quite close to the decay rate Γ . This means that the time-dependent interference terms in B^0 decay might be observable.

The states $|B_L^0\rangle$ and $|B_H^0\rangle$ have simple time-dependence, for example:

$$|B_L^0(\tau)\rangle = e^{-i(\bar{m}-\frac{\delta m}{2}-i\frac{\Gamma}{2})\tau} |B_L^0\rangle \quad (7.190)$$

Then, we can use the eigenstates of the matrix \mathbf{M} to compute the time-dependence of the B^0 and \bar{B}^0 states. For $|B\rangle^0$:

$$\begin{aligned} |B^0(\tau)\rangle &= \frac{1}{\sqrt{2}} [|B_L^0(\tau)\rangle + |B_H^0(\tau)\rangle] \\ &= e^{-i\bar{m}\tau-\Gamma\frac{\tau}{2}} \left[|B^0\rangle \cos\left(\frac{\delta m\tau}{2}\right) + i |\bar{B}^0\rangle e^{-2i\beta} \sin\left(\frac{\delta m\tau}{2}\right) \right] \end{aligned} \quad (7.191)$$

Similarly, for $|\bar{B}^0\rangle$:

$$|\bar{B}^0(\tau)\rangle = e^{-i\bar{m}\tau-\Gamma\frac{\tau}{2}} \left[|\bar{B}^0\rangle \cos\left(\frac{\delta m\tau}{2}\right) + i |B^0\rangle e^{+2i\beta} \sin\left(\frac{\delta m\tau}{2}\right) \right] \quad (7.192)$$

We have now dealt with the B^0 - \bar{B}^0 mixing, so all that remains is to the decay of the B^0 and \bar{B}^0 states directly to $J/\psi K_S^0$. Recalling again that there is a minus sign between the $s\bar{d}$ and $d\bar{s}$ components of the K_S^0 , the matrix elements for the full process of time evolution and decay have the form:

$$\mathcal{M}(B^0(\tau) \rightarrow J/\psi K_S^0) = e^{-i\bar{m}\tau-\Gamma\frac{\tau}{2}} \mathcal{A} \left[|B^0\rangle \cos\left(\frac{\delta m\tau}{2}\right) - i |\bar{B}^0\rangle e^{-2i\beta} \sin\left(\frac{\delta m\tau}{2}\right) \right] \quad (7.193)$$

$$\mathcal{M}(\bar{B}^0(\tau) \rightarrow J/\psi K_S^0) = e^{-i\bar{m}\tau-\Gamma\frac{\tau}{2}} \mathcal{A} \left[|\bar{B}^0\rangle \cos\left(\frac{\delta m\tau}{2}\right) - i |B^0\rangle e^{+2i\beta} \sin\left(\frac{\delta m\tau}{2}\right) \right] \quad (7.194)$$

The decay amplitude \mathcal{A} can be complex, with a phase due to the strong interaction, but this factor is the same for B^0 and \bar{B}^0 decays due to the CP invariance of the strong interaction. Squaring the amplitudes in the previous formulae, we find the time-dependence of the decay rates:

$$\Gamma(B^0(\tau) \rightarrow J/\psi K_S^0) = e^{-\Gamma\tau} [1 - \sin(\delta m\tau) \sin(2\beta)] \quad (7.195)$$

$$\Gamma(\bar{B}^0(\tau) \rightarrow J/\psi K_S^0) = e^{-\Gamma\tau} [1 + \sin(\delta m\tau) \sin(2\beta)] \quad (7.196)$$

The asymmetry in the rates is:

$$\frac{\Gamma(\bar{B}^0 \rightarrow J/\psi K_S^0) - \Gamma(B^0 \rightarrow J/\psi K_S^0)}{\Gamma(\bar{B}^0 \rightarrow J/\psi K_S^0) + \Gamma(B^0 \rightarrow J/\psi K_S^0)} = + \sin(\delta m\tau) \sin(2\beta) \quad (7.197)$$

The decay is shifted forward in time for an \bar{B}^0 and backward in time for an initial B^0 . The asymmetry is predicted to have a time-dependence governed by δm with amplitude $\sin 2\beta$. For the process $B^0/\bar{B}^0 \rightarrow J/\psi K_L^0$, the relative minus sign in the decay amplitudes from B^0 and \bar{B}^0 becomes a plus sign and so the asymmetry takes the minus sign. The angle β is the phase angle taken directly from CKM matrix, without corrections due to strong interaction.

The first thing to do in order to understand the time-dependent asymmetry is to find a way to produce a sufficient quantity of B^0 and \bar{B}^0 mesons. This can be done e^+e^- annihilation, which leads to a state with $J = 1$. This means that for the production of spin-0 mesons, the two mesons are in an $L = 1$ wavefunction, antisymmetric in the other meson quantum numbers. In particular, the B mesons go outward from the production point and, after some time, one of the mesons decays. If it decays to an e^+ or a μ^+ , this event tags this meson (at this time) as a B^0 . The other meson must then be a \bar{B}^0 . This state propagates for an additional time Δt , possibly mixing to B^0 during that time, and then decays to the observed final state. Note that the relative time Δt might be negative if the leptonic decay takes place after the selected exclusive decay. These processes are schematized in Figure 7.32.

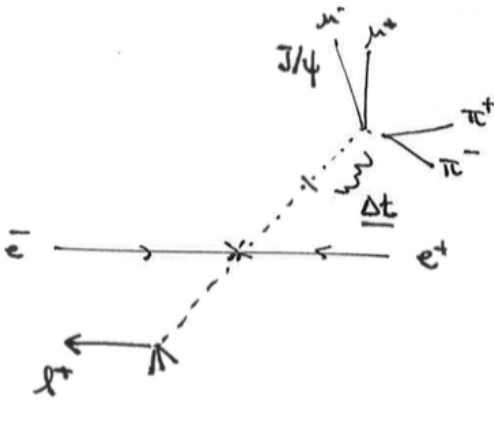


Figure 7.32: Production of B^0 and \bar{B}^0 mesons through e^+e^- annihilation and decay products.

The lifetime of the B meson is about 1.5 ps, so it is difficult to measure the decay time directly. A possibility is to construct an asymmetric colliding beam accelerator, in which the e^+e^- center of mass frame is moving with respect to the lab. The boost of the center of mass is approximately $v/c \sim 0.5$. Therefore, two B decays would be separated by about 200 μm , which is a resolvable distance for a silicon tracking detector which pinpoints the decay vertices.

In the late 1990's, two asymmetric e^+e^- colliders were constructed, one at SLAC (9.0 GeV $e^- \times 3.1$ GeV e^+), for the BaBar experiment, and one at KEK in Tsukuba, Japan (8.0 GeV $e^- \times 3.5$ GeV e^+), for BELLE experiment. In 2001, both experiments observed the CP -violating asymmetry in $B^0 \rightarrow J/\psi K_S^0$.

In Figure 7.33 it is presented the displacements of the decay distributions for $B^0 \rightarrow J/\psi K^0$ and $\bar{B}^0 \rightarrow J/\psi K^0$ measured by the BaBar experiment. The distributions are labelled by the tagging B meson, so the points labeled " B^0 tags" indicate $\bar{B}^0(\tau)$ decays, and vice versa. The distributions for B^0 and \bar{B}^0 are shifted substantially with respect to one another, in just the directions predicted below. The shifts are in the opposite directions for K_L^0 instead of K_S^0 in the final state.

The current best value of β from this measurement is:

$$\sin 2\beta = 0.679 \pm 0.20 \quad (7.198)$$

that is, $\beta = 21^\circ$. This is indeed a large CP -violating effect.

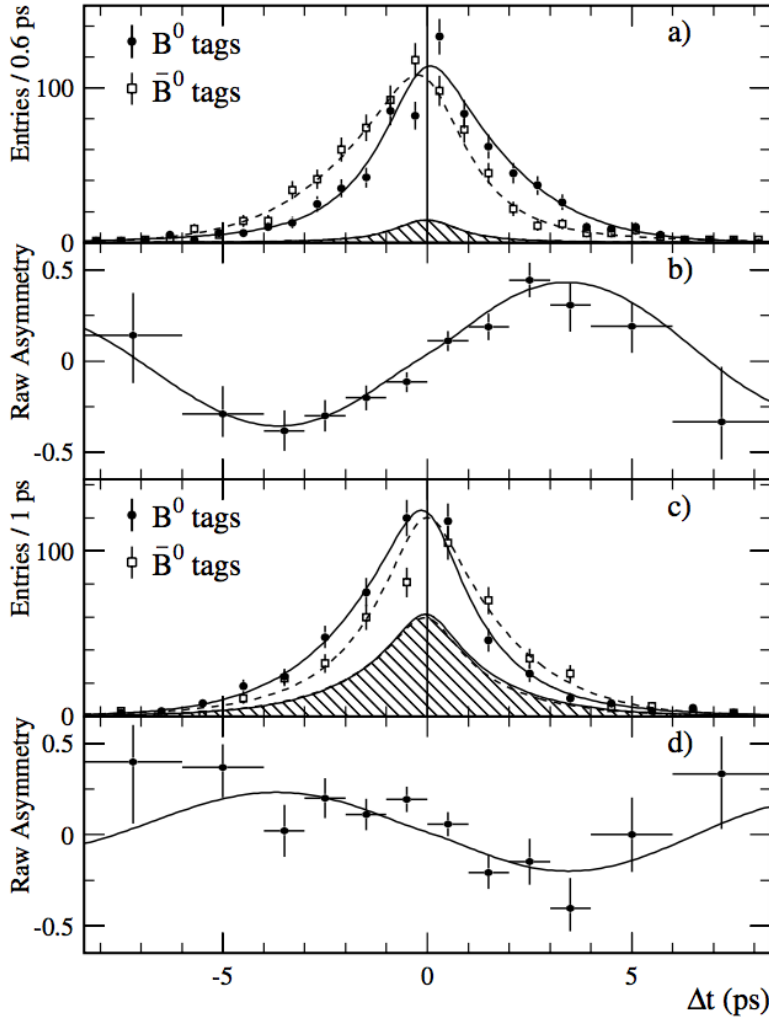


Figure 7.33: Proper time distribution of $B^0\bar{B}^0 \rightarrow J/\psi K^0$ decays at the $\Upsilon(4S)$, measured by the BaBar experiment at the PEP-II collider at SLAC. Panel (a) shows the decay distributions for $B^0\bar{B}^0 \rightarrow J/\psi K_S^0$. Panel (b) shows the rate asymmetry. Panel (c) shows the decay distributions for $B^0\bar{B}^0 \rightarrow J/\psi K_L^0$. Panel (d) shows the corresponding rate asymmetry.

Concerning the angles α and γ , they can also be measured by observable parameters of B decays. The angle α is given by time-dependent asymmetries in B decay to light quarks:

$$B^0 \rightarrow \pi^+ \pi^- \quad (7.199)$$

$$B^0 \rightarrow \pi^\pm \rho^\mp \quad (7.200)$$

$$B^0 \rightarrow \rho^+ \rho^- \quad (7.201)$$

The angle γ can be extracted from asymmetries in B decays to DK . These constraints are shown in Figure ??, together with constraints from the value of $|V_{ub}|$, the values of the B^0 - \bar{B}^0 mixing amplitude, the value of B_s^0 - \bar{B}_s^0 mixing amplitude, and the value of ε from the neutral K system. In the Standard Model, all of these parameters must be consistent with a common value of $(\rho + i\eta)$.

So, any quantum field theory is invariant under CPT , so CP violation implies T violation. However, it is interesting to ask whether one can directly see T violation in heavy quark decays. The BaBar experiment demonstrated this in the following way: We have seen that, in e^+e^- annihilation, B mesons are produced as pairs in a quantum coherent wavefunction. The decay of one meson breaks the coherence, identifying one meson of the pair as a B^0 or a \bar{B}^0 , for a leptonic decay, or as a

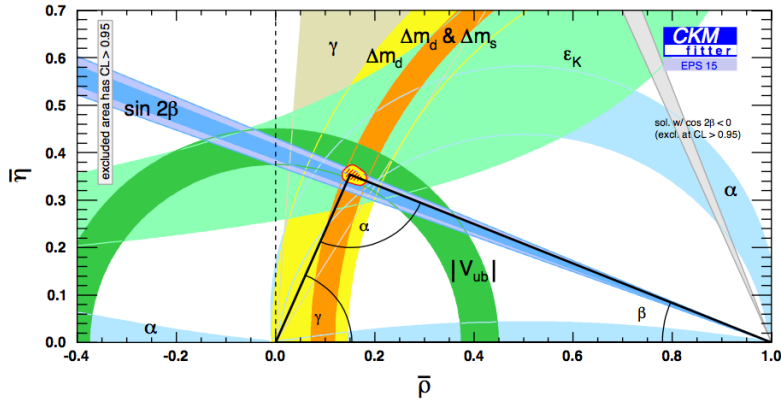


Figure 7.34: Constraints on the CKM parameters (ρ, η) from measurements of CP violation, showing the fit by the CKMFitter collaboration.

$CP = +$ or $CP = -$ state (B_+ or B_-), for a decay to a CP eigenstate. We can then pick out events in which the leptonic decay happens first, followed by time evolution to a CP eigenstate, and also events in which the CP decay happens first, followed by time evolution to a state with a definite leptonic decay. If the equations of motion of nature were T symmetric, the rates for time evolution in the two directions would be equal. They are not. The asymmetries between the rates for pairs of time-reversed processes (e.g., $B^0 \rightarrow B_-$ vs. $B_- \rightarrow B^0$) are shown in Figure 7.35. Note that the asymmetries reverse when one changes from B^0 to \bar{B}^0 and from even to odd CP , consistent with the physics described above. This is the most direct evidence that the equations of nature violate time reversal invariance.

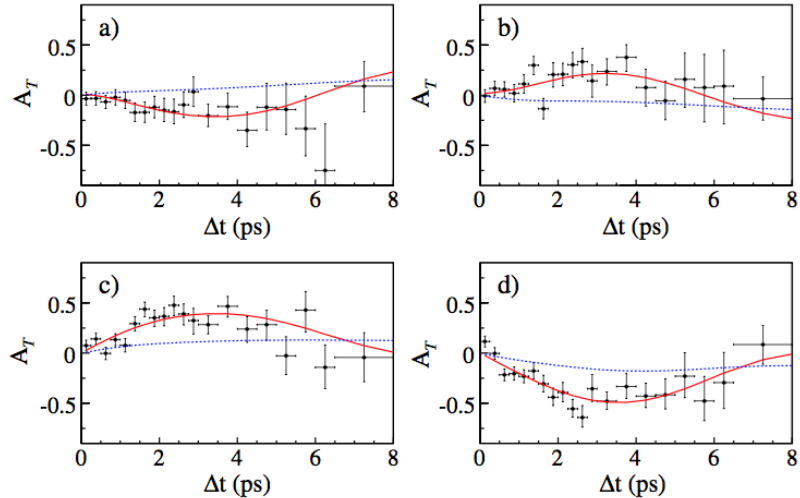


Figure 7.35: Time reversal violating asymmetries measured as a function of proper time by the BaBar experiment at the PEP-II collider. The four panels refer to the transitions: $\dot{\bar{B}}^0 \rightarrow B_-$ (a), $B_+ \rightarrow B^0$ (b), $\bar{B}^0 \rightarrow B_+$ (c), $B_- \rightarrow B^0$ (d).

Chapter 8

New Physics

8.1 Neutrino and Standard Model

8.1.1 Neutrino mass and β decay

The neutrino was introduced by Pauli in the study of β decay. This requires that the mass of the electron neutrino, at least, is very small. A bound on the mass of ν_e can be set by studying in particular the endpoint of the electron energy distribution. If we consider the rate for the β decay of a nucleus A to B , it has the following form:

$$\Gamma(A \rightarrow Be^- \bar{\nu}) = \frac{1}{2m_A} \int \frac{d^3 p_B d^3 p_e d^3 p_\nu}{(2\pi)^9 2E_B 2E_e 2E_\nu} (2\pi)^4 \delta^{(4)}(p_A - p_B - p_e - p_\nu) |\mathcal{M}|^2 \quad (8.1)$$

Since we are interested to the endpoint of e^- spectrum, we will have that $|\mathcal{M}|^2$ is approximately constant in our study. A and B are very heavy compared to their mass difference (typically of few MeV). So, it is also a good approximation to assume that the final nucleus B takes up the recoil momentum, so that the directions of the electron and neutrino are uncorrelated. In this limit, the energies of the final electron and neutrino sum to:

$$E_e + E_\nu = m(A) - m(B) = \Delta m_{AB} \quad (8.2)$$

Then, the rate becomes:

$$\Gamma(A \rightarrow Be^- \bar{\nu}) = \frac{1}{2m_A} \frac{1}{(2\pi)^5 2m_B} \int \frac{dp_e p_e^2}{2E_e} \int \frac{dp_\nu p_\nu^2}{2E_\nu} \delta(\Delta m_{AB} - E_e - E_\nu) |\mathcal{M}|^2 \quad (8.3)$$

Using:

$$dp_e p_e = dE_e E_e$$

$$dp_\nu p_\nu = dE_\nu E_\nu$$

we can write the decay rate as:

$$\Gamma \sim \int_{m_e}^{\Delta m_{AB}} dE_e \int_0^{\Delta m_{AB} - E_e} dE_\nu p_\nu \quad (8.4)$$

Assuming that the neutrino has zero mass, this gives:

$$\frac{d\Gamma}{dE_e} \sim (\Delta m_{AB} - E_e)^2 \quad (8.5)$$

This energy distribution is conventionally represented by a **Kurie plot**, in Figure 8.1, plotting the square root of the event rate as a function of the electron energy.

Lecture 22.
Tuesday 26th May, 2020.
Compiled: Wednesday 10th June, 2020.

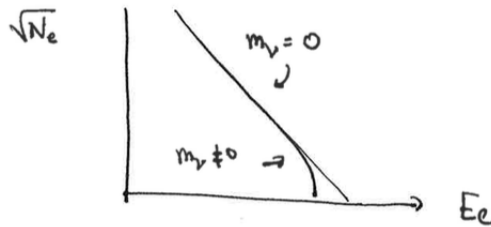


Figure 8.1: Example of Fermi-Kurie plot.

This should be a straight line for a zero mass neutrino. However, if the neutrino is massive, the plot falls off the kinematic endpoint:

$$E_e = \Delta m_{AB} - m_\nu \quad (8.6)$$

Measurements of β decay exclude ν_e masses of more than a few eV. However, β decay is not the most adequate way to measure m_ν mass. The β electron can lose an energy of order eV when it exits the atom, and it loses eV/mm in traversing material. These energy losses must be accounted for in the interpretation of the electron energy distribution. The most accurate measure up to 2019 was done by Mainz and Troitsk and it gives the limit:

$$m_{\nu_e} < 2.05 \text{ eV} \quad (8.7)$$

In September 2019, the KATRIN experiment analyzed the decay of gaseous Tritium. From the fit of the collected data, it was found a new limit for the mass of electronic neutrino at 90% CL:

$$m_{\nu_e} < 1.1 \text{ eV} \quad (8.8)$$

The results of the two experiments are showed in Figure 8.2

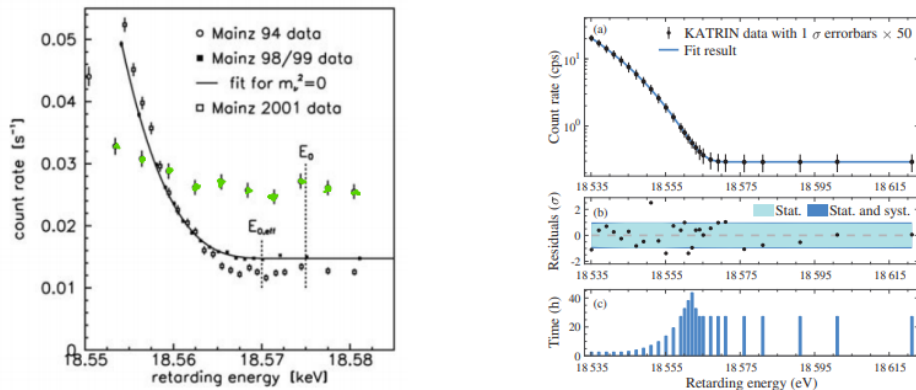


Figure 8.2: Left: measurement of the endpoint of the electron energy spectrum in tritium β decay, from Mainz experiment. Right: KATRIN experiment results, from the analysis of the decay of gaseous Tritium.

Direct limits on ν_μ and ν_τ mass are weaker with respect to the ν_e limit. For them, we can study:



and we find respectively the following limits on the masses:

$$m(\nu_\mu) < 0.19 \text{ MeV} \quad (8.11)$$

$$m(\nu_\tau) < 18.2 \text{ MeV} \quad (8.12)$$

With a cosmology argument, if we have a massive ν that moves relativistically in the early universe, ν would transfer energy and smear out cosmic structure, giving an observably different distribution of clusters of galaxies if the neutrino masses are sufficiently large. The absence of this effect gives a bound estimated to be:

$$\sum_{i=1,2,3} m_{\nu_i} < 0.23 \text{ eV} \quad (8.13)$$

8.1.2 Adding neutrino mass to the Standard Model

Neutrino masses are thus very small compared to the weak interaction mass scale, sufficiently small that it is unclear how they can be observed. To understand the evidence for neutrino mass, we need to develop further the theory of neutrino massses within the Standard Model.

Let's assume the gauge invariance and a $SU(2) \times U(1)$ symmetry. Neutrino masses can arise in one of the following two ways.

The simplest mechanism is to assume that there exist right-handed neutrinos that couple to the left-handed neutrinos through Yukawa couplings. This translates in adding to the Standard Model Lagrangian a term:

$$\Delta\mathcal{L} = -y_\nu^{ij} L_a^{\dagger i} \varepsilon_{ab} \varphi_b^* \nu_R^j + \text{h.c.} \quad (8.14)$$

similar to the u quark mass term that couples to W^\pm . This term can be treated in the same way the quark and lepton mass terms are treated. However, this is not appropriate. In elementary particle reactions, neutrinos are typically emitted at MeV or higher energies, at which effects of eV-scale masses are unimportant. Therefore it is most convenient to retain our earlier convention that the left-handed neutrinos are described in the basis that diagonalizes their weak interactions. We then treat the new term by making the change of variables:

$$L^i \longrightarrow U_{L_{ij}}^{(e)} L^j \quad (8.15)$$

This transforms:

$$y_\nu \longrightarrow y'_\nu = U_L^{(e)\dagger} y_\nu \quad (8.16)$$

This transformation diagonalizes the charged lepton Yukawa matrix but does not necessarily diagonalize the neutrino Yukawa matrix. This basis for neutrino states will be denoted as the basis of **flavor eigenstates**. In this basis, the ν_e is the linear combination of the three neutrino states that is produced in weak interaction decay together with an e^+ , and the ν_μ and ν_τ are defined similarly.

We can now diagonalize y'_ν as before:

$$y'_\nu = U_L^{(\nu)} Y_\nu U_R^{(\nu)} \quad (8.17)$$

where Y_ν is real and diagonal. We can transform away $U_R^{(\nu)}$ but we cannot get rid of the matrix $U_L^{(\nu)}$. This is a fixed unitary transformation between the basis of flavor eigenstates and the basis of mass eigenstates. We will refer to the the mass eigenstates as ν_1, ν_2, ν_3 , with masses m_1, m_2, m_3 . As we did with the quark mixing matrix, we can redefine phases in $U_L^{(\nu)}$ so that $U_L^{(\nu)}$ contains three angles but only one phase. The

mixing matrix $U_L^{(\nu)}$ is called the **Pontecorvo-Maki-Nakagawa-Sakata** or **PMNS matrix** and is more commonly notated V or V_{PMNS} .

There is another way to add neutrino masses to the Standard Model that is consistent with Lorentz invariance and $SU(2) \times U(1)$. We can write:

$$\Delta\mathcal{L} = -\frac{1}{2}\mu_{ij}(L_{a\alpha}^i\varepsilon_{ab}\varphi_b^*)(L_{c\beta}^j\varepsilon_{cd}\varphi_d^*)\varepsilon_{\alpha\beta} \quad (8.18)$$

where $\alpha, \beta = 1, 2$ are the indices of 2-component spinors. This expression is Lorentz-invariant. It does not violate any gauge symmetry of the Standard Model. The expression does violate lepton number, but lepton number conservation is not a postulate in the description of the Standard Model. When the Higgs field φ acquires an expectation value and breaks $SU(2) \times U(1)$, 8.18 leads to a mixing of the ν_L states with their antiparticles $\bar{\nu}_R$, generating masses given by the eigenvalues of:

$$m_{ij} = \mu_{ij}\frac{v^2}{2} \quad (8.19)$$

This mass term, resulting from particle-antiparticle mixing, is called a **Majorana mass term**.

The quantity μ_{ij} has the dimensions $(\text{GeV})^{-1}$, so we might also write the mass formula as:

$$m_{ij} = \frac{\bar{\mu}_{ij}v^2/2}{M} \quad (8.20)$$

where $\bar{\mu}$ is dimensionless and M sets the mass scale.

We can obtain this structure naturally by starting from a Lagrangian with neutrino Yukawa couplings and a lepton-number violating mass term for the right-handed neutrinos:

$$\Delta\mathcal{L} = -\frac{1}{2}M_{ij}\nu_{R\alpha}^i\nu_{R\beta}^j\varepsilon_{\alpha\beta} + \text{h.c.} \quad (8.21)$$

This is a direct Majorana mass term for the right-handed neutrinos. Note that, because the right-handed neutrinos do not transform under $SU(2) \times U(1)$, we are free to write this term without violating any symmetry of the Standard Model. Thus, while quark, lepton, and vector boson masses are restricted to be of the size of the Higgs field expectation value, there is no reason why the scale of masses in M_{ij} cannot be very much larger. When we use the previous mass term together with the neutrino Yukawa coupling, the diagram in Figure 8.3 generates Majorana masses for the left-handed neutrinos of the form of m_{ij} previously defined.

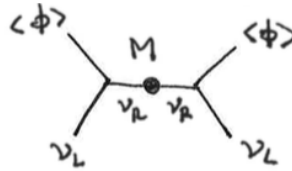


Figure 8.3: Diagram representing generation of Majorana masses for the left-handed neutrinos.

This is called the **seesaw mechanism** for generating small neutrino masses. It produces small masses by a modification of the theory at very high energies.

The consequences of the Majorana mass term for neutrinos are almost the same as those of the Dirac mass term. We can diagonalize the Majorana neutrino mass as:

$$m_{ij} = (V\bar{m}V^T)_{ij} \quad (8.22)$$

where \bar{m} is complex and V is unitary. The matrix V is the PMNS matrix, reducible to three angles and one phase. There are two more possible phases in \bar{m} . These have no significant effect on neutrino flavor oscillations.

The Majorana mass term gives a new weak interaction process: the double β decay. At some points in the periodic table, ordinary β decay is energetically forbidden, but double β decay is allowed. For example:

$$m(\text{Cs}^{136}) > m(\text{Xe}^{136}) > m(\text{Ba}^{136}) \quad (8.23)$$

Then, Xe^{136} can decay by:



However, double β decay is one of the rarest physical processes known. For example, the EXO experiment measured:

$$\tau(\text{Xe}^{136}) = 2 \cdot 10^{21} \text{ yr} \quad (8.25)$$

If the neutrino $\bar{\nu}_e$ has a lepton-number violating Majorana mass term, then also the decay process:



is allowed, with no final-state neutrinos. The rate of this decay is expected to be small even in comparison to the lifetime of Xe^{136} previously given. This and similar decays are being intensively searched for, but none has yet been observed.

8.1.3 The V_{PNMS} effect

We can now describe the physical effect of a neutrino mass term. I choose the process of π^+ decay as an example. The π^+ decays to $\mu^+ \nu_\mu$, that is, specifically to the ν_μ weak interaction eigenstate. The ν_μ is a linear combination of the three mass eigenstates. If the π^+ energy is fixed, the three components are emitted with slightly different values of momentum:

$$p_i = E - \frac{m_i^2}{2E} + \dots \quad (8.27)$$

This is permitted, because the pion decay region is of finite size, allowing the momentum to be uncertain. This uncertainty is small enough that the components of the ν_μ wavefunction are created with quantum coherence.

The outgoing neutrino wavefunction then has the form:

$$\sum_{i=1,2,3} V_{\mu i} e^{+i(E-m_i^2/2E)x} \quad (8.28)$$

At very large distances x , the components of this wavefunction go out of phase. Then the probability of finding a ν_μ is no longer 1. Instead, we find:

$$\text{Prob}(\nu_\mu \rightarrow \nu_\mu) = \left| \sum_i V_{\mu i} V_{\mu i}^* e^{-i(m_i^2/2E)x} \right|^2 \quad (8.29)$$

It is easiest to understand this formula if we evaluate it for the case of two-neutrino mixing with mixing angle θ :

$$V = \begin{pmatrix} \cos \theta & -\sin \theta \\ \sin \theta & \cos \theta \end{pmatrix} \quad (8.30)$$

In that case, the formula becomes:

$$\text{Prob}(\nu_\mu \rightarrow \nu_\mu) = \left| \cos^2 \theta e^{-i(m_1^2/2E)x} + \sin^2 \theta e^{-i(m_2^2/2E)x} \right|^2 \quad (8.31)$$

which can be rewritten as:

$$\text{Prob}(\nu_\mu \rightarrow \nu_\mu) = 1 - \sin^2(2\theta) \sin^2 \left[\frac{\delta m^2}{4E} x \right] \quad (8.32)$$

There is an oscillation between the flavor eigenstates with an oscillation length:

$$L = 4\pi \frac{E}{\Delta m^2} = (2.48 \text{ m}) \frac{E (\text{MeV})}{\Delta m^2 (\text{eV}^2)} \quad (8.33)$$

The conclusion is quite surprising. We can detect the presence of small neutrino masses if the neutrinos also exhibit flavor mixing. Then the effect of the mass term is to generate a **flavor oscillation** as a function of the distance from the neutrino source. For MeV neutrinos with 10^{-2} eV masses or for GeV neutrinos with 10^{-1} eV masses, the length scale of the oscillation can be km.

This is just the opposite of the way that we determine the masses and weak interaction flavor mixing among quarks. For quarks, we observe the particles as mass eigenstates, inside hadrons of definite mass. Decays through the weak interaction show that the mass eigenstates are linear combinations of weak interaction eigenstates. For neutrinos, the primary way that we observe the particles is through weak interaction decay. Then we characterize the neutrino eigenstates according to their weak interaction properties. It is the flavor mixing as the neutrinos travel that demonstrates that there is a mass eigenstate basis, with different masses for the three neutrinos, that is different from the flavor basis.

Lecture 23.

Wednesday 27th

May, 2020.

Compiled:

Wednesday 10th

June, 2020.

8.1.4 Neutrino mixing evidence

Now that we know how to look for neutrino mass, we can discuss the experimental evidence that the neutrino masses are indeed nonzero.

The first clear evidence for neutrino flavor mixing, and, thus, for neutrino mass, came in the study of the neutrinos produced in cosmic ray interactions in the atmosphere. These were observed in underground water Cherenkov detectors originally built to look for proton decay. It was observed that the flux of ν_e from atmospheric interactions was close to the predictions, while the flux of ν_μ was too small by a factor of 2.

In 1998, the SuperKamiokande experiment, a very large water Cherenkov detector in the Kamioka mine in Japan, resolved this question by observing the directions of ν_μ 's from their conversion to muons in charge-changing interactions. The downward-going ν_μ were present with a flux that was essentially unsuppressed, while upward-going ν_μ , created on the other side of the earth, were highly suppressed. For ν_e , the ratio of the predicted to the observed flux was independent of direction. The data is showed in Figure 8.4.

This strongly indicated a flavor mixing $\nu_\mu \leftrightarrow \nu_\tau$ on the scale of the Earth's diameter. The mixing angle was consistent with a maximal value:

$$\sin^2(2\theta) = 1 \quad (8.34)$$

This flavor mixing has since been confirmed by accelerator experiments that create beams of ν_μ at GeV energies and detect the neutrinos over a long path length. Some examples are K2K and MINOS experiments. The current best values of the oscillation

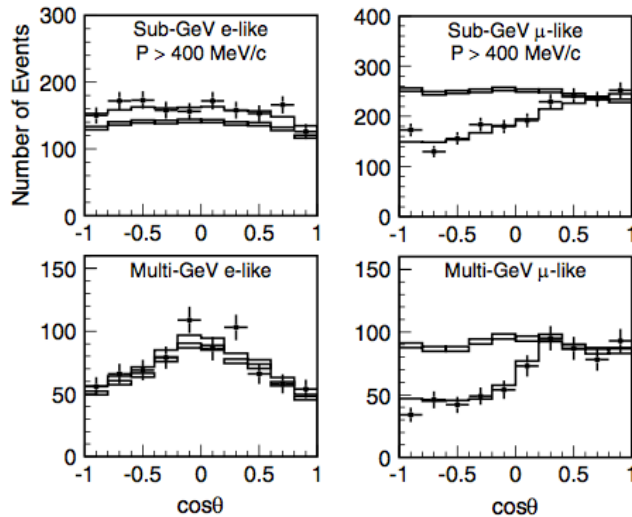


Figure 8.4: Measurement of the flux of electron and muon type neutrinos from atmospheric cosmic ray events, compared to models of neutrino production with and without neutrino mixing.

parameters are:

$$\Delta m^2 = (2.43 \pm 0.08) \cdot 10^{-3} \text{ eV}^2 = (5 \cdot 10^{-2} \text{ eV})^2 \quad (8.35)$$

$$\sin^2 \theta = 0.386 \pm 0.023 \quad (8.36)$$

The mass of the ν_e is related to another long-standing anomaly in neutrino physics. In the 1960's, John Bahcall suggested testing the mechanism of energy generation in the sun by observing the flux of neutrinos produced by the sun. Raymond Davis took up the challenge. He designed an experiment with a tank containing 600 tons of CCl_4 underground in the Homestake mine in South Dakota. Solar neutrinos would convert Cl^{37} to Ar^{37} at the rate of atoms/month. The radioactive Ar atoms could then be extracted and counted. The rate of Ar production was observed to be consistently low compared to the solar model prediction.

The production of neutrinos by the sun is quite complex. The dominant process, accounting for 99% of solar neutrinos, is:



where D is a deuterium nucleus. However, the resulting neutrinos, at 0.5 MeV energy, are of too low energy to be detected in Davis's experiment. Instead, rarer reactions are needed to give neutrinos of energy above the 0.8 MeV threshold for this detection technique. A typical solar neutrino spectrum is showed in Figure 8.5.

Over the decades, solar neutrino experiments were mounted in other energy regions, and eventually experiments with a gallium detection medium observed the neutrinos from the dominant pp process. Always, the rate was smaller than required.

Finally, the situation was resolved by the Sudbury Neutrino Observatory (SNO) experiment, using a heavy water (D_2O) Cherenkov detector located in the Sudbury mine in northern Ontario. This experiment was sensitive only to the highest energy solar neutrinos, from $\text{B}^8 \rightarrow \text{Be}^8 e^+ \nu_e$. However, it was able to simultaneously observe three different neutrino reactions:



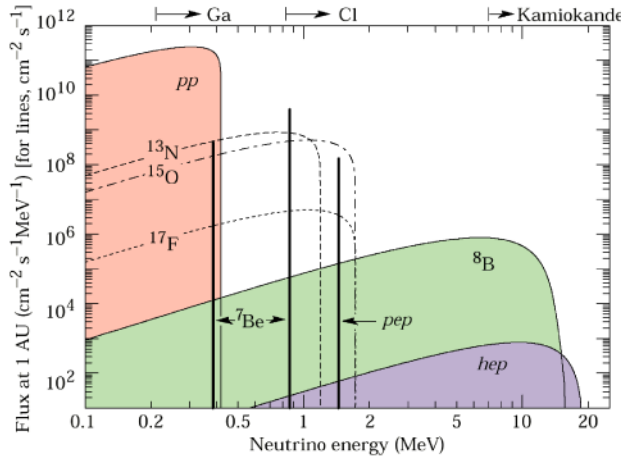


Figure 8.5: Predicted energy spectrum of neutrinos from the sun.

The first reaction, charged current neutrino scattering from deuterium, measures the flux of ν_e . The second reaction is the neutral current scattering from deuterium, which has equal cross section for all three neutrino species. Neutrino-electron scattering is sensitive to all neutrino species, but the cross section for ν_e is larger than that for ν_μ , ν_τ by about a factor 6, reflecting contributions from both Z and W exchange processes, in Figure 8.6.

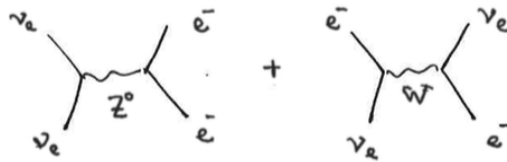


Figure 8.6: Z and W exchange processes.

The flux determinations from SNO are shown in 8.7. The flux of ν_e is indeed smaller than expected by more than a factor of 2, but the total neutrino flux is in good agreement with the prediction for ν_e production in solar models. Apparently, the solar neutrinos are converting to ν_μ and ν_τ on their way to the earth.

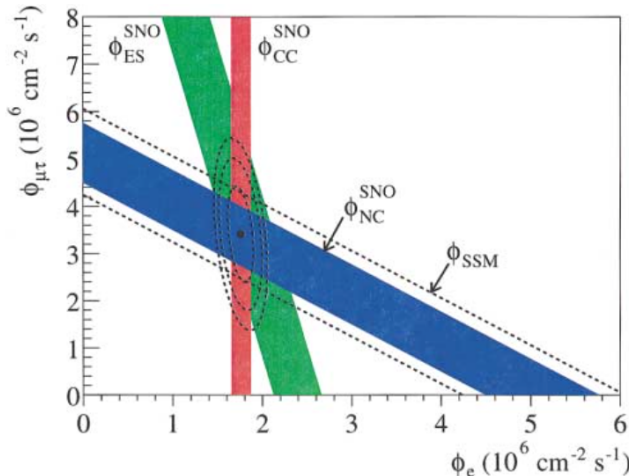


Figure 8.7: luxes of solar neutrinos of the various types, extracted from the data of the SNO experiment. The estimates of ν_e and ν_μ/ν_τ fluxes from the three processes listed in Eqs. 8.38-8.40 are showed as the red, blue, and green bands, respectively.

This neutrino flavor oscillation, which requires a small Δm^2 , was confirmed by the KamLAND experiment, a scintillator detector in the Kamioka mine which observed neutrinos from nuclear reactors in Japan at baselines of order 100 km. The oscillation in the $\bar{\nu}_e$ survival probability as a function of neutrino energy is shown in 8.8.

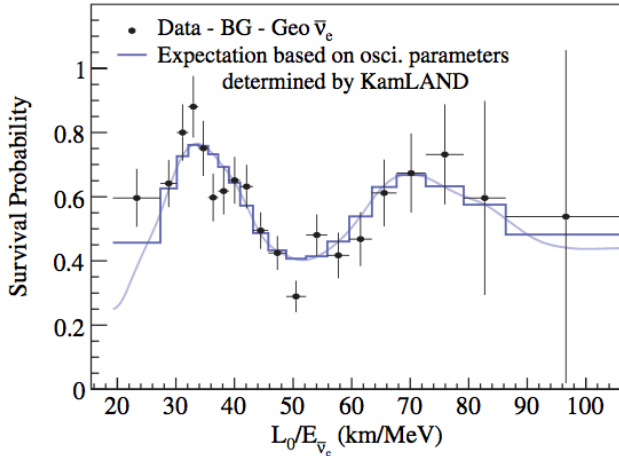


Figure 8.8: Probability of $\nu_e \rightarrow \bar{\nu}_e$ for neutrinos from nuclear reactors as a function of proper time, as measured by the KamLAND experiment.

The current best values for the oscillation parameters are:

$$\Delta m^2 = (7.54 \pm 0.024) \cdot 10^{-5} \text{ eV}^2 = (0.9 \cdot 10^{-2} \text{ eV})^2 \quad (8.41)$$

$$\sin^2 \theta = 0.307 \pm 0.017 \quad (8.42)$$

So, there are two small neutrino mass differences of rather different scale. The large ratio between the two Δm^2 values justifies the use of two-neutrino mixing formula to parametrize each oscillation. The values of Δm^2 imply that all of the neutrino masses must be within about 0.1 eV of one another. However, these results do not give the absolute scale of neutrino masses. They also do not give the ordering of the levels. There are two possibilities, called the **normal** and **inverted hierarchy**, represented in Figure 8.9.

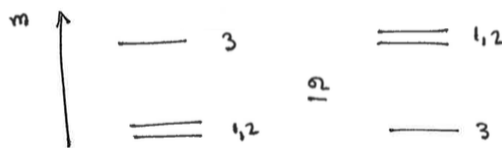


Figure 8.9: Normal and inverted neutrino mass hierarchy.

In each case, the isolated mass eigenstate is an almost pure combination of ν_μ and ν_τ , while the two closely spaced states mix ν_e with the orthogonal linear combination of ν_μ and ν_τ .

It is possible in principle to distinguish these possibilities by observing the effect on neutrino mixing of neutrino interactions with matter as the neutrinos pass through the Earth over hundreds of km. So far, the issue has not been resolved.

The next question we might address is that of whether ν_3 contains some admixture of ν_e . This mixing is controlled by the third mixing angle in the PMNS matrix. It can be detected by looking for an oscillation of reactor neutrinos at the oscillation Δm^2 of the atmospheric neutrino oscillation, which corresponds to a km wavelength for neutrinos of MeV energy. This was finally observed in 2012 by the reactor experiments Daya Bay, in China, and RENO, in Korea. These experiments constructed closely

Lecture 24.
Monday 1st June,
2020.
Compiled:
Wednesday 10th
June, 2020.

matched pairs of detectors and contrasted the rate observed in a “far” detector with that predicted from the rate observed in a “near” detector. Figure 8.10 shows the comparison of near and far detector fluxes at Daya Bay.

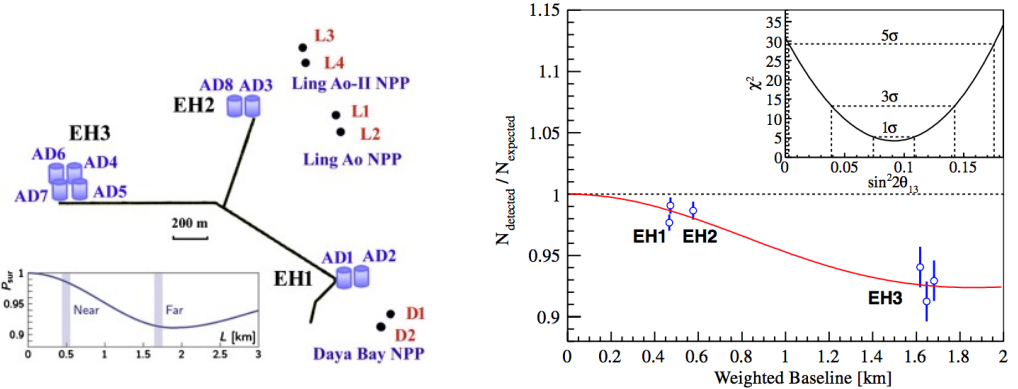


Figure 8.10: (Right) Probability of $\nu_e \rightarrow \nu_e$ for neutrinos from nuclear reactors as a function of distance from the reactor, as measured by the Daya Bay experiment (Left).

The value of the third neutrino mixing angle is:

$$\sin^2 \theta_{13} = 0.0241 \pm 0.0025 \quad (8.43)$$

The question remains of whether the possible phase in the PMNS matrix is nonzero. There is room for this CP -violating term in the neutrino mass matrix. Still, it is a fundamental question whether the couplings of the neutrinos violate CP and T . In principle, CP violation in the neutrino system can be measured by observing asymmetries such as:

$$\text{Prob}(\nu_\mu \rightarrow \nu_e) \neq \text{Prob}(\bar{\nu}_\mu \rightarrow \bar{\nu}_e) \quad (8.44)$$

8.1.5 Summary of experimental results

Experiment	Dominant	Important
Solar Experiments	θ_{12}	$\Delta m_{21}^2, \theta_{13}$
Reactor LBL (KamLAND)	Δm_{21}^2	θ_{12}, θ_{13}
Reactor MBL (Daya-Bay, Reno, D-Chooz)	$\theta_{13}, \Delta m_{31,32}^2 $	
Atmospheric Experiments (SK, IC-DC)		$\theta_{23}, \Delta m_{31,32}^2 , \theta_{13}, \delta_{CP}$
Accel LBL $\nu_\mu, \bar{\nu}_\mu$, Disapp (K2K, MINOS, T2K, NO ν A)	$ \Delta m_{31,32}^2 , \theta_{23}$	
Accel LBL $\nu_e, \bar{\nu}_e$ App (MINOS, T2K, NO ν A)	δ_{CP}	θ_{13}, θ_{23}

Figure 8.11: Experiments contributing to the present determination of the oscillation parameters. Taken from [5].

Lecture 25.
Wednesday 3rd
June, 2020.
Compiled:
Wednesday 10th
June, 2020.

8.2 Higgs boson and properties

8.2.1 Expected properties of the Higgs boson

Now we look into the more specific properties of the Higgs field as predicted by the Standard Model. The Higgs field of the Standard Model contains only 4 degrees of freedom. We saw that 3 of these are Goldstone bosons that are eaten as the W and Z bosons obtain mass. What remains is only 1 dynamical field, the Higgs field $h(x)$. In the Standard Model Lagrangian $h(x)$ always appears together with the Higgs field

NO Param	Ref. [188] w/o SK-ATM		Ref. [188] w SK-ATM		Ref. [189] w SK-ATM		Ref. [190] w SK-ATM	
	Best Fit Ordering		Best Fit Ordering		Best Fit Ordering		Best Fit Ordering	
	bfp $\pm 1\sigma$	3σ range	bfp $\pm 1\sigma$	3σ range	bfp $\pm 1\sigma$	3σ range	bfp $\pm 1\sigma$	3σ range
$\sin^2 \theta_{12}$	$3.10^{+0.13}_{-0.12}$	$2.75 \rightarrow 3.50$	$3.10^{+0.13}_{-0.12}$	$2.75 \rightarrow 3.50$	$3.04^{+0.14}_{-0.13}$	$2.65 \rightarrow 3.46$	$3.20^{+0.20}_{-0.16}$	$2.73 \rightarrow 3.79$
$\theta_{12}/^\circ$	$33.82^{+0.78}_{-0.76}$	$31.61 \rightarrow 36.27$	$33.82^{+0.78}_{-0.76}$	$31.61 \rightarrow 36.27$	$33.46^{+0.87}_{-0.88}$	$30.98 \rightarrow 36.03$	$34.5^{+1.2}_{-1.0}$	$31.5 \rightarrow 38.0$
$\sin^2 \theta_{23}$	$5.58^{+0.20}_{-0.33}$	$4.27 \rightarrow 6.09$	$5.63^{+0.18}_{-0.24}$	$4.33 \rightarrow 6.09$	$5.51^{+0.19}_{-0.80}$	$4.30 \rightarrow 6.02$	$5.47^{+0.20}_{-0.30}$	$4.45 \rightarrow 5.99$
$\theta_{23}/^\circ$	$48.3^{+1.2}_{-1.9}$	$40.8 \rightarrow 51.3$	$48.6^{+1.0}_{-1.4}$	$41.1 \rightarrow 51.3$	$47.9^{+1.1}_{-4.0}$	$41.0 \rightarrow 50.9$	$47.7^{+1.2}_{-1.7}$	$41.8 \rightarrow 50.7$
$\sin^2 \theta_{13}$	$2.241^{+0.066}_{-0.065}$	$2.046 \rightarrow 2.440$	$2.237^{+0.066}_{-0.065}$	$2.044 \rightarrow 2.435$	$2.14^{+0.09}_{-0.07}$	$1.90 \rightarrow 2.39$	$2.160^{+0.083}_{-0.069}$	$1.96 \rightarrow 2.41$
$\theta_{13}/^\circ$	$8.61^{+0.13}_{-0.13}$	$8.22 \rightarrow 8.99$	$8.60^{+0.13}_{-0.13}$	$8.22 \rightarrow 8.98$	$8.41^{+0.18}_{-0.14}$	$7.9 \rightarrow 8.9$	$8.45^{+0.16}_{-0.14}$	$8.0 \rightarrow 8.9$
$\delta_{CP}/^\circ$	$222^{+1.2}_{-2.8}$	$141 \rightarrow 370$	$221^{+0.9}_{-2.8}$	$144 \rightarrow 357$	$238^{+0.11}_{-33}$	$149 \rightarrow 358$	$218^{+0.8}_{-27}$	$157 \rightarrow 349$
Δm_{21}^2	$7.39^{+0.21}_{-0.20}$	$6.79 \rightarrow 8.01$	$7.39^{+0.21}_{-0.20}$	$6.79 \rightarrow 8.01$	$7.34^{+0.17}_{-0.14}$	$6.92 \rightarrow 7.91$	$7.55^{+0.20}_{-0.16}$	$7.05 \rightarrow 8.24$
$\frac{1}{10^{-5}} \text{eV}^2$	$2.449^{+0.032}_{-0.030}$	$2.358 \rightarrow 2.544$	$2.454^{+0.029}_{-0.031}$	$2.362 \rightarrow 2.544$	$2.419^{+0.035}_{-0.032}$	$2.319 \rightarrow 2.521$	2.424 ± 0.03	$2.334 \rightarrow 2.524$
IO	$\Delta\chi^2 = 6.2$		$\Delta\chi^2 = 10.4$		$\Delta\chi^2 = 9.5$		$\Delta\chi^2 = 11.7$	
$\sin^2 \theta_{12}$	$3.10^{+0.13}_{-0.12}$	$2.75 \rightarrow 3.50$	$3.10^{+0.13}_{-0.12}$	$2.75 \rightarrow 3.50$	$3.03^{+0.14}_{-0.13}$	$2.64 \rightarrow 3.45$	$3.20^{+0.20}_{-0.16}$	$2.73 \rightarrow 3.79$
$\theta_{12}/^\circ$	$33.82^{+0.78}_{-0.76}$	$31.61 \rightarrow 36.27$	$33.82^{+0.78}_{-0.75}$	$31.62 \rightarrow 36.27$	$33.40^{+0.87}_{-0.81}$	$30.92 \rightarrow 35.97$	$34.5^{+1.2}_{-1.0}$	$31.5 \rightarrow 38.0$
$\sin^2 \theta_{23}$	$5.63^{+0.19}_{-0.26}$	$4.30 \rightarrow 6.12$	$5.65^{+0.17}_{-0.22}$	$4.36 \rightarrow 6.10$	$5.57^{+0.17}_{-0.24}$	$4.44 \rightarrow 6.03$	$5.51^{+0.18}_{-0.30}$	$4.53 \rightarrow 5.98$
$\theta_{23}/^\circ$	$48.6^{+1.1}_{-1.5}$	$41.0 \rightarrow 51.5$	$48.8^{+1.0}_{-1.2}$	$41.4 \rightarrow 51.3$	$48.2^{+1.0}_{-1.4}$	$41.8 \rightarrow 50.9$	$47.9^{+1.0}_{-1.7}$	$42.3 \rightarrow 50.7$
$\sin^2 \theta_{13}$	$2.261^{+0.067}_{-0.064}$	$2.066 \rightarrow 2.461$	$2.259^{+0.065}_{-0.065}$	$2.064 \rightarrow 2.457$	$2.18^{+0.08}_{-0.07}$	$1.95 \rightarrow 2.43$	$2.220^{+0.074}_{-0.076}$	$1.99 \rightarrow 2.44$
$\theta_{13}/^\circ$	$8.65^{+0.13}_{-1.12}$	$8.26 \rightarrow 9.02$	$8.64^{+0.12}_{-0.23}$	$8.26 \rightarrow 9.02$	$8.49^{+0.15}_{-0.14}$	$8.0 \rightarrow 9.0$	$8.53^{+0.14}_{-0.15}$	$8.1 \rightarrow 9.0$
$\delta_{CP}/^\circ$	$285^{+1.2}_{-26}$	$205 \rightarrow 354$	$282^{+0.25}_{-25}$	$205 \rightarrow 348$	$247^{+0.26}_{-27}$	$193 \rightarrow 346$	$281^{+0.23}_{-27}$	$202 \rightarrow 349$
Δm_{21}^2	$7.39^{+0.21}_{-0.20}$	$6.79 \rightarrow 8.01$	$7.39^{+0.21}_{-0.20}$	$6.79 \rightarrow 8.01$	$7.34^{+0.17}_{-0.14}$	$6.92 \rightarrow 7.91$	$7.55^{+0.20}_{-0.16}$	$7.05 \rightarrow 8.24$
$\frac{1}{10^{-5}} \text{eV}^2$	$-2.509^{+0.032}_{-0.032}$	$-2.603 \rightarrow -2.416$	$-2.510^{+0.030}_{-0.031}$	$-2.601 \rightarrow -2.419$	$-2.478^{+0.035}_{-0.033}$	$-2.577 \rightarrow -2.375$	-2.50 ± 0.04	$-2.59 \rightarrow -2.39$
$\frac{1}{10^{-3}} \text{eV}^2$	$-2.509^{+0.032}_{-0.032}$	$-2.603 \rightarrow -2.416$	$-2.510^{+0.030}_{-0.031}$	$-2.601 \rightarrow -2.419$	$-2.478^{+0.035}_{-0.033}$	$-2.577 \rightarrow -2.375$	-2.50 ± 0.04	$-2.59 \rightarrow -2.39$

Figure 8.12: 3ν oscillation parameters (not everything is up to date) obtained from different global analysis of neutrino data. In all cases the numbers labeled as NO (IO) are obtained assuming NO (IO), i.e., relative to the respective local minimum. SK-ATM makes reference to the tabulated χ^2 map from the Super-Kamiokande analysis of their data. Taken from [5].

vacuum expectation value v . Then the couplings of the Higgs boson are generated by the replacement:

$$v \longrightarrow v + h(x) \quad (8.45)$$

The couplings of h are then associated with the Standard Model mass terms. The Higgs interaction terms in the Standard Model Lagrangian are:

$$\begin{aligned} \Delta\mathcal{L} = & - \sum_f m_f \bar{f} f \frac{h(x)}{v} + 2m_W^2 W_\mu^+ W^{-\mu} \frac{h(x)}{v} \\ & + \frac{2}{2} m_Z^2 Z_\mu Z^\mu \frac{h(x)}{v} - 3m_h^2 \frac{h(x)}{v} + \mathcal{O}(h^4) \end{aligned} \quad (8.46)$$

These terms are all P and C conserving, so the Higgs boson is a spin-0 particle with $P = +1$. It is possible to find that v has the value:

$$v = 246 \text{ GeV} \quad (8.47)$$

So all of the couplings of the Higgs boson are highly suppressed, except for the couplings to W , Z , and t . More general models of $SU(2) \times U(1)$ symmetry breaking also have this problem. Either W , Z , or t must be involved in the relevant processes, or the expected rates of Higgs boson processes are extremely small.

We will now discuss the processes that we can use to observe the Higgs boson. We must discuss both the production and decay processes. We will start with the decays. If m_h were greater than $2m_W$ and $2m_Z$, the dominant decays would be the decays to these particles:

$$h \longrightarrow W^+ W^- \quad (8.48)$$

$$h \longrightarrow ZZ \quad (8.49)$$

These decays have been searched for at the LHC, but the only result has been to put strong limits on the production cross sections. Thus, the mass of the Higgs boson must be below the threshold for decay into WW .

In this case, the Higgs boson would decay dominantly into the next lightest Standard Model particle, the b quark. It is not so difficult to work out the decay rate for Higgs boson decay to $b\bar{b}$. The result is:

$$\Gamma(h \rightarrow b\bar{b}) = 3 \frac{\alpha_w}{8} m_h \frac{m_b^2}{m_W^2} \left(1 - \frac{4m_b^2}{m_h^2}\right)^{\frac{3}{2}} \quad (8.50)$$

The quark mass should be evaluated at $Q \approx m_h$, giving a value of about 3 GeV for m_b . Then, for a Higgs boson of mass 125 GeV, we find:

$$\Gamma(h \rightarrow b\bar{b}) \approx 2 \text{ MeV} \quad (8.51)$$

Recall that the width of the Z boson is about 2.5 GeV, a thousand times larger. So the Higgs boson is very narrow, so narrow that it will be difficult to measure the width directly. Other relevant decays to quarks and leptons

$$h \rightarrow \tau^+ \tau^- \quad (8.52)$$

$$h \rightarrow c\bar{c} \quad (8.53)$$

give decay rates about 10 times smaller than the decay rate to $b\bar{b}$.

Because the decay to $b\bar{b}$ is so highly suppressed, higher-order decay processes can compete with it. First, although $h \rightarrow WW, ZZ$ are forbidden, it is possible that the Higgs boson can decay through a diagram in which an off-mass-shell W and Z appears as a resonance, as in Figure 8.13.

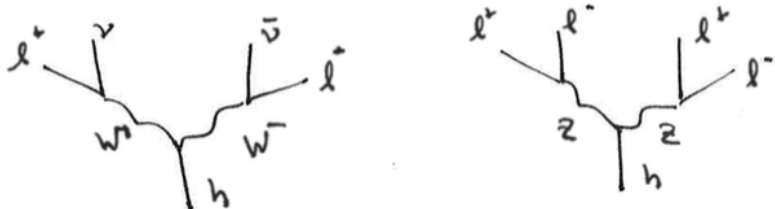


Figure 8.13: Decay of the Higgs boson to off-mass-shell W and Z pairs.

These decays are called $h \rightarrow WW^*$ and $h \rightarrow ZZ^*$. The suppression from multi-body phase space and the tail of the Breit-Wigner distribution is comparable to the suppression seen above from the small size of $(m_b/v)^2$.

It is also possible for a Higgs boson to decay through higher-order processes involving virtual top quarks or W bosons. This gives decays to two gluons, as in Figure 8.14, to two photons, as in Figure 8.15, and to γZ .

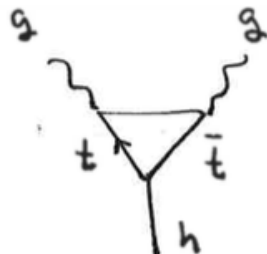


Figure 8.14: Higgs decay to two gluons.

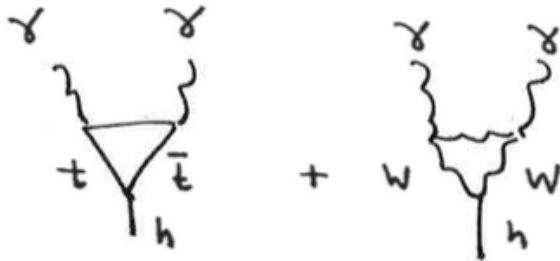


Figure 8.15: Higgs decay to two photons.

For a 125 GeV Higgs boson, the rate for $h \rightarrow 2g$ is comparable to the rate for $h \rightarrow \tau^+\tau^-$ and $h \rightarrow WW^*$. The rate for $h \rightarrow \gamma\gamma$ is about a factor of 50 smaller. A full set of predictions for the branching ratios of the Higgs boson within the Standard Model, as a function of the Higgs boson mass, is showed in Figure 8.16. These predictions of the Standard Model do not involve any parameters other than those that we have already discussed. Thus, the predictions can be highly precise. Does nature agree with these results?

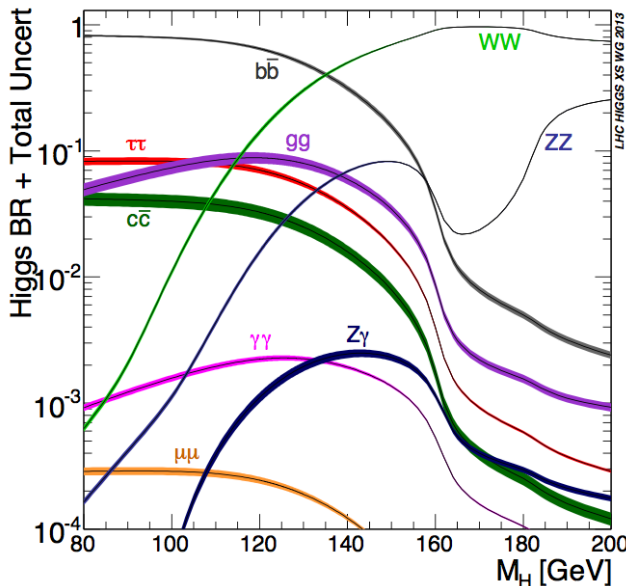


Figure 8.16: Branching ratios for decays of the Higgs boson as a function of the Higgs boson mass, predicted in the Standard Model.

8.2.2 Measurements of Higgs boson properties at the LHC

Reversing the decay processes, we find processes for producing the Higgs bosons in high energy collisions. An obvious production process is:

$$b\bar{b} \longrightarrow h \quad (8.54)$$

However, at the LHC, the cross section for this process is multiplied by the very small b quark pdf in the proton. The most promising production mode at the LHC turns out to be $gg \rightarrow h$, or **gluon-gluon fusion**, represented in the diagram in Figure 8.17, using the Higgs coupling to two gluons showed above.

The intrinsic strength of the interaction is smaller, but the initial gluons can be taken from the very large gluon pdf in the proton. At the 13 TeV LHC, a gluon momentum fraction of $x \sim 0.01$ is all that is required.

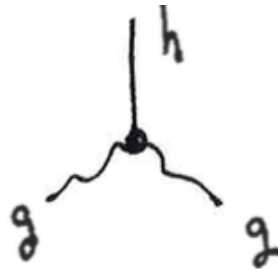


Figure 8.17: Gluon-gluon fusion diagram.

Another important production process is **vector boson fusion**, represented in Figure 8.18, in which high- x quarks in the proton create virtual W or Z bosons that then combine to produce a Higgs boson.

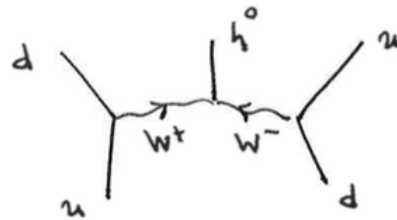


Figure 8.18: Vector boson fusion diagram.

Notice that this process results in a Higgs boson and two high-energy jets emitted in the forward direction. The presence of the forward jets can then be used to enhance the Higgs boson signal.

A third important reaction is production of a Higgs boson in association with a W or Z boson. This process can be imagined as $q\bar{q}$ annihilation to the weak boson followed by radiation of a Higgs boson using the relatively large Higgs coupling to these particles. This process is represented in Figure 8.19.

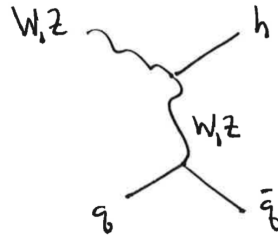


Figure 8.19: Diagram of production of h in association with W and Z bosons.

Predictions for these and other Higgs boson production processes at the LHC are showed in Figure 8.20.

For $m_h = 125$ GeV and an LHC center of mass energy of 13 TeV, the cross sections are:

$$\sigma(pp \rightarrow gg \rightarrow h) = 50 \text{ pb} \quad (8.55)$$

$$\sigma(pp \rightarrow WW \rightarrow h) = 4 \text{ pb} \quad (8.56)$$

$$\sigma(pp \rightarrow Wh, Zh) = 2 \text{ pb} \quad (8.57)$$

These results should be compared with the proton-proton total cross section of about 100 mb, which is higher by a factor of $2 \cdot 10^9$.

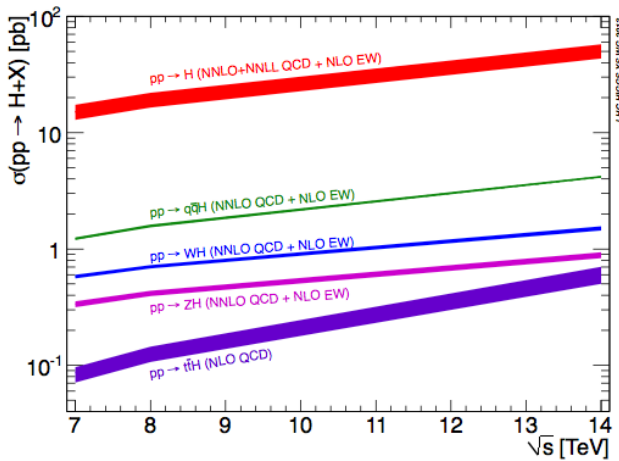


Figure 8.20: Cross sections for production of the Higgs boson at the LHC as a function of center of mass energy, predicted in the Standard Model.

At the LHC, we do not observe the total rate for Higgs production. Rather, we reconstruct the Higgs boson in a particular decay mode. The quantity that we measure has the form of a cross section times branching ratio, $\sigma \cdot \text{BR}$, for example:

$$\sigma(gg \rightarrow h) \cdot \text{BR}(h \rightarrow b\bar{b}) \quad (8.58)$$

In general, a separate selection must be used for each separate decay mode. Unfortunately, many of the most important Higgs boson decay modes are difficult to observe at the LHC. For example, the process:

$$gg \rightarrow h \rightarrow b\bar{b} \quad (8.59)$$

results in two b quark jets. However, the QCD process:

$$gg \rightarrow b\bar{b} \quad (8.60)$$

also produces pairs of b quark jets, with jet pair masses at and above the Higgs boson mass, at a rate about a million times greater. In the decays $h \rightarrow WW^*$ and $h \rightarrow ZZ^*$, events with hadronic decays of the W and Z are difficult to recognize for the same reason.

To discover the Higgs boson, the ATLAS and CMS experiments at the LHC concentrated their efforts on decay modes of the Higgs boson to photons and leptons in which all final state particle would be visible. These modes are:

$$h \rightarrow \gamma\gamma \quad \text{BR} = 0.23\% \quad (8.61)$$

$$h \rightarrow ZZ^* \rightarrow 4\ell \quad \text{BR} = 0.016\% \quad (8.62)$$

In all, Higgs boson production and decay into these modes occurs in about 1 in $2 \cdot 10^{12}$ pp collisions. It was quite a feat to collect such events in the presence of enormous numbers of more ordinary LHC collisions. By collecting a very large data set, the LHC experiments were able to identify the Higgs boson in these channels. Figure 8.21 shows a candidate $pp \rightarrow h \rightarrow \gamma\gamma$ event from CMS. Figure 8.22 shows the distribution of $pp \rightarrow \gamma\gamma$ events found by CMS as of June 2012 as a function of the invariant mass of the $\gamma\gamma$ pair. There is a clear resonance on the expected smooth background at a mass of about 125 GeV. Figure 8.23 shows a candidate $pp \rightarrow h \rightarrow e^+e^-\mu^+\mu^-$ event collected by the ATLAS experiment. Figure 8.24 shows the 4-lepton events seen by the ATLAS experiment as of June 2012, plotted as a

function of the 4-lepton invariant mass. A significant resonance signal is seen at the same mass of 125 GeV. On July 4, 2012, both experiments showed significant signals in both of these channels, presenting strong evidence for the appearance of this particle.

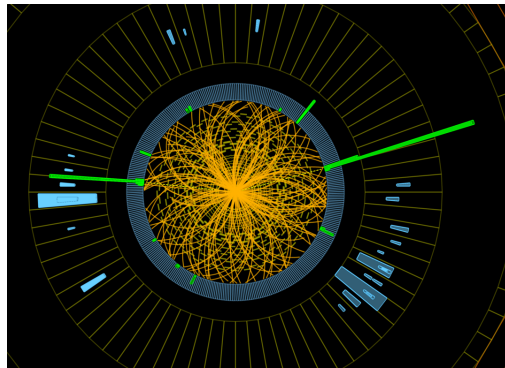


Figure 8.21: Candidate $pp \rightarrow h \rightarrow \gamma\gamma$ event observed by the CMS experiment at the LHC.

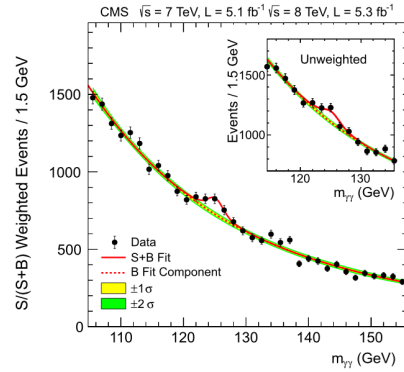


Figure 8.22: Mass distribution of γ pairs measured by the CMS experiment at the LHC. In main plot, events more likely to be well-reconstructed $pp \rightarrow \gamma\gamma$ events are given higher weight.

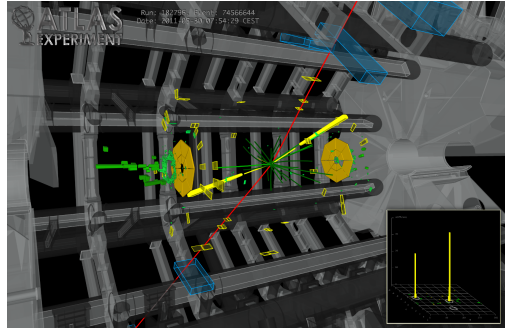


Figure 8.23: Candidate $pp \rightarrow h \rightarrow e^+e^-\mu^+\mu^-$ event observed by the ATLAS experiment at the LHC.

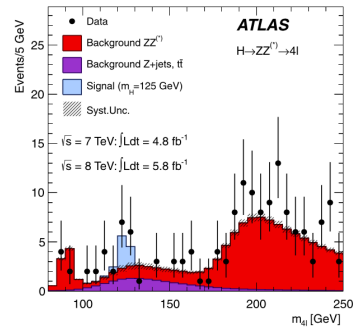


Figure 8.24: Mass distribution in four-lepton events measured by the ATLAS experiment at the LHC.

With the new particle identified, we can ask whether it indeed has the properties expected for the Higgs boson. First, is it a particle with $J^P = 0^+$, as the Standard Model predicts? If the new resonance decays to $\gamma\gamma$, it cannot be a particle of spin 1. However, the possibilities of spin greater than 1, and of $P = -1$, would still be open. These hypotheses can be addressed using $h \rightarrow ZZ^* \rightarrow 4$ leptons events. The relative orientations of the leptons in these events give information on the polarizations of the Z bosons in $h \rightarrow ZZ^*$. Also, they allow tests of whether the particle production and decay is independent of orientation, as would be expected for a spin-0 particle. Figure 8.25 shows tests of the various spin and parity hypotheses relative to the hypothesis of $J^P = 0^+$. In all cases, the 0^+ hypothesis is favored. In most cases, this hypothesis is strongly favored already with this sample of about 25 events.

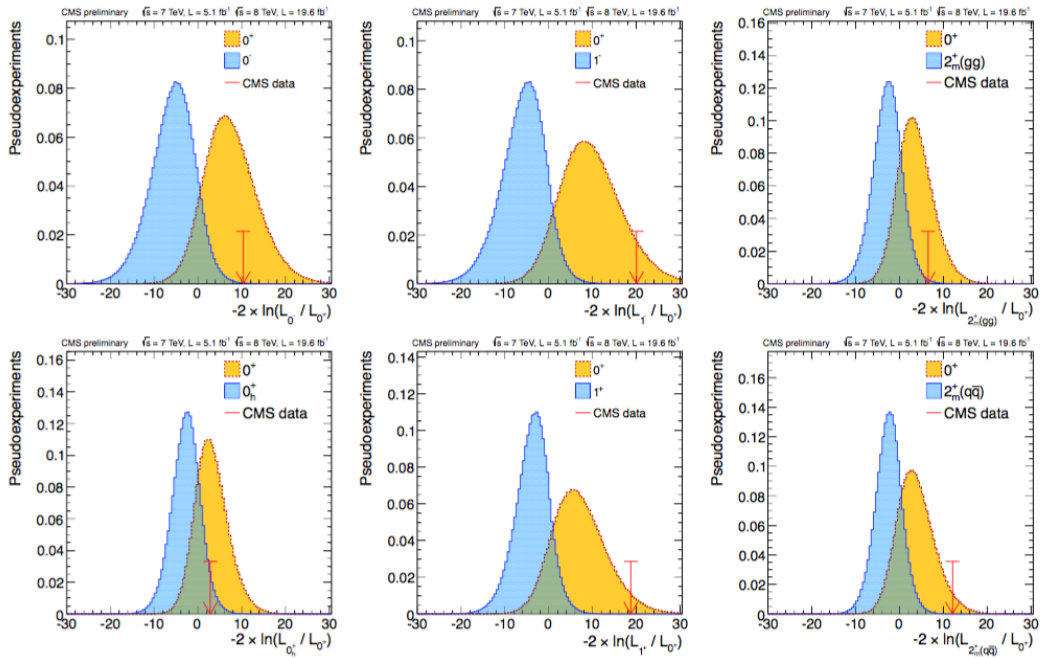


Figure 8.25: Comparison of hypotheses for the spin and parity of the 125 GeV resonance from event distributions in $h \rightarrow 4\ell$. What is shown in each plot is the distribution of a test statistic expected for the Standard Model 0^+ hypothesis (yellow) and for an alternative hypothesis (blue). The arrow shows the value of the test statistic given by the data.

Chapter 9

Exercises

Exercise 1: Electromagnetic shower in calorimeters

Calculate the average number of particles in an electromagnetic shower initiated by a 50 GeV photon, after 10, 13 and 20 cm of crossed iron.

Hint: search for the radiation length of the iron on the PDG.

Searching on Particle Data Group^a, we find for e^- :

$$X_0^{\text{Fe}} = 1.757 \text{ cm} \quad (9.1)$$

$$E_C^{\text{Fe}} = 21.68 \text{ MeV} \quad (9.2)$$

So, until the energy of the product particles is lower than the critical energy E_C , we have:

$$N(x) = 2^{\frac{x}{X_0^{\text{Fe}}}} \quad (9.3)$$

We find these values:

$$N(x = 10 \text{ cm}) \approx 52 \quad (9.4)$$

$$N(x = 13 \text{ cm}) \approx 169 \quad (9.5)$$

$$N(x = 20 \text{ cm}) \approx N(x \approx 19.6 \text{ cm}) \approx 2306 \quad (9.6)$$

We note that for $x = 20 \text{ cm}$, the critical energy has already been reached at $x \approx 19.6 \text{ cm}$, so the number of product particles has to be computed at this distance with Eq. 9.3.

^ahttp://pdg.lbl.gov/2010/AtomicNuclearProperties/HTML_PAGES/026.html

Exercise 2: Energy loss of muons

A muon of 100 GeV energy crosses without being absorbed a detector whose mass is mainly due to the hadronic calorimeter and to the muon detector. The thickness of the crossed material can be considered as a layer of 3 m of iron. Determine:

- What is the dominant energy loss process.
- The average loss of the muon inside the detector.

Hint: look at the energy loss picture of muons.

Exercise 3: Electron inelastic scattering

An electron with a $E = 20$ GeV kinetic energy collides inelastically on a proton at rest. The electron is scattered at an angle $\theta = 5^\circ$ with respect to its original direction and with an energy $E' = 12$ GeV. Calculate the effective mass of the final hadronic system.

Exercise 4: Structure function

The momentum distribution of the u -type quark in the proton can be parametrized by the formula:

$$F_u(x) \approx xu(x) = a(1-x)^2 \quad (9.7)$$

Determine the constant a with the assumption that the u quarks carry 33% of the proton momentum.

Exercise 5: Gluon structure function

It is believed that the structure function describing the distribution of the gluon momentum inside the nucleons, $g(x)$, strongly increases with decreasing x . Estimate the number of gluons that would be possible to resolve with deep inelastic

$$e + p \longrightarrow e + X \quad (9.8)$$

collisions at $Q^2 = 104$ GeV 2 at low x values (in the intervals $0.0001 \div 0.001$, $0.001 \div 0.01$, $0.01 \div 0.1$). Assume that at these Q^2 values the distribution function of the gluons is:

$$xg(x) = 0.36x^{-0.5} \quad (9.9)$$

Bibliography

- [1] Michael E. Peskin *Concepts of Elementary Particle Physics*. Oxford Master Series in Particle Physics, Astrophysics and Cosmology April 2, 2019
- [2] Richard Wigmans Department of Physics, Texas Tech University, Lubbock, TX 79409-1051, U.S.A. *Calorimetry*. http://siba.unipv.it/fisica/ScientificaActa/volume_2_1/Wigmans.pdf
- [3] C. W. Fabjan (CERN, Geneva, Switzerland) and T. Ludlam (Brookhaven National Laboratory, Upton, Long Island, New York 11973, USA) *Calorimetry in high-energy physics*. <https://www.annualreviews.org/doi/pdf/10.1146/annurev.ns.32.120182.002003>
- [4] Luigi Di Lella (University of Pisa) and Carlo Rubbia (Gran Sasso Science Institute) *The Discovery of the W and Z Particles*. https://cds.cern.ch/record/2103277/files/9789814644150_0006.pdf
- [5] M.C. Gonzalez-Garcia (YITP, Stony Brook; ICREA, Barcelona; ICC, U. of Barcelona) and M. Yokoyama (Tokyo U.; Kavli IPMU (WPI), U. Tokyo). *14. Neutrino Masses, Mixing, and Oscillations*. <http://pdg.lbl.gov/2019/reviews/rpp2019-rev-neutrino-mixing.pdf>
- [6] <https://wiki.physik.uzh.ch/cms/latex:feynman>